Air Force Office of Scientific Research #AFOSR-91-0269

DIAGNOSING BOUNDARY-LAYER FRACTIONAL CLOUDINESS IN A MESOSCALE MODEL

by David M. Mocko

William R. Cotton, P.I.

Colorado State University

DEPARTMENT OF ATMOSPHERIC SCIENCE

PAPER NO. 553

DIAGNOSING BOUNDARY-LAYER FRACTIONAL CLOUDINESS IN A MESOSCALE MODEL

by

David M. Mocko

Department of Atmospheric Science

Colorado State University

Fort Collins, CO 80523

Research Supported by

Air Force Office of Scientific Research

under Grant #AFOSR-91-0269

April 5, 1994

Atmospheric Science Paper No. 553

ABSTRACT

DIAGNOSING BOUNDARY-LAYER FRACTIONAL CLOUDINESS IN A MESOSCALE MODEL

The Regional Atmospheric Modeling System (RAMS), developed at Colorado State University, was used to predict boundary-layer clouds and diagnose fractional cloudiness. The case study for this project occurred on 7 July 1987 off the coast of southern California. On this day, a transition in the type of boundary-layer cloud was observed from a clear area, to an area of small scattered cumulus, to an area of broken stratocumulus, to an area of solid stratocumulus. This case study occurred during the First ISCCP (International Satellite Cloud Climatology Project) Regional Experiment (FIRE) field study in this locale. RAMS was configured with three interactive nested grids: a coarse grid with 80 km model spacing covering the western 1/4 of the U.S. and the eastern 1/3 of the Pacific, a 20 km grid covering the ocean waters off the southern California coast, and a 5 km grid covering the transition area. The non-hydrostatic version of RAMS was chosen, and explicit bulk microphysics was used. The model was initialized using rawinsondes and surface aviation observations (SAOs) as archived at the National Center for Atmospheric Research (NCAR).

A unique feature of this study is that a cumulus parameterization scheme was used that predicts on vertical velocity variance. Various fractional cloudiness schemes found in the literature were then implemented into RAMS and tested against each other in order to determine which best represented observed conditions.

The RAMS model was also configured for a separate case study which occurred as part of the Boundary Layer Experiment - 1983 (BLX83). This field project took place over central Oklahoma in June of 1983. On the case day, clear conditions existed early in the morning. As the day progressed, scattered boundary-layer cumuli developed and dissipated through the afternoon. The model was configured with one 5 km grid and was initialized horizontally homogeneous with a morning sounding. The fractional cloudiness schemes were also examined for this case study and compared to observations.

David M. Mocko
Department of Atmospheric Science
Colorado State University
Fort Collins, Colorado 80523
Spring 1994

ACKNOWLEDGEMENTS

I would like to thank my advisor, Dr. William R. Cotton, for his guidance and support over the last few years. I would also like to thank him for the opportunity to work with the RAMS model. Committee members Dr. Roger A. Pielke and statistics professor Dr. Paul W. Mielke are also thanked for their helpful contributions to this thesis.

I would also like to acknowledge Drs. Cotton and Pielke for their efforts in the classroom, as well as other members of the Atmospheric Science Department, especially Dr. Wayne H. Schubert, Dr. Thomas B. McKee, and Dr. Richard H. Johnson. Information that I acquired in their classes was instrumental in completing this thesis.

Many thanks are extended to Greg Thompson for his help in understanding and starting up the RAMS model. His assistance ranged from help with conceptual ideas to coding problems. His work in improving the RAMS analysis package is also appreciated.

Thanks are also extended to Dr. Michael Weissbluth for his help in using his small-scale turbulence parameterization and in extracting additional information from it. Dr. Robert L. Walko is also thanked for his assistance in negotiating the RAMS code and in solving model numerical problems (a.k.a., model crashes).

Brenda Thompson, Abby Hodges, and Lucy McCall are thanked for their invaluable assistance in preparing this thesis and the accompanying flurry of paperwork. No other members of our group were always as willing to help me out and always as friendly while I was pestering them.

I would like to thank my friend/office mate/co-worker –*insert name here*– for his/her: 1) unending moral support, 2) helpful insight in both classwork and research, and/or 3) constant supply of good times. Not enough kind, glowing things can be said about you - I only wish I had the space to give each of you a personal greeting!

Computer expert Donna Chester is thanked for her efforts. Her help in everything from software tips to bringing the computer back to life is deeply appreciated.

Brian Beitler is also thanked for his computing knowledge. His assistance with my personal computer allowed me to perform some of this work remotely and saved me many hours in putting together the figures for this thesis.

I would like to thank my roommates, Eric Stevens and Matthew Savoie, for being such fun to live with and for their support in sharing the downsides of graduate student life. Their evening guitar playing never failed to cheer me up.

I would like to thank my good friend, John A. Pasqua, who is still living in New Jersey. Our weekly phone calls allowed me an unbiased outlet for my frustations and kept me informed on the performances of the New Jersey Devils hockey team. This year, John, I mean it - they are going all the way!

Finally, I would like to thank my family for their support while moving almost 2000 miles away from them. I greatly miss seeing you more than twice a year, but I thank God for providing me with such loving parents and terrific brothers.

This research was made possible under contract #AFOSR-91-0269 through the Air Force Office of Scientific Research. Computations were performed on an IBM RS/6000-320 workstation purchased under support of AFOSR.

TABLE OF CONTENTS

1 INTRODUCTION **1**
1.1 Overview 1
1.2 Summary 2

2 BACKGROUND **3**
2.1 Reasons for study 3
2.2 Typical characteristics of the STBL 4
2.2.1 Diurnal variation and life cycle 6
2.2.2 Cloud breakup 9
2.3 Typical characteristics of the CBL 12
2.4 Previous modeling studies 13
2.4.1 Modeling the boundary layer 13
2.4.2 Modeling fractional cloudiness 15

3 RAMS CONFIGURATION **17**
3.1 ISAN 17
3.2 Model 18
3.2.1 Variables 18
3.2.2 Grids 19
3.2.3 Numerics 19
3.2.4 Parameterizations 19
3.2.5 Domain 23
3.3 VAN 23

4 FRACTIONAL CLOUDINESS DESCRIPTIONS **26**
4.1 As a function of RH 27
4.1.1 Albrecht 27
4.1.2 Kvamstø 28
4.1.3 Sundqvist, Berge, and Kristjansson 29
4.2 As a function of mixing line slopes 30
4.2.1 Betts and Boers - wet adiabat 30
4.2.2 Betts and Boers - wet virtual adiabat 32
4.3 As a function of sub-grid variability 33
4.3.1 Ek and Mahrt 33
4.3.2 Manton and Cotton 36
4.3.3 Sommeria and Deardorff 37
4.3.4 Bechtold, Fravalo, and Pinty 39
4.4 Uncertainties in evaluation 40

5 7 July 1987 **42**
5.1 Observed Conditions 42
5.2 Comparison to observed conditions 48
5.3 Comparison to cloud transition 54
5.3.1 Comparison to satellite imagery 54
5.3.2 Comparison to fractional cloudiness measurements 67

6 7 June 1983 **70**
6.1 Observed conditions 70
6.2 Model set-up 71
6.3 Comparison to observations 74
6.3.1 Comparison of fractional cloudiness 75
6.3.2 Comparison when modifying radiation 83

7 SUMMARY AND CONCLUSIONS **95**
7.1 Summary 95
7.2 Conclusions 96
7.3 Suggestions for future research 98

LIST OF FIGURES

2.1 Mean conditions within the stratocumulus-topped boundary layer (from Stull (1988)). 5
2.2 Life cycle of a stratocumulus deck (from Paluch and Lenschow (1991)). 8
2.3 Lidar cloud top heights (dots) and cloud fraction (line) as measured 7 July 1987 (from Betts and Boers (1990)). 10
2.4 Mean thermodynamic profiles for four regimes: Clear, Cumulus, Broken, and Stratocumulus (from Betts and Boers (1990)). 11
2.5 Mean conditions within the convective boundary layer (from Stull (1988)). . . . 12

3.1 Grids showing domain of first and second grids from the RAMS configuration. 24
3.2 Grids showing domain of second and third grids from the RAMS configuration. 25

4.1 Dependence of RH and SR on FC-Albrecht (from Albrecht,1989). 28
4.2 Dependence of RH on FC-Kvamstø. 29
4.3 Dependence of RH on FC-Sundqvist et al. 30
4.4 Depiction of cloud fraction (dark region) for a Gaussian distribution of relative humidity (from Ek and Mahrt, 1991). 34

5.1 RAMS depiction of synoptic-scale initial mean sea level pressure and winds for Grid 1 at 00 UTC 7 July. 43
5.2 RAMS depiction of mesoscale initial mean sea level pressure and winds for Grid 2 at 00 UTC 7 July. 44
5.3 RAMS depiction of synoptic-scale initial 700 hPa geopotential heights and winds for Grid 1 at 00 UTC 7 July. 45
5.4 RAMS depiction of synoptic-scale initial 500 hPa geopotential heights and winds at 00 UTC 7 July. 46
5.5 RAMS depiction of synoptic-scale initial 250 hPa geopotential heights and winds at 00 UTC 7 July. 47
5.6 LANDSAT scene at 1830 UTC 7 July 1987 with center coordinates 33°10'N, 121°44'W. (from Betts and Boers, 1990). 49
5.7 RAMS 24-hour prediction of mean sea level pressure and winds for Grid 1 valid at 00 UTC 8 July. 50
5.8 RAMS 18.5-hour prediction of potential temperature (K) for Grid 3 valid at 1830 UTC 7 July. 52
5.9 RAMS 18.5-hour prediction of total specific humidity (g/g) for Grid 3 valid at 1830 UTC 7 July. 53
5.10 RAMS 20.5-hour prediction of soundings across transition valid at 2030 UTC 7 July. 55
5.11 Albrecht's fractional cloudiness scheme, from the RAMS third grid, 262 m AGL, valid 1830 UTC 7 July 1987. 56

5.12 Kvamstø's fractional cloudiness scheme, from the RAMS third grid, 262 m AGL, valid 1830 UTC 7 July 1987. . . . 57
5.13 Sundqvist et al.'s fractional cloudiness scheme, from the RAMS third grid, 262 m AGL, valid 1830 UTC 7 July 1987. . . . 58
5.14 Betts and Boers' wet adiabat fractional cloudiness scheme, from the RAMS third grid, valid 1830 UTC 7 July 1987. . . . 59
5.15 Betts and Boers' wet virtual adiabat fractional cloudiness scheme, from the RAMS third grid,valid 1830 UTC 7 July 1987. . . . 60
5.16 Ek and Mahrt's fractional cloudiness scheme, from the RAMS third grid, 262 m AGL, valid 1830 UTC 7 July 1987. . . . 61
5.17 Manton and Cotton's fractional cloudiness scheme, from the RAMS third grid, 262 m AGL, valid 1830 UTC 7 July 1987. . . . 62
5.18 Sommeria and Deardorff's fractional cloudiness scheme, from the RAMS third grid, 262 m AGL, valid 1830 UTC 7 July 1987. . . . 63
5.19 Bechtold et al.'s fractional cloudiness scheme, from the RAMS third grid, 262 m AGL, valid 1830 UTC 7 July 1987. . . . 64

6.1 Grid showing domain of the RAMS configuration used for the Oklahoma simulations. . . . 72
6.2 Sounding used for initialization of the Oklahoma simulations, taken at 10:00 a.m. local time, Canton, OK, 7 June 1983. . . . 73
6.3 RAMS time-height prediction of vertical velocity variance for the center grid point. 76
6.4 RAMS time-height prediction of potential temperature for the center grid point. 77
6.5 RAMS time-height determination of FC-Kvamstø for the center grid point. . . 79
6.6 RAMS time-height determination of FC-Sundqvist et al. for the center grid point. 80
6.7 RAMS time-height determination of FC-Ek and Mahrt for the center grid point. 81
6.8 Time-series plot at the center grid point of fractional cloudiness through the boundary layer for: (A) observations; (B) Kvamstø; (C) Sundqvist et al.; and (D) Ek & Mahrt. . . . 83
6.9 RAMS time-height determination of FC-Bechtold et al. for the center grid point. 84
6.10 RAMS time-height determination of FC-Manton and Cotton for the center grid point. . . . 85
6.11 RAMS time-height prediction of vertical velocity variance for the center grid point when the long and short wave radiation have been modified. . . . 89
6.12 RAMS time-height determination of FC-Kvamstø for the center grid point when the long and short wave radiation have been modified. . . . 90
6.13 RAMS time-height determination of FC-Sundqvist et al. for the center grid point when the long and short wave radiation have been modified. . . . 91
6.14 RAMS time-height determination of FC-Ek and Mahrt for the center grid point when the long and short wave radiation have been modified. . . . 92
6.15 Time-series plot at the center grid point of fractional cloudiness through the boundary layer for: (A) observations; (B) Kvamstø; (C) Sundqvist et al.; and (D) Ek & Mahrt. . . . 94

LIST OF TABLES

4.1 Mixing line slopes and adiabats for four cloudiness regimes, including error estimates (from Betts and Boers, 1990). 31

5.1 Comparison between the fractional cloudiness schemes and satellite imagery for three sections of the third grid. 66
5.2 Boundary between cloud regimes and cloud fraction within each regime at 2032 UTC and 31.6° N (from Betts and Boers, 1990). 67
5.3 Comparison between the fractional cloudiness schemes and observations for each cloud regime. 68

6.1 Cloud coverage from lidar and aircraft reports during the afternoon of 7 June 1983 (from Stull et al., 1989). 71
6.2 Cloud coverage from lidar and aircraft reports during the afternoon of 7 June 1983 (from Stull et al., 1989) compared to the fractional cloudiness through the boundary layer from the Kvamstø, Sundqvist et al., and Ek & Mahrt schemes. 82
6.3 As in Table 6.2, except for when the fractional cloudiness has modified the radiation. 93

7.1 Brief review of good points of using each fractional cloudiness scheme 97
7.2 Brief review of bad points of using each fractional cloudiness scheme 98

Chapter 1

INTRODUCTION

We've been blown around from town to town,
Just looking for a place to land.
Where the sun breaks through the clouds and falls like a circle,
A circle of fire down on this hard land.

- Bruce Springsteen "This Hard Land"

1.1 Overview

Boundary layer cloudiness is an important part of the full representation of the planetary boundary layer (PBL). Low level clouds affect the PBL by modifying its radiative forcing (both long wave and short wave), its moisture profile, and its surface parameters. Low level clouds found near the top of the PBL include small cumulus, broken stratocumulus, and solid stratocumulus. Stratocumulus clouds are climatologically found on the east side of oceans, where cooler water is found near the continent (e.g., Lilly, 1968). Further away from the continent, the water temperature is warmer and the cloud type usually switches to small cumulus. The transition between the solid stratocumulus deck and the scattered small cumulus field can be identified from the fractional cloudiness parameter.

The First ISCCP (International Satellite Cloud Climatology Project) Regional Experiment (FIRE I) ran a field project off the southern California coastline from 29 June to 19 July 1987. One of the objectives of this marine stratocumulus experiment was a study into fractional cloudiness amount. One research day, 7 July 1987, showed a sharp transition in cloud amount, from clear conditions, through broken cloudiness, to a solid stratocumulus deck very near the coast. This study will examine the feasibility of diagnosing boundary-layer fractional cloudiness in a mesoscale model through comparisons of fractional cloudiness schemes using model simulations.

These schemes will also be tested against each other in simulations of boundary layer cumulus over Oklahoma. The Boundary Layer Experiment - 1983 (BLX83) ran a field project over Oklahoma from 25 May to 18 June 1987. One research day, 7 June 1983, showed boundary-layer cumuli develop and dissipate during the afternoon. This investigation will provide another way to evaluate these fractional cloudiness schemes.

1.2 Summary

In Chapter 2 of this thesis a background on fractional cloudiness and boundary layer processes is given. This background includes insight into the importance of undertaking this study and into the development of the boundary layer over both land and sea. Previous attempts of the mesoscale modeling of boundary layer clouds are also presented there. Next, the mesoscale model used for this study, the Regional Atmospheric Modeling System (RAMS), is discussed in Chapter 3. The model set-up and parameterizations used are mentioned in this chapter. In Chapter 4 a detailed mathematical description is provided of every fractional cloudiness parameterization that RAMS will use to diagnose the boundary layer cloud cover amount. Comparison of model results to observed conditions from FIRE I takes place in Chapter 5. The comparison includes the relative performance of each fractional cloudiness scheme. The set-up and results of the Oklahoma boundary layer cumulus model runs are discussed in Chapter 6. Finally, in Chapter 7 a summary and conclusions are found and ideas for future research are provided.

Chapter 2

BACKGROUND

2.1 Reasons for study

Stratocumulus clouds are climatologically common over the eastern side of oceans in areas of a subtropical high. The importance of these clouds to climate has been shown, especially when knowing that, at any time, these clouds cover a sizeable portion of the earth. Stratocumulus clouds are important because low-level clouds do not significantly reduce the amount of long wave radiation emitted from earth to space but do significantly increase the amount of short wave radiation reflected to space. This disparity can lead to net cooling. It is this net cooling which is important to climate and can act to offset the greenhouse effect (Cahalan and Snider, 1989). These clouds tend to be plane-parallel, located at the top of the boundary layer between the lifting condensation level and the boundary-layer inversion.

The boundary layer has many significant effects on both people and the atmosphere. Because it is the part of the troposphere that is directly influenced by the earth's surface and it responds to surface forcings within an hour's time, it has tremendous impact on weather at the surface. The boundary layer must also be studied to determine pollution dispersion, crop moisture, evaporation, etc. The boundary layer affects the atmosphere in many ways as well. About 50 percent of the dissipation of atmospheric kinetic energy occurs in the boundary layer from turbulence. The boundary layer also provides water vapor and cloud nuclei for the atmosphere.

There are two main types of cloudy boundary layers typically observed in the atmosphere. These are the stratocumulus-topped boundary layer (STBL) and the convective boundary layer (CBL). Studying the STBL is useful for many reasons as mentioned previously. Studying the CBL brings insight into development of convection and wind storms.

2.2 Typical characteristics of the STBL

In order to focus on a particular section of the world, attention will be turned to the persistent stratocumulus cloudiness that occurs off of the California coast during the summer months. These clouds are usually formed as part of a typical synoptic pattern that develops in the California area in the summer. This synoptic pattern can last for days or more, causing relatively steady cloud cover in the region. A thermal low in the Arizona/California deserts, in combination with a Pacific subtropical high, causes north and northwesterly winds in the oceans off California. These winds can be strong and often act to cause upwelling of cold ocean waters near the coast. The wind stress displaces the water near the surface and brings about a sloping sea surface. Colder water from lower depths must then come up to counteract the sloping surface. This process causes relatively cold sea surface temperatures during the summer.

The cold sea surface temperatures and north to northwest winds cause the formation of a well-mixed moist boundary layer. Often, the low-level moisture can produce fog, or if air is brought to the mixing condensation level (MCL), clouds exhibiting a cumulus structure can be formed. The Pacific subtropical high, however, in place has subsidence of the air associated with it. The subsiding air, as it interacts with the boundary layer, will form a capping inversion. At the capping inversion, sounding data changes rapidly. Figure 2.1 shows typical conditions in a stratocumulus field. It demonstrates the sharp rise of potential temperature and a sharp decrease in moisture.

In their June 1976 study of marine stratocumulus mixed-layers off of California from aircraft data, Brost et al. (1981a) found that the aforementioned synoptic conditions and resulting processes are typical for half the stratocumulus clouds formed in this area during the summer. They noted that the stronger the subtropical high tended to be, the stronger the resultant north to northwest winds were, and the stronger the capping inversion was. As above, these two factors helped to build a solid stratocumulus layer. Brost et al. also examined the climatological winds in the area and found that the north to northwest winds, when observed, are usually stronger in magnitude than average winds in the area. They

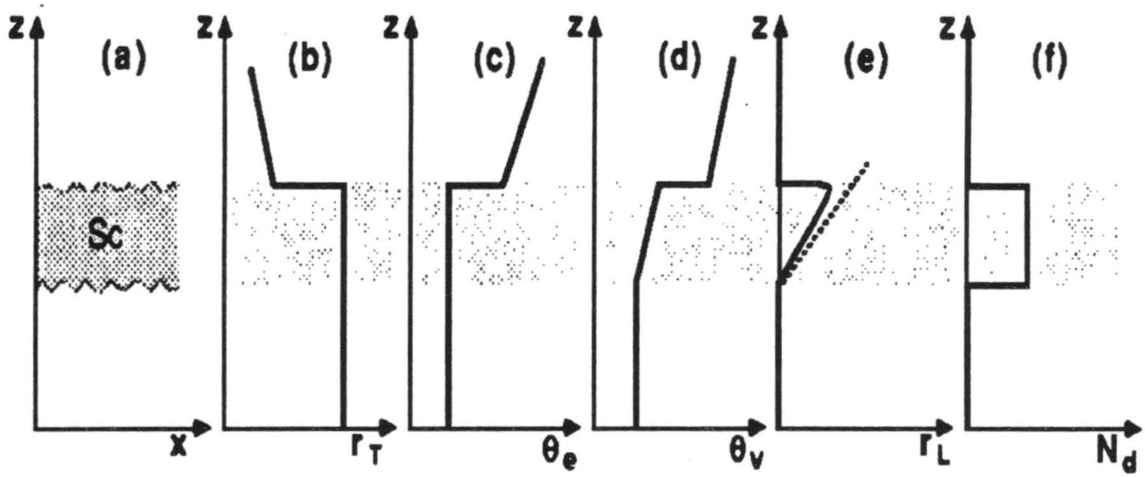

Figure 2.1: Mean conditions within the stratocumulus-topped boundary layer (from Stull (1988)). (a) cloud location; (b) total water mixing ratio; (c) equivalent potential temperature; (d) virtual potential temperature; (e) liquid water mixing ratio; (f) number density of cloud droplets. The dashed line in (e) represents the theoretical adiabatic value of liquid water mixing ratio.

concluded that wind speeds in the presence of stratocumulus clouds in this area tend to be greater than the average wind speed.

The stratocumulus-topped boundary layer (STBL) is also turbulent, but at the same time very moist, especially through the cloud layer. The main mechanism driving the turbulence is radiative cooling at cloud top. Over an ocean surface, solar heating provides a slow response as a result of the large heat capacity of water. Heating at the surface is further reduced by the cloud layer, but it still must be considered. The long wave radiative cooling in the cloud results in negatively buoyant air. This air horizontally converges and sinks as a cool parcel. These downdrafts and compensating updrafts effectively mix the layer. Area fraction and magnitudes of updrafts and downdrafts in the STBL are generally equal (Schumann and Moeng, 1991). The virtual potential temperature and total mixing ratio are nearly constant with height, while the liquid water mixing ratio increases linearly from cloud base to cloud top. Updrafts in the STBL are usually warmer (as a result of surface heating) and moister (as a result of surface evaporation). There is a capping inversion, which causes a rise to the virtual potential temperature and a fall to the total mixing ratio. The inversion determines cloud top and is where the liquid water mixing ratio drops to zero.

In Brost et al. (1981b) the turbulence budgets of stratocumulus clouds was studied. They found that shear production can dominate through the entire boundary layer. They also found that radiative cooling is concentrated in the upper few tens of meters of the cloud. In this area, potential temperature reduced by radiative cooling is nearly balanced by that gained by shear-driven entrainment. Shear production gives a gain to turbulent kinetic energy (TKE) and buoyant production gives a loss to TKE, for this case. Brost et al. also show how drizzle can affect the stability of the boundary layer. Heating occurs in the upper layers due to condensation and cooling occurs in the lower layers due to evaporation. This results in two shallow unstable layers separated by an intermediate stable layer.

2.2.1 Diurnal variation and life cycle

Although stratocumulus cloud formation, development, and dissipation is controlled heavily by synoptic conditions persisting for several days or more, there is a noted daily variation in the clouds. This variation is as a result of changes in solar heating of the stratocumulus cloud. These changes force a diurnal cycle of cloud cover, liquid water content, and cloud thickness. Changing synoptic conditions produce a separate stratocumulus cloud life cycle which can, as mentioned before, take upwards of a few days.

Among the more recent studies of a diurnal cycle, Minnis et al. (1991) examined satellite data from the FIRE I experiment during July 1987. One of the most significant findings noted was the change in cloud cover. Satellite-determined cloud cover showed a minimum in the late afternoon and a maximum in the early morning. The afternoon minimum is caused by the solar heating during the daytime hours. Short wave radiation heats the cloud layer and can evaporate cloud water. As this cloud water evaporates, some of the weaker and/or smaller of the convective cells will dissipate, which results in reduced cloud cover. The opposite process works at night - the loss of short wave heating causes the clouds to re-organize as a result of long wave radiational cooling. The cooling causes condensation and cloud formation, giving rise to the morning maximum in cloud cover. Minnis et al. also found that cloud thickness, cloud top height, and liquid water content reached maxima in the morning and minima in the afternoon.

In addition, Minnis et al. compared cloud covers derived from the satellite data and from island-base instrumentation. During the FIRE experiment, much of the ground-based instrumentation was positioned on San Nicholas Island (SNI), which is positioned southwest of Los Angeles. This island was usually in the region of persistent cloud cover during the occurrence of a stratocumulus cloud deck. It was found that cloud cover tended to be longer lived directly over the island than over the adjacent waters. This bias towards cloudiness over the island is more pronounced during the daytime. This occurs as a result of differential heating rates over the island versus over the ocean. Short wave heating that penetrates the cloud layer causes a greater buoyancy flux over the island than over the ocean. It is this additional buoyancy which causes cloud cover to be maintained over the island. Mesoscale convergence over the island can also cause baroclinic circulations to develop.

Paluch and Lenschow (1991) also studied data from the FIRE experiment. They used aircraft data to look at how sea surface heating and precipitation evaporation affects the cloud formation. They found that air being heated near the sea surface will lead to the formation of a stratus layer, while air being cooled near the sea surface or by the evaporation of precipitation will produce a field of cumuli. From their findings, they built a conceptual model of the life cycle of a stratocumulus deck (Figure 2.2). First, the stratus layer forms as a result of heating near the sea surface. As it forms and strengthens, long wave radiation at cloud top cools the cloud and strengthens the inversion. Because the cloud is cooler than adjacent clear air, baroclinic circulations are formed which, in conjunction with mixing and moisture fluxes, produce a patchy cloud structure. Evaporating precipitation begins to cool air underneath the cloud. Cooling in this area under the cloud may lead to convective instability and the formation of cumuli underneath the stratus cloud. With time, the mixing and baroclinicity of the stratus layer may cause its dissipation, leaving behind a field of cumuli. Entrainment of warm dry air from above the inversion can also act to dissipate portions of the stratus layer.

Skupniewicz et al. (1991) used sodar observations to examine the effects of cloud shading on the surface heat flux and boundary layer heights. This study was done by studying cases where the stratocumulus cloud moved in and off the coast in a diurnal cycle. They found that surface temperatures on the cloudy side of the cloud-clear line were colder and

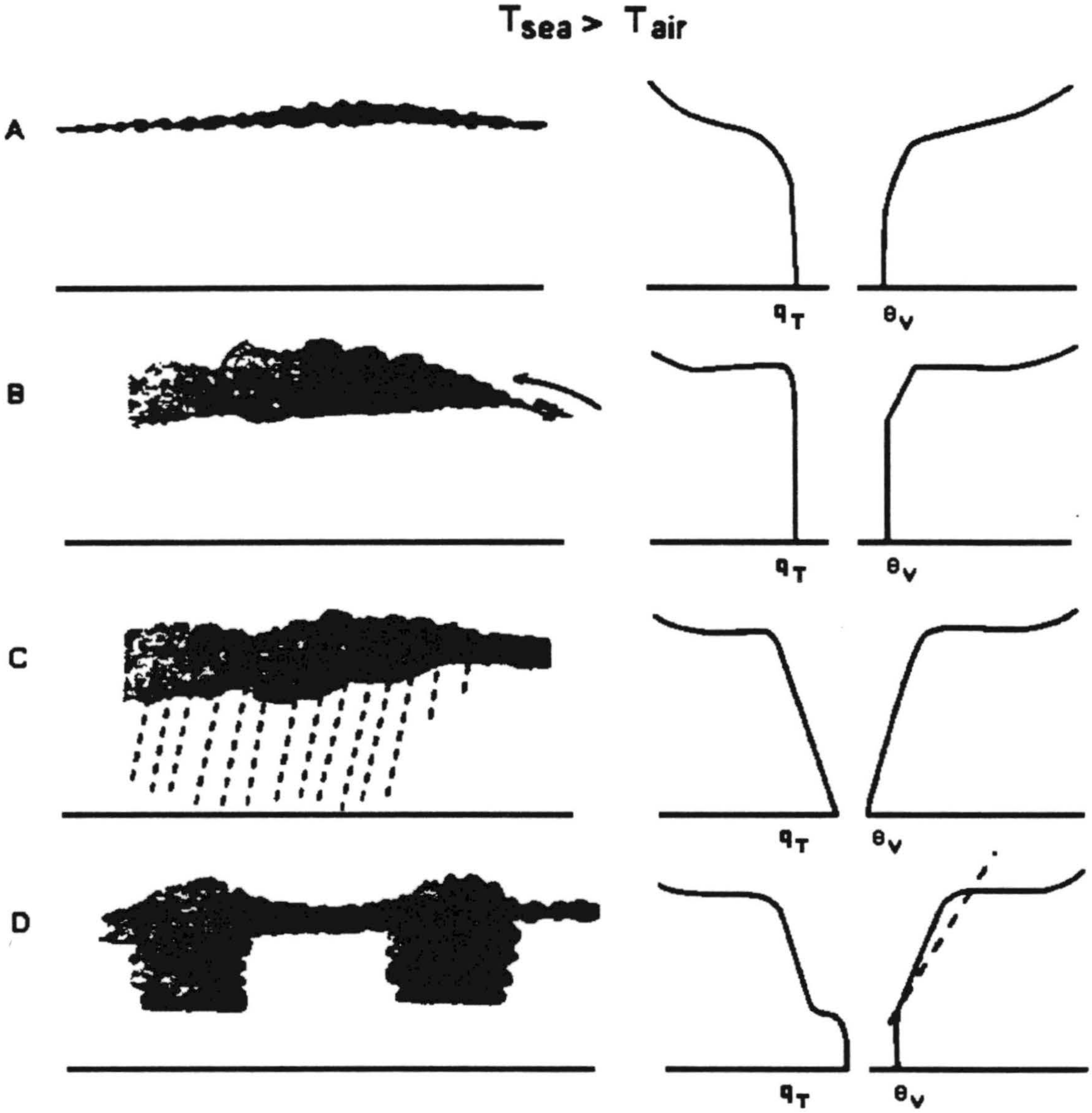

Figure 2.2: Life cycle of a stratocumulus deck (from Paluch and Lenschow (1991)). (a) Stratus layer forms; (b) Inversion strengthens; (c) Evaporating precipitation cools air under the cloud layer; (d) Cumuli forms underneath stratus cloud. The dashed line represents the wet adiabat.

the boundary heights lower than those measured on the clear side. This baroclinicity produces a surface wind maximum which moves back and forth across the coast, which they call a cloud breeze. It is claimed that this cloud breeze can dominate over circulations induced by the land-sea interaction.

2.2.2 Cloud breakup

An important dynamic factor which has so far just been briefly mentioned is entrainment. Entrainment is the process where warm dry air from above the inversion is carried down into the boundary layer. Often entrainment can be significant enough to cause a change in boundary layer or cloud structure. Entrainment is most often caused by vertical wind shears across the boundary layer or by buoyancy fluxes near cloud top. Researchers have looked for insight into determining under what conditions entrainment will occur. Many have called these conditions the cloud-top entrainment instability (CTEI) conditions. In certain regions where CTEI criteria are met, entrainment may be large enough to cause breakup of the stratocumulus cloud layer. Lilly (1968) helped to develop the CTEI theory by saying that the CTEI criterion was met when:

$$\Delta\theta_e = (\theta_e)_{\text{inversion top}} - (\theta_e)_{\text{inversion base}} < 0. \tag{2.1}$$

Following this work, Deardorff (1980) and Randall (1980) mentioned that CTEI should include virtual temperature and liquid-loading effects. Adding these effects makes it more difficult for CTEI to be met. Kuo and Schubert (1988) included virtual temperature effects in the following way:

$$\Delta\theta_e < k\frac{L}{c_p}\Delta q_t, \tag{2.2}$$

where $k \sim 0.23$ for typical conditions and Δq_t is defined similarly to $\Delta\theta_e$.

Betts and Boers (1990) collected aircraft data and lidar data to study the thermodynamic structure of areas with different cloud cover amounts and types. They studied in detail the 7 July case of FIRE where there was a transition from west to east of a clear boundary layer, to areas of small cumulus, to an area of broken stratocumulus, to a solid stratocumulus deck. Betts and Boers found that sea surface temperatures decreased from the clear areas to the solid stratocumulus areas, while wind speeds increased underneath the stratocumulus deck. The lidar data provided the researchers with information about cloud top heights and is shown in Figure 2.3. This graph shows that in the small cumulus areas, cloud fraction is small, but cloud top height variability is large. Meanwhile, the stratocumulus deck region has small cloud top height variability and large cloud fractions. The lower cloud top heights on the clear side of the transition corresponds to a lowering of the inversion height. Figure 2.4 shows the boundary layer is thinner and the inversion weaker in the clear area than in the stratocumulus area. Betts and Boers try to determine their own CTEI and go on to show that by examining a mixing line slope, they can determine the cloudiness regimes quite accurately for this case.

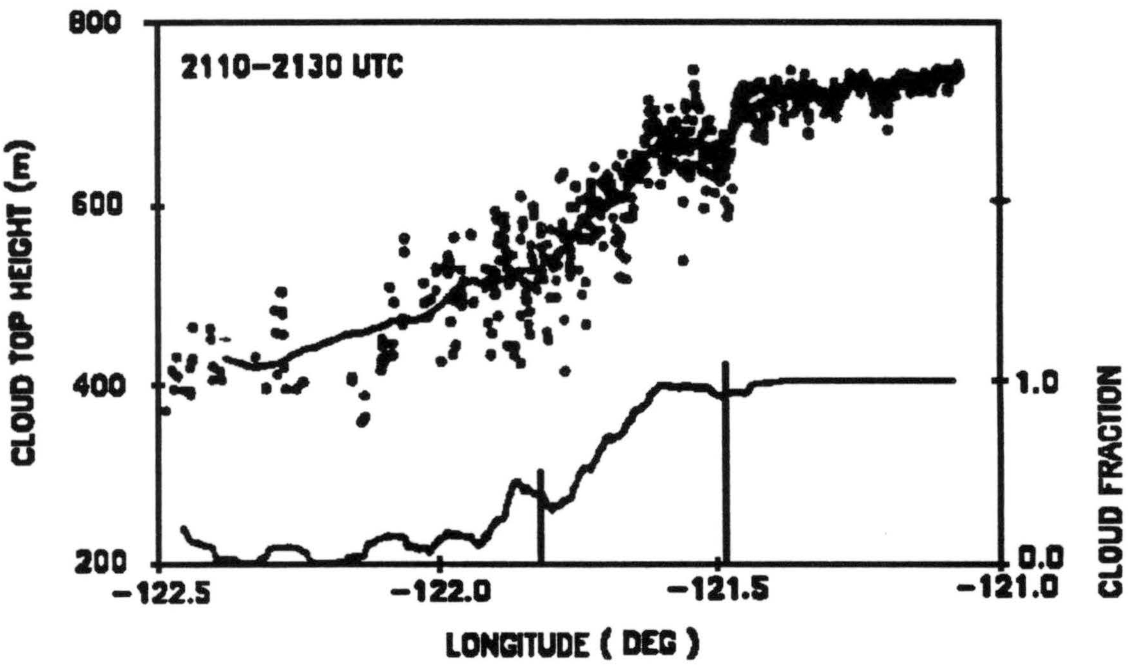

Figure 2.3: Lidar cloud top heights (dots) and cloud fraction (line) as measured 7 July 1987 (from Betts and Boers (1990)). Valid between 2110 and 2130 UTC for 31.6°N.

Albrecht (1991), however, found no correlation between mixing line slopes and the fractional cloudiness in soundings obtained during the Atlantic Trade-Wind Experiment (ATEX). His findings concur with the suggestions of Siems et al. (1990) and MacVean and Mason (1990) that the dynamics of the mixing process must be considered in addition to thermodynamic boundary conditions in order to determine cloud fraction.

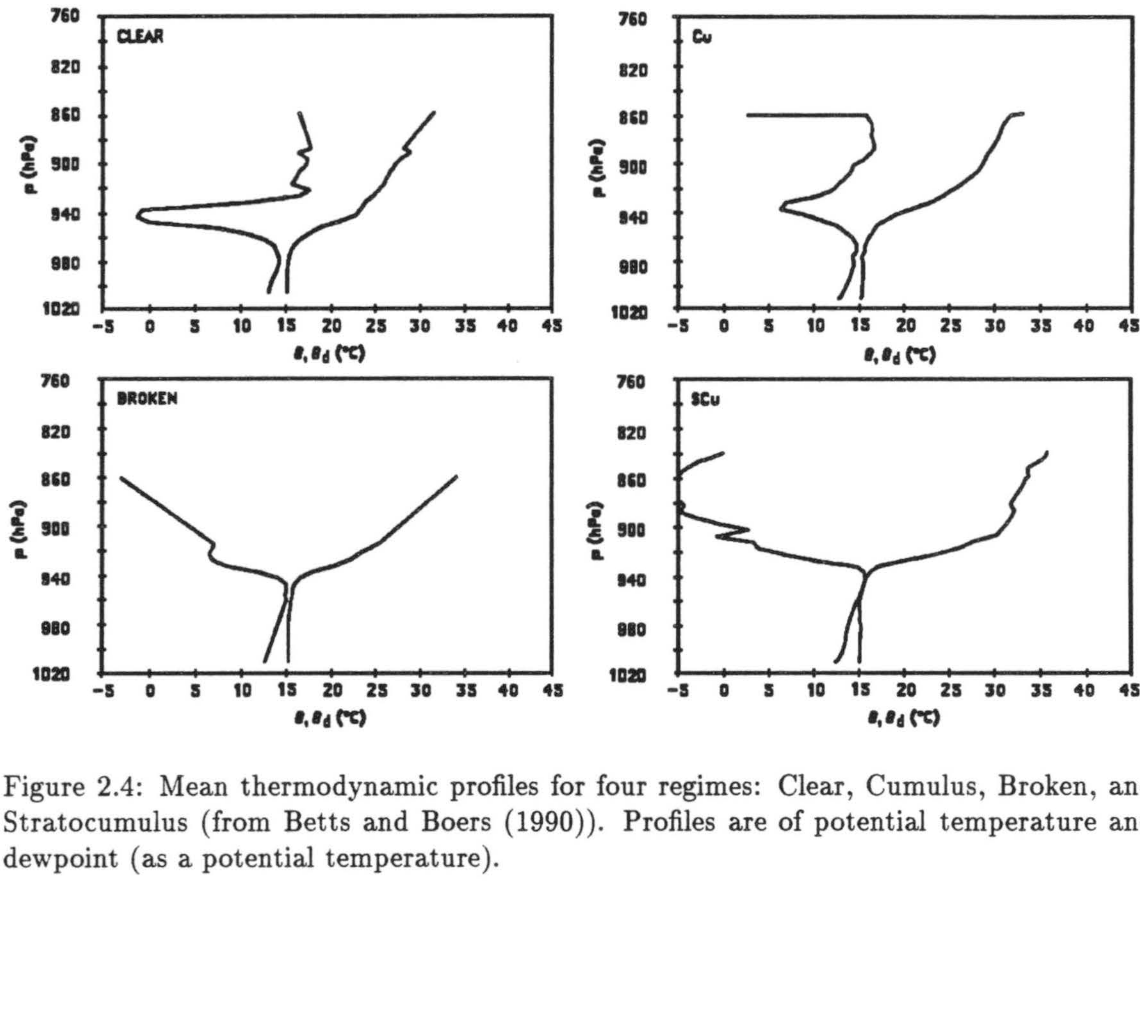

Figure 2.4: Mean thermodynamic profiles for four regimes: Clear, Cumulus, Broken, and Stratocumulus (from Betts and Boers (1990)). Profiles are of potential temperature and dewpoint (as a potential temperature).

2.3 Typical characteristics of the CBL

The convective boundary layer (CBL) is usually considered to be dry and turbulent. The main mechanism driving this turbulence is buoyancy. This buoyancy is driven by heating of the surface of the earth by solar radiation. The solar radiation warms the earth's surface, which then warms the air just above the surface. As this air is warmed, it becomes positively buoyant and begins to rise in the form of plumes or thermals. This rising air and the compensating sinking air give rise to updrafts and downdrafts. These up and downdrafts mix the layer and determine the profiles as seen in Figure 2.5. The mean virtual potential temperature is nearly constant with height within the mixed layer. The mean specific humidity is larger near the surface than near the inversion as a result evaporation of surface moisture. The mean wind is found to increase from the surface to the inversion layer. Typically, the mean wind is sub-geostrophic. Just above the boundary layer is a capping inversion. This inversion is marked by a strong increase in virtual potential temperature, by a strong decrease in specific humidity, and by a return to geostrophic flow of the mean wind.

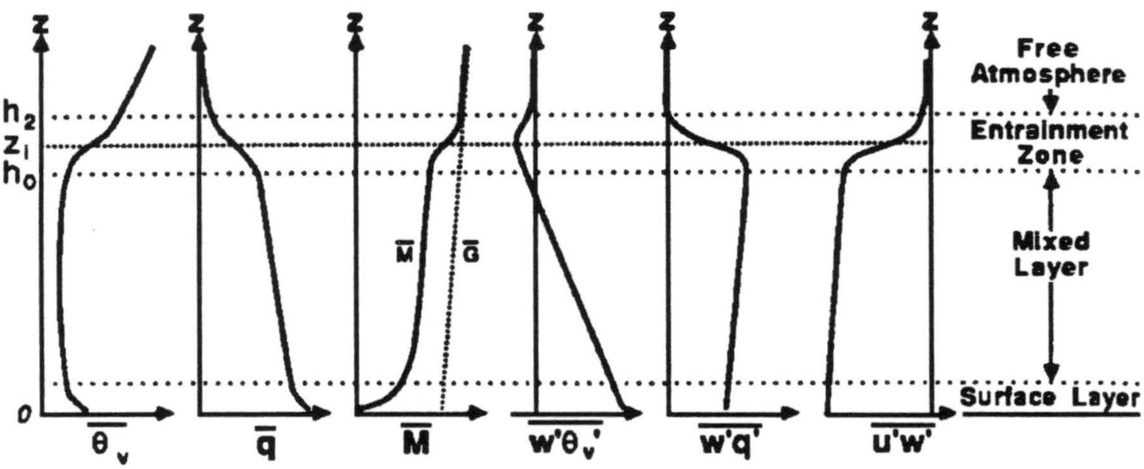

Figure 2.5: Mean conditions within the convective boundary layer (from Stull (1988)). $\overline{\theta_v}$ - mean virtual potential temperature; $\overline{q}$ - mean specific humidity; $\overline{M}$ - mean wind speed; $\overline{G}$ - geostrophic wind speed; $\overline{w'\theta_v'}$ - heat flux; $\overline{w'q'}$ - moisture flux; $\overline{u'w'}$ - momentum flux.

In the CBL, the updrafts and downdrafts have varying area fractions, velocities, and temperatures. The updrafts typically take an area fraction in the horizontal of less than half. The vertical velocity magnitude is larger for updrafts and thereby exhibit larger mass fluxes. Also, the updrafts tend to be warmer than downdrafts, as a result of the surface warming.

2.4 Previous modeling studies

Many models have been developed to study both the STBL and CBL. One type of model that can be used is a simple mixed layer model. In this model, certain physical parameters (such as virtual potential temperature and moisture) are assumed to be constant through the layer. The main advantages of these models are that they are simple to program and do not consume a great deal of computer resources. The main disadvantage of these models is that they are not versatile. If the layer departs from a well-mixed state, then the model is no longer valid. For example, if there is drizzle from the cloud, then the layer is no longer well-mixed. Other models that can be used include the mesoscale model and the large-eddy simulation (LES) model. The mesoscale model may be run in one, two, or three dimensions, depending on the complexity desired. The LES can be applied to either the STBL or the CBL as well.

Some previous studies have included a formulation of the fractional cloudiness. Typically, the fractional cloudiness scheme was designed specifically for the model in which it was implemented. This chapter will not describe the schemes themselves, but provide a brief overview of the modeling of the boundary layer and its fractional cloudiness.

2.4.1 Modeling the boundary layer

Chen and Cotton (1987) used a one-dimensional second-order closure model to simulate the same days/cloud conditions as Brost et al. They found the clouds were mostly buoyancy driven. When the model winds above the mixed layer were increased from geostrophic velocities, however, to observed velocities, the cloud became shear driven. Many sensitivity experiments were performed. A few of the sensitivity experiments also caused the cloud to become shear driven: when the radiation model was turned off; when there was significant subsidence above the capping inversion; and when there were high clouds above the stratocumulus (which reduced long wave cooling). Chen and Cotton also simulated sporadic entrainment. Through the use of additional sensitivity experiments, it was determined that this sporadic entrainment is controlled by drizzle, by long wave cloud top cooling, and by vertical wind shear.

Diurnal variation sensitivity experiments were also performed and they seemed to agree well with observations as noted previously. Chen and Cotton found that short wave heating was maximized 100 m down from cloud top, while long wave cooling was maximized 25 - 30 m down from cloud top. Because the long wave cooling is a maximum closer to cloud top, no descent of the cloud top after sunrise was found, although cloud base did rise. Chen and Cotton also demonstrated that subsidence warming can counteract radiative cooling at cloud top, which may breakup the clouds. They also show that the presence of mid- or high-level clouds can also cause the dissipation of the stratocumulus layer by reducing the radiative cooling and thus the liquid water content at cloud top.

Schumann and Moeng (1991 a & b) ran simulations of the CBL with their large-eddy simulation (LES) model. Looking at the fluxes and budgets in the CBL, Schumann and Moeng isolated the effects of various terms by using a plume-averaged LES. For instance, it is found that the updrafts are mainly driven by buoyancy. Mean vertical pressure gradient also affects the motion, accelerating upward motion in the lower half and decelerating it in the upper half of the layer. In the downdrafts, pressure forcing is the main driving force. When considering the kinetic energy budget, the authors find that the vertical buoyancy flux provides the main source of energy, while dissipation is the primary sink term. For the downdrafts, all terms of kinetic energy are smaller in magnitude, except for mixing, which is the main energy source in the upper part of the downdrafts.

Schumann and Moeng (1991a) also found that the area fraction of updrafts and downdrafts in the STBL was roughly equal, about 0.28 to 0.29 each. Thus, the velocity for both up and down is about the same, which differs from the CBL where the updraft velocity is larger. This symmetry between the up and downdrafts is not evident in the CBL as it is in the STBL because the STBL is driven by radiative cooling at the top of the layer and/or by surface heating at the bottom of the layer. They also found that horizontal length scales of both the updrafts and downdrafts were larger in the STBL than they were in the CBL. There is a moisture difference between updrafts and downdrafts in the STBL which is not present in the CBL. Updrafts in the STBL have more moisture, especially at the surface, as a result of surface evaporation. Schumann and Moeng found that this difference decreases away from the surface due to mixing between the drafts, but becomes large again at cloud top where the downdrafts pull in dry air from above the inversion. The CBL and STBL have in common, however, the fact that updrafts are warmer than downdrafts as a result of surface heating.

It is possible to further compare the CBL and STBL using numerical simulations. Considering the amount of mixing in each layer, one would find that mixing is high in both the STBL and the CBL, with the mixing in the STBL being slightly larger. This, again, is from the radiative cooling/latent heat release in the cloud layer and heating at the surface, which intensifies the circulation both near the inversion and at the ground. Examining the pressure profiles of updrafts and downdrafts, it is shown that the downdrafts have a larger pressure deviation than do the updrafts. The higher pressure in the downdrafts is more pronounced in the STBL than it is in the CBL. Reasons for this are the increased circulation as well as the larger horizontal scale for updrafts and downdrafts in the STBL (Schumann and Moeng, 1991b). Another thing to consider is the relationship of free atmosphere air to the boundary layer. In the CBL, updrafts often "shoot past" the inversion due to inertia. As they do, air from above the inversion is often mixed in. For the STBL, the compensating updrafts will push against the inversion, but not break through, although some entrainment will occur as the updrafts are at the inversion. Then, as this air is radiatively cooled, it horizontally converges and sinks due to its negative buoyancy. As it sinks, it can carry some entrained warm air. Nicholls (1989), however, found that these downdrafts contain only a small percentage of free atmosphere air, on average.

2.4.2 Modeling fractional cloudiness

The first implementation of the fractional cloudiness parameter within a computer model was done for the modeling of moist convection on the mesoscale. Sommeria and Deardorff (1977) and Manton and Cotton (1977) separately developed a fractional cloudiness scheme built around subgrid-scale condensation. Their work has been further updated, including additional studies by Bechtold et al. (1992), and by Bechtold et al. (1993). These schemes are most applicable for models with horizontal grid spacing on the order of 50 m.

Sundqvist et al. (1989) used a simple relation between relative humidity and fractional cloudiness for their mesoscale model. Kvamstø (1991) advanced this work, using observed satellite data to predict model parameters to develop a separate fractional cloudiness scheme. Based on the model output, Kvamstø found a relationship between the relative humidity in the model and the observed fractional cloudiness. The model used by Kvamstø had a horizontal grid spacing of 50 km.

A relation between relative humidity and fractional cloudiness is very easy to put into a numerical model. Other studies into this relation include Mitchell and Hahn (1990), Saito and Baba (1988), Slingo (1980, 1987), and Chu (1986). Other mesoscale models use a set of prognostic equations for cloud water species together with a diagnostic relation for the fractional cloudiness (e.g., Ballard et al. (1991) and Pudykiewicz et al. (1992)). Ek and Mahrt (1991) also relate the relative humidity to the fractional cloudiness. This study is different in that it includes both turbulent and subgrid mesoscale variations of relative humidity in its formulation of fractional cloudiness.

Bulk boundary layer models have also included a formulation of fractional cloudiness. Shao (1994) diagnosed the fractional area covered by updrafts. The fractional cloudiness was determined when updrafts were saturated and downdrafts were not saturated.

Work has also been done in bringing a fractional cloudiness amount into a general circulation model. Among these are Smith (1990), Le Treut and Li (1991), and Smith and Randall (1992). These schemes also use prognostic cloud water species equations with a diagnostic fractional cloudiness relation.

For this study, many different schemes that can be applied to a mesoscale numerical model were tested against each other. This study will be the one of the first times that fractional cloudiness schemes built independently of each other will be directly compared.

Chapter 3

RAMS CONFIGURATION

The Regional Atmospheric Modeling System (RAMS), developed at CSU, is a highly flexible atmospheric model that is based on an earlier hydrostatic mesoscale model (Mahrer and Pielke, 1977) and a non-hydrostatic cloud model (Tripoli and Cotton, 1982). Further descriptions of the model may be found in Cotton et al. (1982, 1986), Tripoli and Cotton (1982), Tremback et al. (1986), Tripoli (1986), Tremback (1990), Pielke et al. (1992), and Nicholls et al. (1993). This chapter provides a detailed description of the configurations used in this study.

There are three distinct components to RAMS. The first is the ISentropic ANalysis (ISAN) package, which handles model initialization; the second is the RAMS model itself, which performs the model simulation; and the third is the Visualization and ANalysis (VAN) package, which does the post-processing.

3.1 ISAN

The ISAN package is used to create model-compatible observations from outside data sources. The first step of the process is to combine all horizontal wind, temperature, and moisture data onto a pressure level data set. The second step is to combine surface observations and rawinsondes with the pressure data and build an isentropic data set. A Barnes (1973) objective analysis is performed on the data at this time to smooth the model fields. The final step is to interpolate the isentropic data onto model-compatible grid points. The first two steps of this process were performed on the Cray/YMP at the National Center for Atmospheric Research (NCAR) in Boulder. The final step was performed on an IBM/RISC 6000 at CSU. A further description of the ISAN package can be found in Tremback (1990), Cram (1990), and Pielke et al. (1992).

For this study, the NMC data set as archived at NCAR was used. This data set contains NMC rawinsondes, surface aviation observations (SAOs), and mandatory pressure level global analyses.

For the FIRE I experiment, three different isentropic data sets were generated using the NMC archived data. The first data set, valid at 0000 UTC 7 July - the start of the simulations, was used to initialize the model at every grid point. The next two data sets, valid at 1200 UTC 7 July and 0000 UTC 8 July - the end of the simulations, were used to nudge the model's lateral grid points.

3.2 Model

The RAMS model is continually being refined and improved. For this study, Version New-2C of RAMS was used.

During the running of the model, analysis and history files are generated. The history files are used to re-start the model in the event of a crash or if the model is to be run in time blocks. The analysis files are used by the VAN package to generate plots of the model results.

3.2.1 Variables

RAMS integrates the model equations forward in time. The non-hydrostatic version of RAMS was chosen. This version predicts wind components u, v, and w, the ice-liquid water potential temperature θ_{il}, the dry air density, total water mixing ratio r_t, and the mixing ratios of the following water species: rain, pristine ice, snow, aggregates, and graupel. From these variables, pressure, temperature, potential temperature, cloud water mixing ratio and vapor mixing ratio are diagnosed.

An additional predictive variable was added to this version. Dr. Michael Weissbluth's cumulus parameterization (Weissbluth and Cotton, 1993) was added to the RAMS code, using only the small-scale turbulence parameterization; not the deep convection model. This turbulence parameterization adds $\overline{w'w'}$ as a predictive variable. A more detailed description will be found in the Parameterizations section of the model description.

3.2.2 Grids

RAMS uses the standard Arakawa-C grid (Arakawa and Lamb, 1981) which is staggered in the horizontal and vertical directions. The velocity components are valid at the faces of the grid-volume. Scalar variables are valid at the center of the grid-volume. A polar stereographic horizontal projection of the grid was used.

RAMS uses the σ_z terrain following system (Gal-Chen and Somerville, 1975) for its vertical coordinate. The vertical grid spacing can change according to user specifications. For this study, 40 vertical levels were used, with spacing of 75 m from the ground to 1 km, stretched to the model top of 15.5 km.

It is also possible to nest grids using RAMS. When nesting, a portion of a larger grid with coarser grid spacing contains a smaller grid with finer grid spacing. With RAMS, unlimited nests can be used; either many grids separately within a main grid, or finer and finer grids within each other within a coarse grid. Typically, two-way interactive nesting between grids is used. Two-way interactive nesting means that the outer grid forces the inner grid, and after the inner grid is integrated forward in time, the inner grid information is averaged and supplants the outer grid information.

3.2.3 Numerics

This version of RAMS used the second order leapfrog time differencing scheme with an Asselin filter and a time split scheme (Klemp and Wilhelmson, 1978). The time split scheme integrates the acoustic terms on a small time step and all other terms on a long time step. The ratio chosen between long and short time steps was 3:1. For the FIRE I experiment, the long time step for the outer grid was 60 seconds, for the middle grid it was 30 seconds, and for the inner grid it was 15 seconds.

3.2.4 Parameterizations

When using atmospheric models, certain calculations can be very time consuming. Therefore, it is necessary to use parameterizations to save the cost of making detailed physics calculations. The RAMS model has many different parameterizations which can be used in various ways according to the specific needs of the simulation. The following is a brief description of the parameterizations used for this study.

Eddy Diffusion

The horizontal eddy diffusion coefficients were calculated using a deformation K rate equation similar to Smagorinsky (1963). Vertical eddy diffusion was calculated by the Weissbluth 2.5w turbulence parameterization.

Radiation

The radiation calculations for both long and short wave radiation are described in Chen and Cotton (1983). This scheme considers the effects of water vapor, ozone, carbon dioxide, and condensate. Calculating the effects of condensate on the radiative transfer can be computationally expensive. Accounting for the reflection and absorption of short wave radiation by boundary-layer clouds (especially a solid stratocumulus deck), however, has been shown to be important. The radiation calculations were updated every 900 seconds.

Microphysics

The RAMS model handles moisture calculations in one of the following four ways (Flatau et al., 1989): 1) completely dry, 2) using moisture as a passive tracer, 3) condensing any supersaturation into liquid water, and 4) microphysics. Microphysics has the highest complexity of the moisture options, but it allows the user to predict or specify individual ice and water species.

For this study, the mixing ratio of rain r_r was predicted and the presence of the other microphysical species were not allowed. Allowing only rain is a valid assumption because this study is intended to focus on the development of boundary-layer clouds. For all of the simulations performed, it was found that all condensed moisture existed at heights below the freezing level. The mean diameter of the rain species was specified at 10^{-4} m. The aerosol characteristics used in the model runs were consistent with characteristics typically observed in a marine stratus environment.

Surface boundary conditions

The surface layer scheme described by Louis (1979) was used in this study. A prognostic soil model developed by Tremback and Kessler (1985) was also used for the land areas within the model domain. The soil model contained 11 layers down to 1.3 m below the surface. Every effort possible was made to initialize the soil temperature and moisture profile consistent with the start and area of the simulation. The model code was modified to allow the horizontally inhomogeneous initialization of vegetation cover and roughness length. The vegetation data was obtained from a USGS 1 km by 1 km map and the corresponding roughness length was obtained from Stull (1988). Sea surface temperatures were initialized from the NCAR storage data.

The model topography was taken from a 10 minute data set for the synoptic grid and from a 5 minute data set for all the other grids. The model land percentage was taken from the same data sources. The finest grid for the stratocumulus simulations was entirely over the ocean (thus, the relative coarseness of the 5 minute data set was not important). The sharp changes in terrain height over the western 1/3 of the U.S., however, caused problems during the running of the model for the FIRE I simulations. The 75 m vertical spacing in the lowest levels of the model proved too small for the model to handle over steep topography. This problem was solved by increasing the wavelength cutoff filter and shutting off the silhouette averaging within the model topography.

Top boundary condition

As a top boundary condition, this study chose the "wall on top" option. The "wall on top" requires that the vertical velocity w is equal to zero at the top model level. This requirement can have the adverse effect of reflecting gravity waves off the model top. It did not prove to be a problem, however, as no significant gravity waves were observed in the upper portion of the model throughout all simulations.

Lateral boundary conditions

Because this implementation of RAMS is not global in nature, information at the edges of the largest grid must be accounted for. During the running of the model, certain features may leave the model domain and other features may enter the model domain. The appearance and disappearance of these features was taken into account by nudging the solutions of the outermost grid points to the grid information generated by using the

ISAN package. The Davies nudging scheme specified the boundary conditions on the five outermost grid points on the course grid. Through the use of user-defined weighting factors, each grid point, when integrated forward in time, was nudged towards its "solution" at the time of the nudging file.

Turbulence

A unique feature used in these simulations is that the model used a small-scale turbulence scheme that predicts on vertical velocity variance. Using Mellor and Yamada's (1974) terminology, a Level 4 second-order closure model has prognostic equations for all variances and covariances, while the Level 3 model has prognostic equations for only turbulent kinetic energy, TKE, and the variance of potential temperature. The Level 2.5 model has only a prognostic equation for TKE. Like the Level 3 model, the Level 2.5 model diagnoses the other variances and covariances. Weissbluth and Cotton's (1993) parameterization is called Level 2.5w because it is a Level 2.5 closure that predicts on vertical velocity variance instead of TKE. The Zeman and Lumley (1976) formulation is used to close the pressure term and eddy transport term using the buoyancy-driven mixed layer.

There are several advantages to closing the equations on vertical velocity variance instead of TKE. The first is that the mean horizontal and vertical winds can explicitly advect $\overline{w'w'}$ or TKE. This allows adjacent grid-volumes to easily exchange information about convective activity. Another advantage is that shear can influence $\overline{w'w'}$ because it is advected by the mean winds. This allows the solution of the shear production term in the tendency equation for $\overline{w'w'}$. A third advantage is that the vertical velocity variance seems to behave similarly for differing modes of convection. Weissbluth (1991) showed that the vertical profile of $\overline{w'w'}$ was very similar for tropical squall lines and mid-latitude supercells. He also showed that the profile of $\overline{w'w'}$ is similar to the profile of the vertical convective fluxes of total water r_t and ice-liquid potential temperature θ_{il}. One final advantage of the Weissbluth parameterization is that his scheme can provide cumulus source functions for all hydrometeor species. For more information on this parameterization, the reader is referred to Weissbluth (1991).

In addition to the benefits already mentioned, it was chosen to use the Weissbluth small-scale turbulence parameterization because it can provide turbulence parameters, diagnostically, that will be needed to calculate fractional cloudiness for some of the schemes to be tested. These parameters can only be provided from a Level 2.5 model or greater. Without going into too much mathematics from the Weissbluth parameterization, the variances that will be needed and what they are set to are:

$$\begin{aligned}
\overline{w'r_t'} &= -lqS_h\frac{\partial\overline{r_t}}{\partial z}, \\
\overline{r_t'r_t'} &= B_2 l^2 S_h \frac{\partial\overline{r_t}}{\partial z}^2, \\
\overline{\theta_{il}'\theta_{il}'} &= B_2 l^2 S_h \frac{\partial\overline{\theta_{il}}}{\partial z}^2, \\
\overline{r_t'\theta_{il}'} &= B_2 l^2 S_h \frac{\partial\overline{r_t}}{\partial z}\frac{\partial\overline{\theta_{il}}}{\partial z},
\end{aligned} \tag{3.1}$$

where $q^2 = \overline{u_i'u_i'}$ is the TKE, l is the master length scale, B_2 is the dissipation length scale, and S_h is the eddy heat exchange coefficient. The RAMS model code was modified to allow this information to be saved in the model-generated analysis files.

3.2.5 Domain

The model domain used for the California stratocumulus case study was centered over the FIRE I target area. The coarse grid with 80 km horizontal grid spacing covers the extreme eastern Pacific ocean and western 1/3 of the U.S. There is a nested middle grid with 20 km horizontal grid spacing very close to the center of the coarse grid. The outermost two grids are shown in Figure 3.1.

Inside the middle grid is another nested grid. This fine grid has 5 km horizontal grid spacing. The domain of the smallest grid was especially chosen to match the domain of satellite imagery showing the cloud transition. The innermost two grids are shown in Figure 3.2.

3.3 VAN

The VAN package uses the model-generated analysis files to generate plots of the model forecast fields. VAN uses NCAR graphics plotting routines to help make the plots. Many

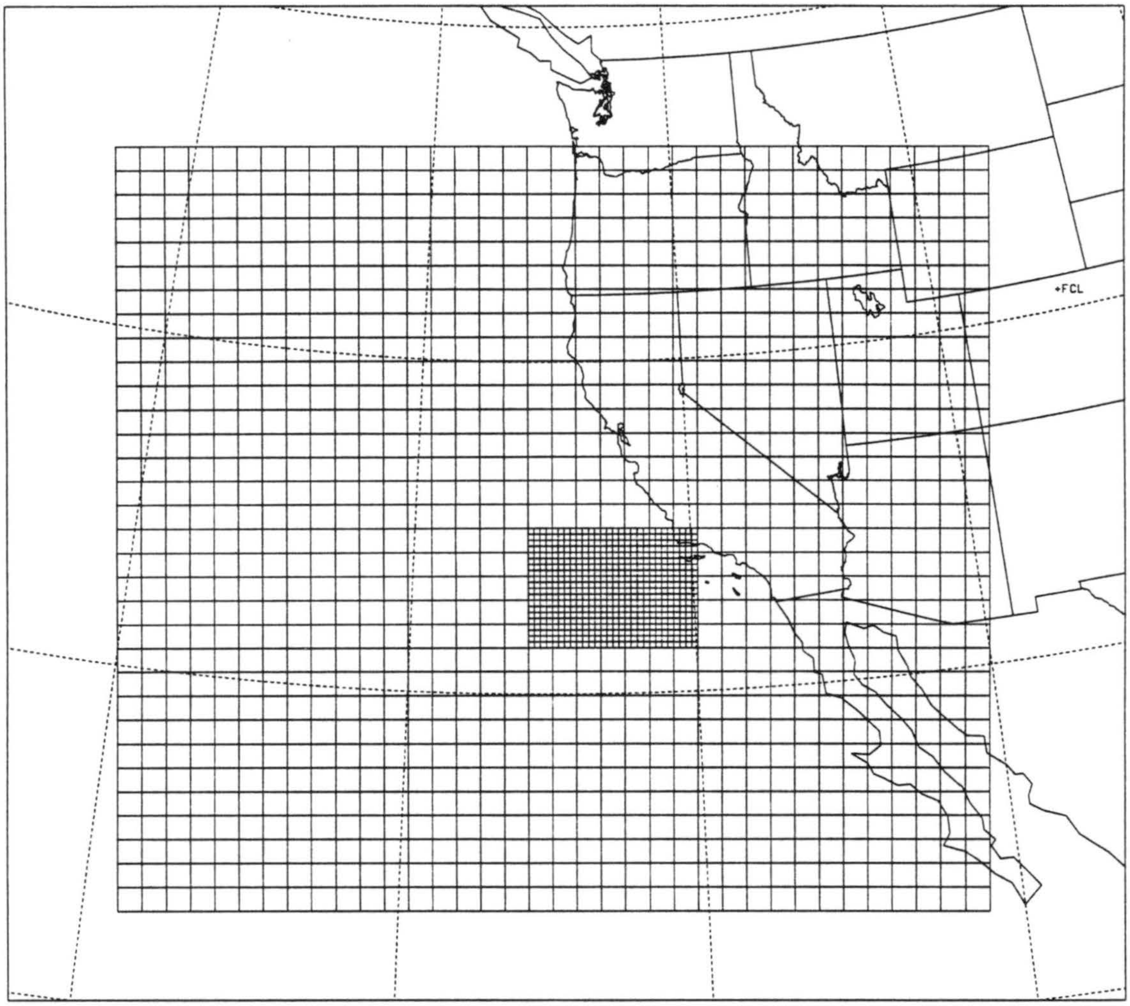

Figure 3.1: Grids showing domain of first and second grids from the RAMS configuration.

of the desired fields to be plotted are in the standard Version New-2C code. However, other fields were coded to enhance the range of variables that can be plotted with the VAN package. This includes adding a skew-T plotting option into the VAN code.

The VAN package was also where the fractional cloudiness schemes were coded into RAMS. The model-generated analysis files are used to calculate the fractional cloudiness parameter, FC. The FC did not feedback into the model's predictive equations. Nine different FC schemes were coded into RAMS. This coding proved to be the most time-consuming portion of this study. Further description of every fractional cloudiness parameterization can be found in Chapter 4.

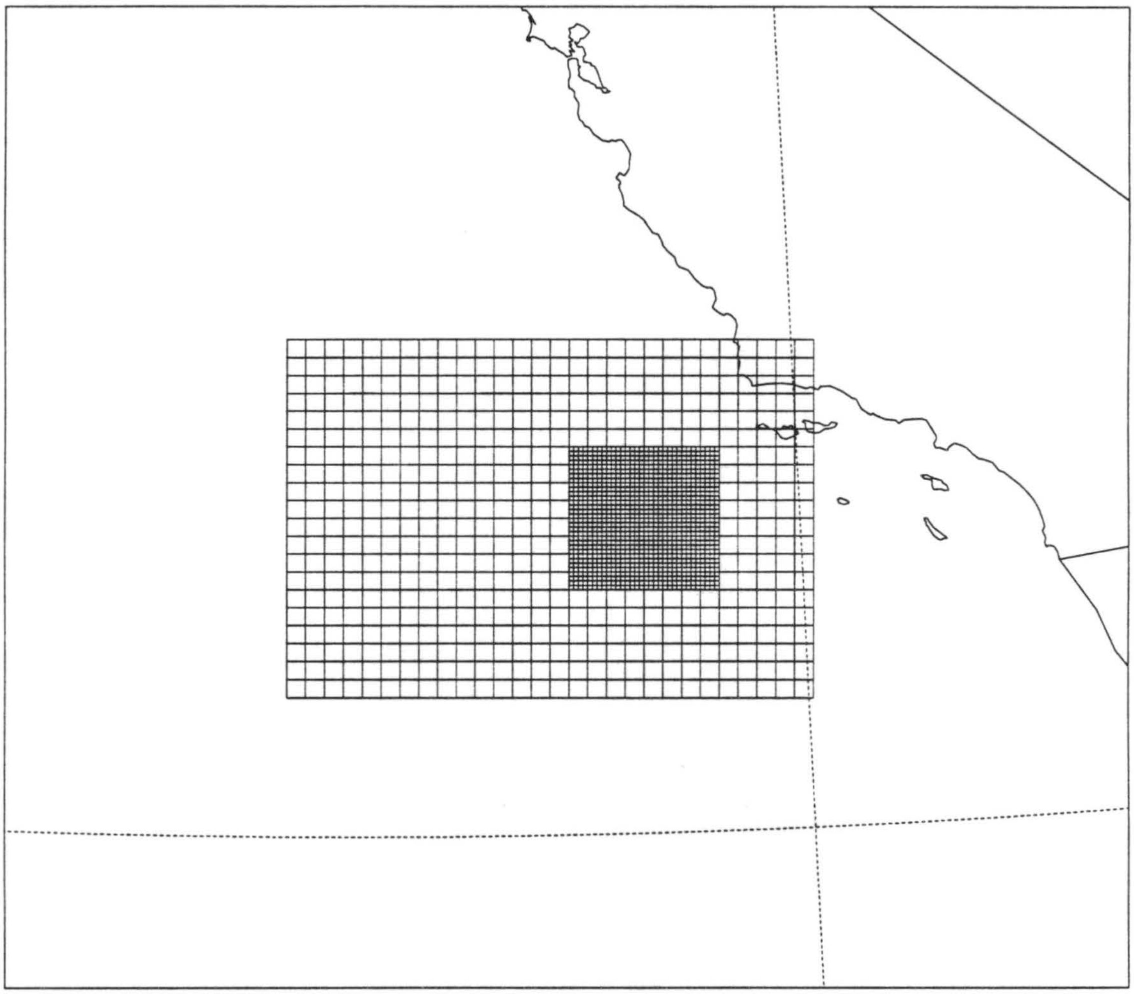

Figure 3.2: Grids showing domain of second and third grids from the RAMS configuration. The width of the innermost grid domain is about 170 km.

Chapter 4

FRACTIONAL CLOUDINESS DESCRIPTIONS

For purposes of examining the feasibility of diagnosing fractional cloudiness (FC), many different FC schemes readily found in the atmospheric science literature were evaluated. Once a FC scheme was chosen, the equations were coded into the RAMS analysis package. These equations take the information saved to the model's predicted analysis files and produce a fractional cloudiness parameter. In the model's typical configuration, the information saved to the analysis files includes u, v, w, perturbation Exner function (π'), total water mixing ratio (r_t), and θ. Because the microphysics option of RAMS was used for these simulations, the mixing ratio of rain was also saved. Subgrid-scale variances and co-variances that can be obtained from Weissbluth's turbulence scheme were needed for the calculation of some of the FC schemes, and were thus saved as well. All of the FC schemes chosen were diagnosed from the information above.

The fractional cloudiness parameter is defined to be between 0.0 and 1.0. Zero represents a grid-volume that is diagnosed to be completely free of cloud. One represents a grid-volume that is diagnosed to be completely encompassed with cloud. A value of 0.5 will therefore represent a grid-volume that is half-filled with cloud.

The FC parameter is intended to be provide a measure of cloud amount when the model's grid spacing does not allow an explicit simulation of the cloud field. RAMS allows the modeller to diagnose cloud water. For RAMS to produce cloud water in a grid-volume, however, that grid-volume must be completely saturated (RH goes to 100%). The FC parameter allows the possibility for scattered clouds, whose extent may be less than the model's grid spacing, to be diagnosed. These scattered clouds, while not necessarily being explicitly predicted by the model, can be an important component of the model's solution and affect forecast features such as surface heating, cloud radiative heating and cooling, and visibility.

The reason this study was undertaken was to provide RAMS with a fractional cloudiness parameterization that can be applied to the model's prognostic equations. As mentioned previously, a cloud fraction amount can be used to better represent model calculations such as radiation - which can in turn affect other model variables. It is intended that one of these fractional cloudiness schemes will eventually become part of the model's standard framework.

These parameterizations can be applied to other nested-grid mesoscale models with grid spacings ranging from 5 to 100 km. Even general circulations models (GCMs) can apply the results given in this work.

There are many varieties of FC schemes. The simplest ones simply diagnose the FC as a function of relative humidity. Others use mixing line slopes through the depth of the boundary layer. The model's grid spacing can also be accounted for in some schemes. Finally, some FC schemes use subgrid-scale turbulence parameters. This chapter provides a detailed description of every FC scheme encoded in this study.

4.1 As a function of RH

Some of the first fractional cloudiness schemes put into the RAMS code turned out to be some of the easier to encode. These diagnose the FC solely as a function of the moisture content in the grid-volume. Typically, the relative humidity (water vapor mixing ratio over saturation vapor mixing ratio) is used. Because RAMS diagnoses cloud water as a result of any total water greater than the grid-volume's saturation vapor mixing ratio, the greatest value of RH that can be obtained in any grid-volume is 100%.

4.1.1 Albrecht

The first scheme is from Albrecht (1989). He parameterized the FC amount to be a simple ratio involving the liquid water content and relative humidity of the grid-volume:

$$FC = \frac{(SR-1)}{(SR-RH)}, \tag{4.1}$$

where SR is the ratio of the total water (both liquid and vapor) mixing ratio to the saturation vapor mixing ratio.

Albrecht claims that in an environment with a high RH, cloud elements will be long-lived, and the FC will be high. If the environment has a small SR (just barely over one), the liquid-water content of the cloud elements will be small, and the FC will be low. Albrecht (1981) concludes that for typical conditions near where clouds are observed, RH will be between 0.8 and 1.0 and SR will be between 1.0 and 1.2. A graphical depiction of the dependence on FC of RH and SR in Albrecht's scheme can be found in Figure 4.1.

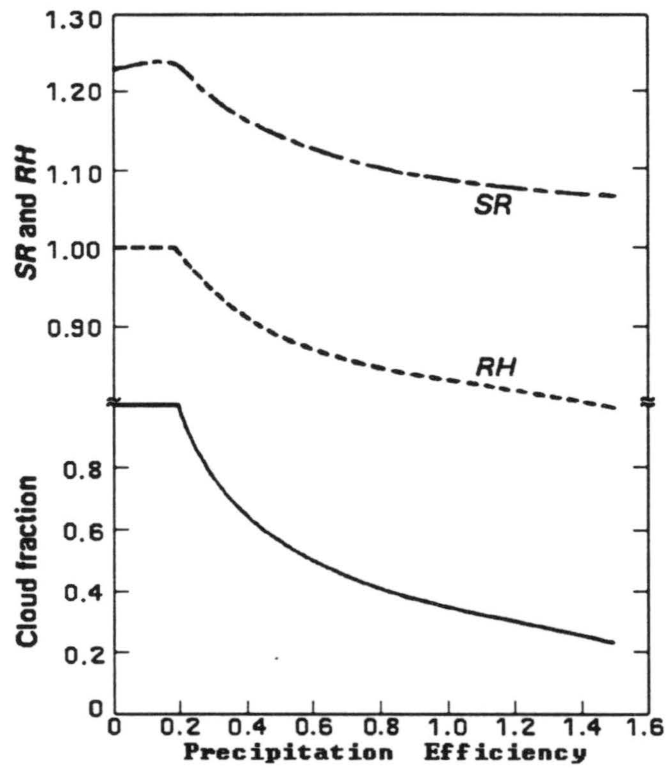

Figure 4.1: Dependence of RH and SR on FC-Albrecht (from Albrecht,1989).

4.1.2 Kvamstø

The next two FC schemes inserted into RAMS are very similar. Both of these diagnose solely on relative humidity found in the grid-volume. Kvamstø (1991) used the following relation:

$$FC = \left(\frac{FC_{max} - FC_{min}}{RH_S - RH_{00}}\right)(RH - RH_{00}), \tag{4.2}$$

where $FC_{max} = 1.0$, $FC_{min} = 0.0$, $RH_S = 1.0$, and RH_{00} is a threshold value when condensation is allowed to take place in a grid-volume.

Kvamstø used values of $RH_{00} = 0.85$ over sea and $RH_{00} = 0.75$ over land. In the present version of the model, these were the same values used in RAMS. If the land percentage of the surface that the grid-volume was over was determined to be greater than or equal to 50%, $RH_{00} = 0.75$ was used. If the land percentage was less than 50%, $RH_{00} = 0.85$ was used. The relationship between RH and FC for this scheme over land and sea is shown in Figures 4.2a and 4.2b.

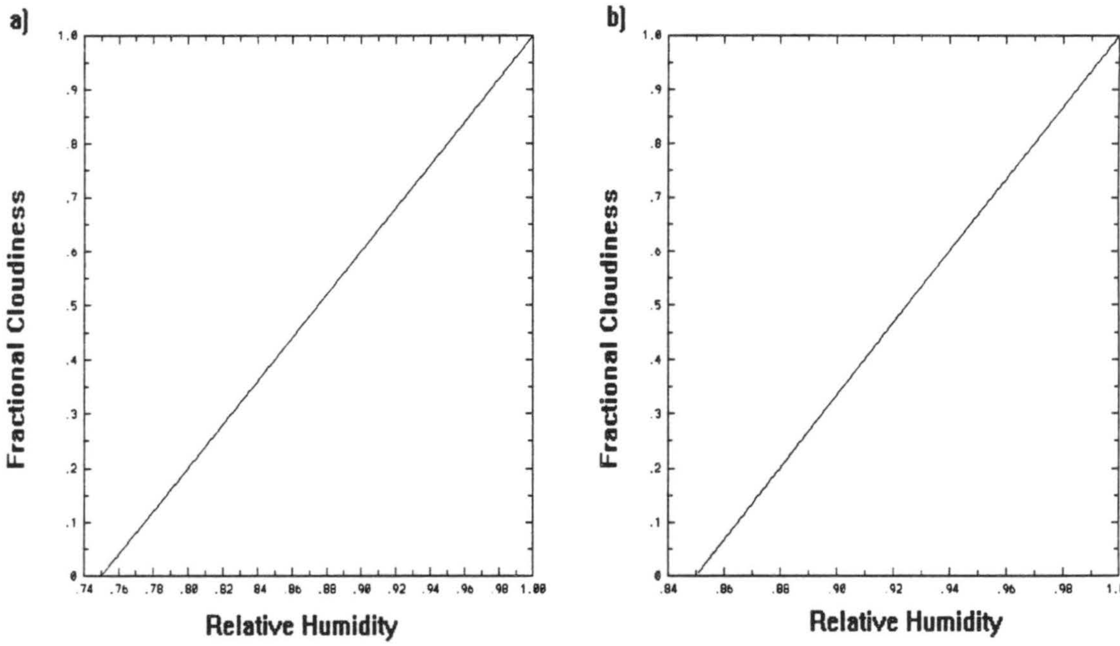

Figure 4.2: Dependence of RH on FC-Kvamstø for (a) over land and (b) over sea.

4.1.3 Sundqvist, Berge, and Kristjansson

Sundqvist, Berge, and Kristjansson (1989) used a diagnostic relation based on the same parameters as Kvamstø (1991). Their FC equation is:

$$FC = 1 - \left(\frac{RH_S - RH}{RH_S - RH_{00}}\right)^{1/2}, \tag{4.3}$$

where all parameters are the same as from Kvamstø, and the RH_{00} values used in RAMS are also as before.

The relationship between RH and FC for this scheme for over land and sea is shown in Figures 4.3a and 4.3b.

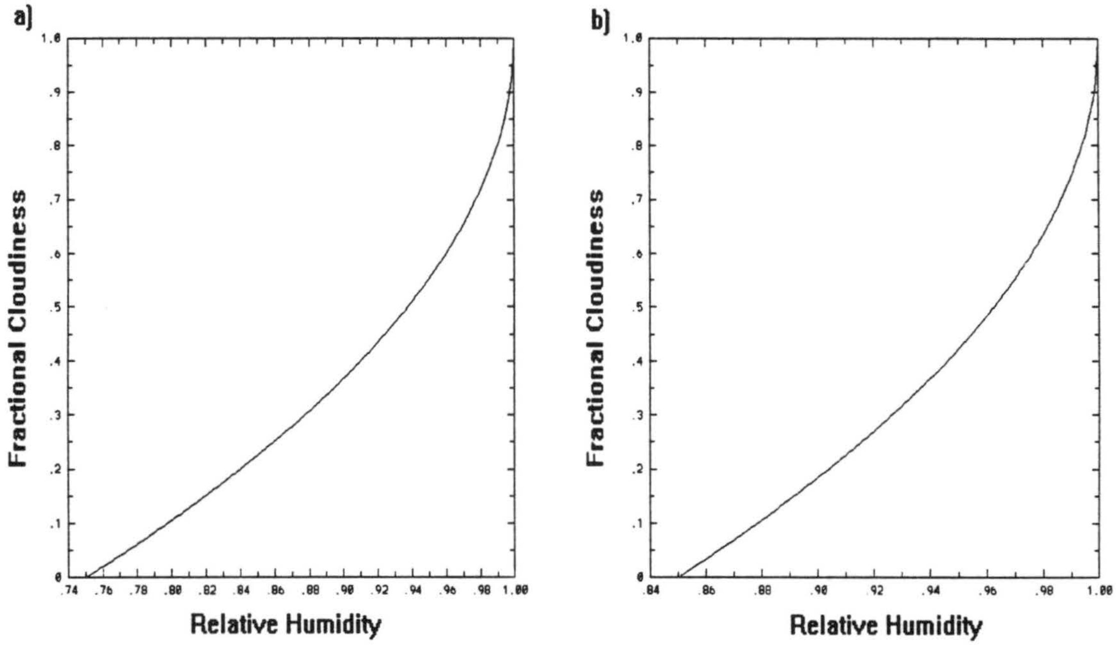

Figure 4.3: Dependence of RH on FC-Sundqvist et al. for (a) over land and (b) over sea.

4.2 As a function of mixing line slopes

The following two schemes apply exclusively to the clouds within the boundary layer. They use mixing line slopes through the depth of the boundary layer. These mixing line slopes are defined to be the mean slope of a linear regression line through a plot of (θ^*, r^*) points of data underneath the inversion. Betts and Boers (1990) attempted to find a relationship between these slopes and the fractional cloudiness parameter.

4.2.1 Betts and Boers - wet adiabat

For their FC schemes, Boers and Betts (1988) use a saturation point structure. In this structure, r^* is the total water mixing ratio, while θ^* is the potential temperature for unsaturated air or the liquid-water potential temperature for saturated air. The *'s represent the value of the variable at the saturation pressure, which is defined as the atmospheric pressure where the parcel has reached saturation after undergoing adiabatic ascent, if the parcel is originally subsaturated, or adiabatic descent, if the parcel is originally supersaturated. The mixing line slope is then given by:

$$\Gamma_m = \partial\theta^* / \partial r^*. \tag{4.4}$$

The authors normalize the mixing line slope with the wet adiabat, a line of constant equivalent potential temperature. The slope of the wet adiabat is given by:

$$\Gamma_w = (\partial\theta^* / \partial r^*)_{\theta_e^*} = -(L\theta^* / c_p T^*). \tag{4.5}$$

A typical slope of the wet adiabat is -2.6 in the lower troposphere, because θ^* is close to T^* for pressures greater than 800 mb.

Using the 7 July 1987 FIRE data set, Betts and Boers (1990) examined aircraft data through the target area and across the transition zone. They found significant changes in mixing line slopes across the four main areas of cloud conditions: clear, cumulus, broken, and solid stratocumulus. These different slopes are listed in Table 4.1. Also found in the Table are the mixing line slopes normalized by both the wet adiabat and wet virtual adiabat.

Table 4.1: Mixing line slopes and adiabats for four cloudiness regimes, including error estimates (from Betts and Boers, 1990).

Cloud region	Γ_m	Γ_m/Γ_w	Γ_m/Γ_{wv}	Cloud Fraction (%)
Clear	-0.95 ± 0.01	0.36 ± 0.01	0.45 ± 0.01	0
Cumulus	-1.03 ± 0.08	0.39 ± 0.03	0.49 ± 0.04	12
Broken	-1.39 ± 0.08	0.53 ± 0.03	0.66 ± 0.04	73
Stratocumulus	-1.85 ± 0.07	0.70 ± 0.03	0.87 ± 0.04	99

Betts and Boers next plotted the cloud fraction as a function of the normalized mixing line slopes. From this plot, they determined a regression line which helped them to determine a quick parameterization for the change in cloud fraction. Including error estimates, their equation for cloud fraction based on mixing line slope normalized by the wet adiabat is:

$$FC = (0.5 \pm 0.18) + (3.2 \pm 0.6)(\Gamma_m/\Gamma_w - 0.49), \tag{4.6}$$

where the correlation value of the fit of the linear regression line is 0.84.

In its application to RAMS, the top of the boundary layer was determined to be the level at which the vertical velocity variance as predicted by Weissbluth's scheme approached zero. The mixing line slope was then calculated from the lowest model level to the level just below the top of the boundary layer. The range of vertical levels over which the slope was calculated was independently determined for every (x, y) point in the model. For example, the mixing line slope over the ocean could be through model levels 1 to 6, while over the land, the slope could be through levels 1 to 9. The slope of the mixing line was taken from a least-squares fit of the model data over these model levels.

The slope of the wet adiabat is a function of θ^* and T^*. The model level that these variables were taken from for every (x, y) point was simply the middle vertical level of the boundary layer depth as predicted by Weissbluth's scheme. This slope did not vary much between x, y, or z model points at which θ^* and T^* were calculated.

Because slopes were used through the depth of the boundary layer for this scheme, only a grid-column fractional cloudiness was calculated, not a grid-volume fractional cloudiness. Therefore, the fractional cloudiness from Betts and Boers's schemes is the percentage of the (x, y) column through the depth of the boundary-layer that is covered with clouds.

4.2.2 Betts and Boers - wet virtual adiabat

Betts and Boers (1990) also normalized the mixing line slope with the wet virtual adiabat. The wet virtual adiabat, which is a line of constant virtual equivalent potential temperature, takes into account the effects of liquid water loading in a cloudy atmosphere. The slope of the wet virtual adiabat is:

$$\Gamma_{wv} = (\partial\theta^*/\partial r^*)_{\theta_{ev}} = -L\theta^*/c_pT^*\left[1 - (\alpha + \epsilon)/(1 + 1.61\alpha)\right], \tag{4.7}$$

where $\alpha = T^* dr^*/dT^*$ and $\epsilon = c_p T^*/L$. For typical conditions, ϵ is very close to 0.12, while α is heavily dependent on the saturation mixing ratio.

The cloud fraction relation for mixing line slope normalized by the wet virtual adiabat is:

$$FC = (0.5 \pm 0.16 + (2.6 \pm 0.5)(\Gamma_m/\Gamma_{wv} - 0.63), \tag{4.8}$$

where all error estimates are again from the fit of the linear regression line.

For the RAMS implementation of this scheme, nearly every calculation was handled as the wet adiabat scheme. Again, the values of θ^* and T^* (and now ϵ) were determined from the middle level of the boundary layer depth. The value for α was determined as the slope of a least-squares line through the (r^*, T^*) points through the boundary layer depth. The model level just below the inversion was determined as before.

4.3 As a function of sub-grid variability

All of the previous FC schemes parameterize the cloud fraction based on information at a grid-point (or a grid-line) that is used to represent information over the entire grid-volume (or grid-column). However, many influences on cloud formation can be found on scales which are smaller than a mesoscale model's grid spacing. These influences include variations on heat and moisture variances and co-variances. By running the RAMS model with Weissbluth's parameterization, information on these subgrid-scale variances and co-variances can be saved. The following FC schemes need this information, and thus could not be run using RAMS without Weissbluth's small-scale turbulence parameterization.

4.3.1 Ek and Mahrt

Ek and Mahrt (1991) built a FC function out of relative humidity and its standard deviation, σ_{RH}. They constructed their FC scheme using spatially-averaged relative humidity and turbulent and subgrid mesoscale variations of relative humidity. Their function is:

$$FC = f\{[RH], \sigma_{RH}\}, \tag{4.9}$$

where the function is the percentage of the area under a Gaussian curve where $[RH]$ is greater than 1.0. $[RH]$ is the average relative humidity of the grid-volume (as before), and will hereafter be referred to as RH. The Gaussian distribution is determined from σ_{RH} and is comprised of both turbulent scale and mesoscale variations. A graphical depiction of this function and Gaussian distribution can be found in Figure 4.4.

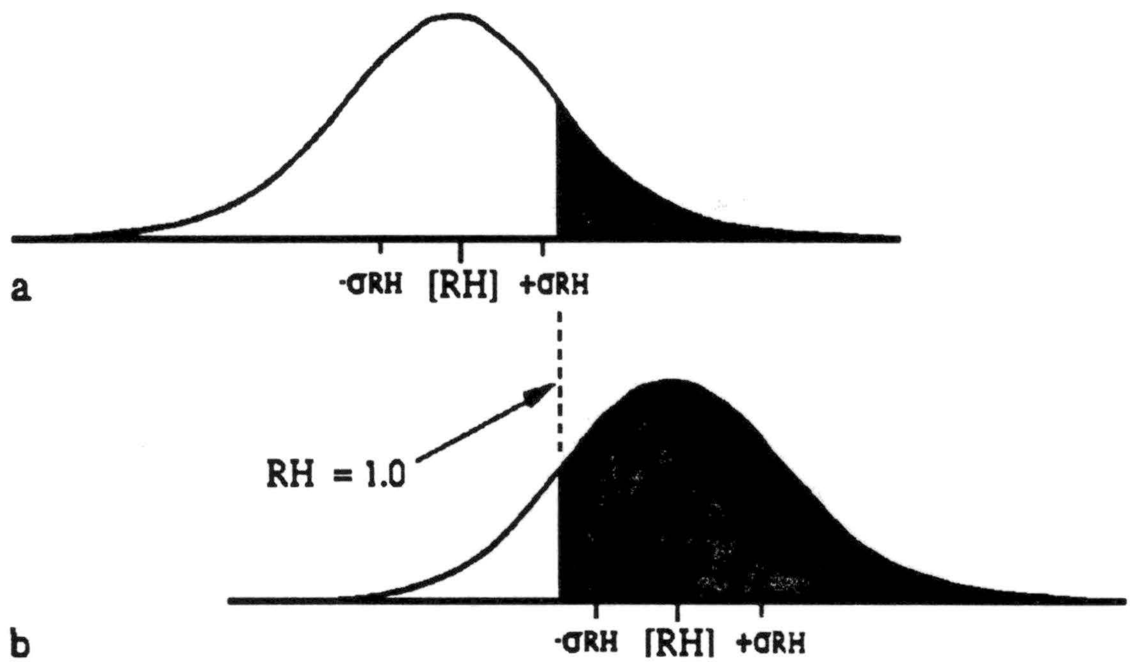

Figure 4.4: Depiction of cloud fraction (dark region) for a Gaussian distribution of relative humidity with (a) RH less than 1.0 and (b) RH greater than 1.0. (from Ek and Mahrt, 1991).

It can be helpful to examine Figure 4.4 and see how the magnitudes of RH and σ_{RH} can affect the FC. A larger value of RH would shift the distribution to the right and thus increase the area under the curve where RH is greater than 1.0. As would be expected, this larger value of RH would mean a higher FC. When the RH is less than 1.0, a larger value of σ_{RH} would also increase the darkened area under the curve. This increase can be reasoned in the following way. For a given value of RH, a subgrid-volume with a large σ_{RH} will more likely have "spots" where the local RH is so much bigger than the volume-averaged RH that these "spots" will allow cloud formation. Thus, the larger the grid-volume or the larger the turbulent variability of RH, the greater the chances that the volume contains at least some cloud.

Ek and Mahrt assumed that the turbulent and mesoscale fluctuations of RH are independent of each other. Therefore, σ_{RH} was written as:

$$\sigma_{RH} = \left[\sigma^2_{RHturb} + \sigma^2_{RHmeso}\right]^{1/2}, \tag{4.10}$$

where σ^2_{RHturb} is the turbulent variance and σ^2_{RHmeso} is the mesoscale variance.

To determine the contribution of σ^2_{RHturb} to the standard deviation on RH, Ek and Mahrt used data from 18 upper-level flight legs from the Hydrological and Atmospheric Pilot Experiment (HAPEX) over southwest France in 1986. They wrote the σ^2_{RHturb} as a function of the moisture variance ($\overline{w'q'_t}$), standard deviation of vertical velocity (σ_w), and saturation mixing ratio ($\overline{q_s}$). The authors claim that this formulation can be useful because boundary layer models (such as RAMS using Weissbluth's scheme) can determine these variables. After performing a linear regression on the HAPEX data, Ek and Mahrt found that:

$$\sigma^2_{RHturb} = C1 + C2\left[\overline{w'q'_t}/(\sigma_w \overline{q_s})\right]^2, \tag{4.11}$$

where $C1 = 0.00014$ and $C2 = 9.75$.

When considering the mesoscale contribution, Ek and Mahrt concluded that σ^2_{RHmeso} should increase with increasing grid size because more mesoscale variations of RH would become subgrid. They computed 5-km averages of RH for the 18 upper-level flight legs from HAPEX and then determine the ensemble average of σ^2_{RHmeso} over 10-, 25-, 50-, and 100-km areas. From plotting σ^2_{RHmeso} as a function of horizontal scale, Ek and Mahrt perform a least-square fit to a logarithmic function and find:

$$\sigma^2_{RHmeso} = a_0 + a_1(\Delta x) + a_2 \ln(\Delta x), \tag{4.12}$$

where Δx is the horizontal grid spacing in kilometers and must be $\geq$ 5 km; and where $a_0 = -0.03$, $a_1 = -0.00015$ km^{-1}, and $a_2 = 0.02$. For the finest grid used in this study (with horizontal spacing of 5 km), the mesoscale contribution to the relative humidity variance was set to zero.

In the RAMS configuration, the RAMS model determined FC from area under the Gaussian curve greater than RH = 0.9 rather than RH = 1.0 as before. This change from the original Ek and Mahrt FC scheme was done because RAMS is not able to produce relative humidities greater than 1.0. The greatest value of FC diagnosed was then only 0.5. Moving the cutoff of the area under the curve down to RH = 0.9 allowed for more realistic values of FC to be diagnosed in areas where the RH was close to 1.0. Changing the cutoff within the distribution, however, had an adverse effect of increasing the FC predicted in areas of relatively lower RH.

It should also be mentioned for the RAMS implementation of this scheme, the perturbation of mixing ratio, not specific humidity, was used. More will be mentioned on the change from $\overline{w'q_t'}$ to $\overline{w'r_t'}$ later in this chapter.

4.3.2 Manton and Cotton

Some of the first work done in subgrid-scale condensation modeling was done by Manton and Cotton (1977). They developed a set of model equations to describe the behavior of a moist atmosphere. These equations also included a description of fractional cloudiness. The fractional cloudiness was used to determine the grid-volume's cloud liquid water density, ρ_c. To determine the moments of ρ_c, Manton and Cotton assume a Gaussian distribution of $(\rho_t - \rho_r - \rho_s)$ with variance:

$$\sigma_c^2 = \overline{(\rho_t' - \rho_r' - \rho_s')^2}, \tag{4.13}$$

where ρ_t represents total water density, ρ_r represents rain water density, ρ_s represents saturation density, and the primes denote a random fluctuation about the mean.

Using the standard deviation of the cloud liquid water density, σ_c, to diagnose FC, Manton and Cotton arrive at:

$$FC = \frac{1}{2}\left[1 + \mathrm{erf}\left(\frac{\rho_t - \rho_r - \rho_s}{\sqrt{2}\sigma_c}\right)\right], \tag{4.14}$$

where erf is the error function.

In this RAMS configuration, information on ρ_s' was not readily available. Therefore, the standard deviation could not be diagnosed. However, another equation for σ_c was used from Chen (1984). Neglecting terms that contain random fluctuations of rain water mixing ratio, the standard deviation becomes:

$$\sigma_c = \left[a_2^2\left(\overline{r_t'^2} - 2\alpha_2\overline{r_t'\theta_{il}'} + \alpha_2^2\overline{\theta_{il}'^2}\right)\right]^{\frac{1}{2}}, \tag{4.15}$$

where the variances and co-variances needed for this scheme are the same that RAMS saves in the analysis files. The coefficients are equal to:

$$a_2 = \left[1 + \frac{Lr_s}{c_pT}\left(\frac{L}{R_vT} - 1\right)\right]^{-1} \tag{4.16}$$

$$\alpha_2 = \frac{r_s\left[\frac{L}{R_vT} - 1\right]}{\theta_{il}}. \tag{4.17}$$

For the RAMS implementation of the subgrid-scale schemes, information on $\overline{r_t'^2}$, $\overline{\theta_{il}'^2}$, and $\overline{\theta_{il}'r_t'}$ is obtained from the Weissbluth small-scale turbulence parameterization. These variables are diagnosed with help of the vertical velocity variance predicted from Weissbluth's scheme. They are saved in the model's analysis files along with the other standard variables previously mentioned that are saved to the RAMS analysis files.

4.3.3 Sommeria and Deardorff

Sommeria and Deardorff (1977) developed a subgrid-scale condensation scheme very similar to Manton and Cotton's (1977) scheme, with the exception that it is assumed that the quasi-conservative variables θ_l and q_w have a joint normal probability distribution. It then follows that:

$$FC = \int_{-\infty}^{\infty}\int_{q_{sl}}^{\infty} G\,dq_w d\theta_l, \tag{4.18}$$

where G is the bivariate normal function. For their study, G is given by:

$$G = \left[2\pi\sigma_{\theta_l}\sigma_{q_w}(1-r^2)^{\frac{1}{2}}\right]^{-1}\exp\left\{\frac{-1}{2(1-r^2)}\left[\frac{\theta_l'^2}{\sigma_{\theta_l}^2} - \frac{2r\theta_l'q_w'}{\sigma_{\theta_l}\sigma_{q_w}} + \frac{q_w'^2}{\sigma_{q_w}^2}\right]\right\}, \tag{4.19}$$

where:

$$r = \frac{\overline{q'_w \theta'_l}}{\sigma_{q_w} \sigma_{\theta_l}}, \tag{4.20}$$

and:

$$\sigma^2_{\theta_l} = \overline{\theta'^2_l} \qquad \text{and} \qquad \sigma^2_{q_w} = \overline{q'^2_w} \ . \tag{4.21}$$

After assuming a linear approximation for q_{sl} around the value $q_{sl} = q_s(\theta_l, p)$ and generalizing σ_{q_w}, Sommeria and Deardorff arrive at an approximation for Equation 4.18, which is given by:

$$FC = \frac{1}{2}\left[1 + \mathrm{erf}\left(\frac{Q_1}{\sqrt{2}}\right)\right], \tag{4.22}$$

where $Q_1 = (q_w - q_{sl})/\sigma_1$ is a normalized departure from mean saturation and σ_1 is the standard deviation of $(q_w - q_{sl})$. This scheme differs from Manton and Cotton's (1977) scheme in that Sommeria and Deardorff assume a Gaussian distribution for $(q_w - q_{sl})$, while Manton and Cotton assume a Gaussian distribution for $(r_w - r_s)$. Sommeria and Deardorff claim their method is preferable because r_s is not conserved during condensation. Banta (1979), however, showed that it is more difficult to satisfy the bi-variant normal approach of Sommeria and Deardorff than the simpler normal distribution of Manton and Cotton. The standard deviation, σ_1, is equal to:

$$\sigma_1 = (\sigma^2_{q_w} + \alpha^2_1 \sigma^2_{\theta_l} - 2r\alpha_1 \sigma_{q_w} \sigma_{\theta_l})^{\frac{1}{2}}, \tag{4.23}$$

where:

$$\alpha_1 = 0.622 \left(\frac{p}{p_0}\right)^{0.286} \frac{Lq_{sl}}{R_d T^2_l}, \tag{4.24}$$

where $T_l = \frac{T}{\theta \theta_l}$, $q_{sl} = q_s(T_l)$, q_s is the saturation specific humidity, and $p_0 = 1013.25$ mb. Substituting Eqns. 4.20 and 4.21 into Equation 4.23 results in:

$$\sigma_1 = (\overline{q'^2_w} + \alpha^2_1 \overline{\theta'^2_l} - 2\alpha_1 \overline{q'_w \theta'_l})^{\frac{1}{2}}. \tag{4.25}$$

Two differences between the subgrid-scale variances and co-variances saved in the RAMS analysis files and those used in this FC scheme should be mentioned. One of RAMS' predictive variables is θ_{il}, the ice-liquid potential temperature. Weissbluth's parameterization diagnoses the perturbation of this variable, not the perturbation of θ_l, which is needed for this FC scheme. However, for the RAMS implementation of this scheme, θ_{il} and θ_l are considered to be equivalent. This assumption is valid in areas where no ice is present. Nearly all boundary-layer clouds occur below the freezing level. Because the focus of this study is boundary layer fractional cloudiness, there is typically no ice in the area of concern. It is similarly assumed that the perturbation of both variables are equivalent.

The other difference is that RAMS predicts on r_t, the total mixing ratio, while this FC scheme uses q_w, the total specific humidity. Mixing ratio and specific humidity are approximately equal to each other in the lower troposphere and are often used interchangeably. For purposes of this study, however, the correct variable was always used. Unfortunately, it was not possible to always use the perturbation of the correct variable. Weissbluth's scheme saves the perturbation of r_t (the total mixing ratio), not the perturbation of q_w (the total specific humidity). One can reason that these perturbations are even more similar than the variables themselves because the perturbations of the variables are generally smaller than their means. Therefore, when diagnosing FC within the subgrid-scale schemes, RAMS substitutes the perturbation of r_t everywhere the perturbation of q_w appears.

4.3.4 Bechtold, Fravalo, and Pinty

Bechtold, Fravalo, and Pinty (1992) developed a model, which included a partial cloudiness scheme, that was used for mesoscale marine boundary layer applications. This model gives a statistical description of the subgrid-scale condensation. It is assumed that the turbulent fluctuations of θ_l (liquid-water potential temperature) and q_w (total water specific humidity) have a joint normal probability distribution. Mellor (1977) showed that to reduce the integration from over two variables to over one, an intermediate variable can be used. The variable he introduced is $s = a/2(q'_w - \alpha_1 \theta'_l)$. The coefficients for s are also defined by Mellor (1977) and Bougeault (1981). They are defined as:

$$a = \left(1 + \frac{L}{R_v T_l}\frac{L}{c_p T_l} q_{sl}\right)^{-1} \tag{4.26}$$

$$\alpha_1 = q_{sl}\left(\frac{L}{R_v T_l^2}\right)\frac{T}{\theta}, \tag{4.27}$$

with q_{sl} and T_l given as before.

For a normalized variable, denoted by $\zeta = s/\sigma_s$, having a probability density function $G(\zeta)$, the fractional cloudiness will be given by:

$$FC = \int_{-Q_1}^{+\infty} G(\zeta)d\zeta, \tag{4.28}$$

where $Q_1 = a(q_w - q_{sl})/2\sigma_s$. In this scheme, σ_s is equal to:

$$\sigma_s = \frac{a}{2}\left(\overline{q_w'^2} + \alpha_1^2\overline{\theta_l'^2} - 2\alpha_1\overline{\theta_l' q_w'}\right)^{1/2}. \tag{4.29}$$

All of the information needed to evaluate the FC for this scheme has been described - ($\overline{q_w'^2}$, $\overline{\theta_l'^2}$, $\overline{\theta_l' q_w'}$, a, α_1) - which leads to σ_s and Q_1. It should be kept in mind that the variances and co-variances in Equation 4.29 are different than those saved in the RAMS analysis files. These differences have been resolved in the previous section. The probability density function, $G(\zeta)$, must still be evaluated. Bechtold, Fravalo, and Pinty chose to identify $G(\zeta)$ as a Gaussian function, where $G(\zeta) = (2\pi)^{-1/2}\exp^{-\zeta^2/2}$. For RAMS, $G(\zeta)$ was evaluated the same way, which leads to:

$$FC = \frac{1}{2}\left[1 + \mathrm{erf}\left(\frac{Q_1}{\sqrt{2}}\right)\right], \tag{4.30}$$

where erf is the error function.

4.4 Uncertainties in evaluation

All of the above fractional cloudiness schemes are diagnosed from other model variables. These parameterizations are therefore only as good as the inputs to the parameterization. If the model produces a poor forecast, the fractional cloudiness diagnosed will also poorly represent observations. This section will mention uncertainties within the model and how these uncertainties could affect the fractional cloudiness schemes and thus their evaluation.

One of the biggest uncertainties with a mesoscale model in evaluating fractional cloudiness is in the distribution of moisture. All of the schemes programmed into RAMS depend on moisture variables, in one way or another. Should the model not accurately portray how this moisture is distributed, every FC scheme will be adversely affected. It is possible that the model could identify a strong moisture gradient only a grid point or two away from where it is observed. A small error in the placement of this gradient will not allow the most accurate depiction of fractional cloudiness, and will lower the confidence with which the FC can be evaluated against observations.

Another uncertainty with the model is how cloud layers affect the radiative calculations. Currently, the RAMS radiation packages are not dependent on the cloud fraction within a grid-volume. Uncertainties in the radiation can create additional uncertainties in surface fluxes and surface temperature.

Some of the FC schemes programmed use boundary-layer variances and co-variances as determined from the Weissbluth parameterization. Uncertainties in these fluxes, which are dependent on the Level 2.5w small-scale turbulent parameterization, may cause incorrect inputs to the fractional cloudiness schemes.

For the FIRE I investigation, the subsidence as calculated by the model may create uncertainties in the strength and height of the boundary-layer inversion. Changes in subsidence strength can cause the boundary-layer to grow or shrink against what has been observed, and thus move the location of clouds diagnosed by the FC schemes. The surface temperature and fluxes are more certain over the ocean due to the slow temporal evolution and small variations in sea surface temperatures.

For the BLX83 investigation, uncertainties in surface fluxes and temperature can play a large role in where clouds are diagnosed by the fractional cloudiness schemes. Variations in soil moisture, vegetation type, vegetation parameterization, and albedo force these uncertainties. Also, the cloud feedback in surface heating, as mentioned before, can make an assessment of the FC schemes much more difficult.

Chapter 5

7 JULY 1987

The First ISCCP (International Satellite Cloud Climatology Project) Regional Experiment (FIRE) took place off the coast of California during the summer of 1987. The objective of the experiment was to provide researchers with a detailed multi-platform data set on the extensive fields of stratocumulus clouds that often form in the subtropics. Special attention was paid to the measurement of the formation, maintenance, and dissipation of these marine stratocumulus clouds.

The dates of the experiment were 29 June to 19 July 1987. Ground-based remote sensing equipment was located on San Nicholas Island (SNI) and operated throughout the duration of the experiment. Detailed satellite imagery was taken during FIRE as well as in situ measurements from multiple aircraft. Tethered balloons provided turbulence, cloud microphysical, and cloud radiative data. For more information on the FIRE, the reader is referred to Albrecht et al. (1988).

Excellent conditions for the experiment existed during the time period. The subtropical high was strongly evident during most of the experiment, providing extended periods of stratocumulus cloudiness in the target area. The case day chosen for this study, 7 July 1987, was chosen because on this day, a long-lived stratocumulus deck began to dissipate, from west to east.

5.1 Observed Conditions

On this day, a subtropical high pressure system was located over the eastern Pacific Ocean, with a ridge that extended into the southern California area. At the same time, a thermal low had developed over Arizona, which created a strong pressure gradient across the FIRE area. Strong north to northwesterly winds from 10-15 m s^{-1} were observed over the FIRE region from the surface up to the 700 hPa level. The surface conditions in the area at 00 UTC on 7 July (which were used to initialize the model simulation) are shown in Figures 5.1 and 5.2.

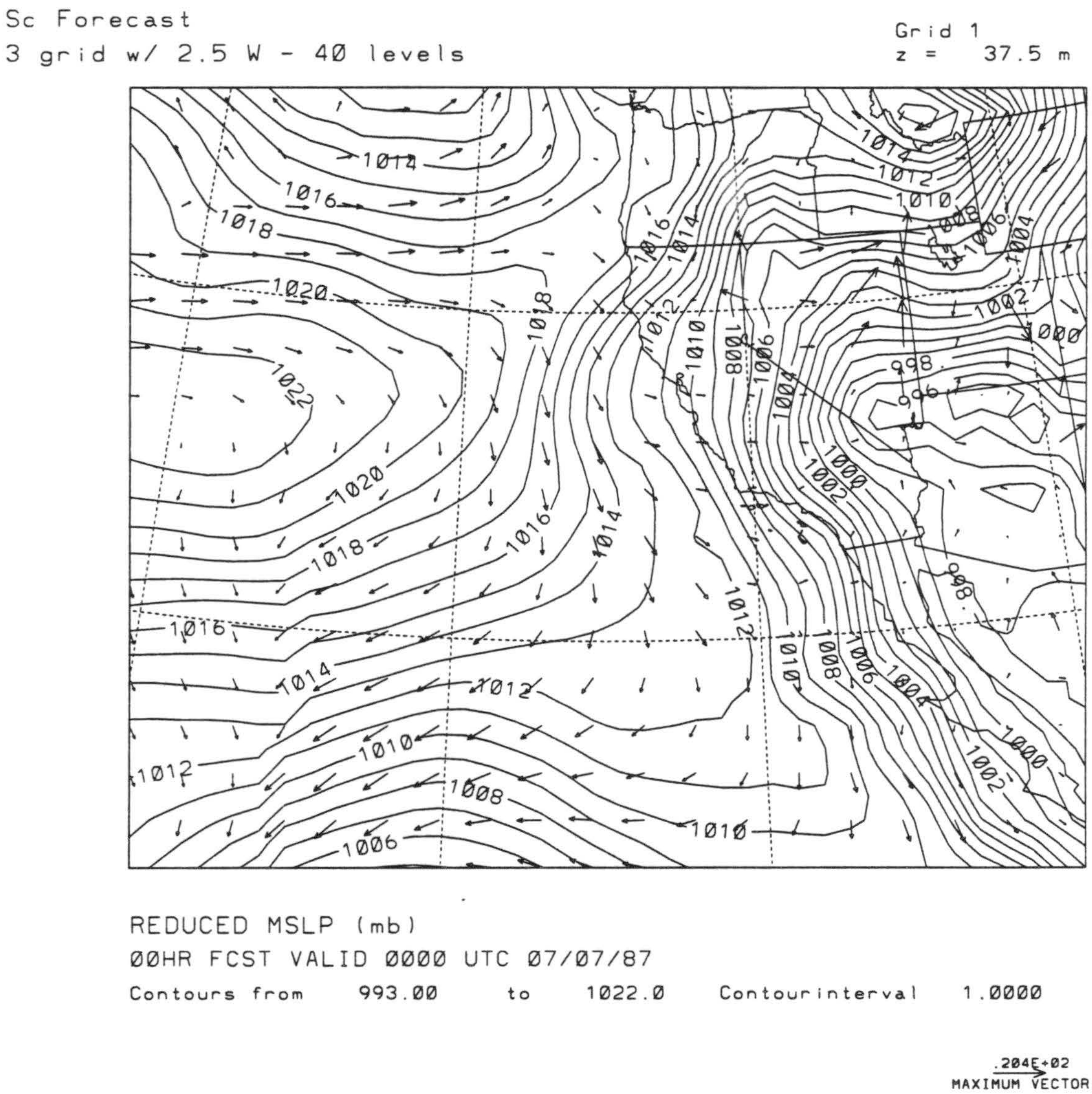

Figure 5.1: RAMS depiction of synoptic-scale initial mean sea level pressure and winds for Grid 1 at 00 UTC 7 July.

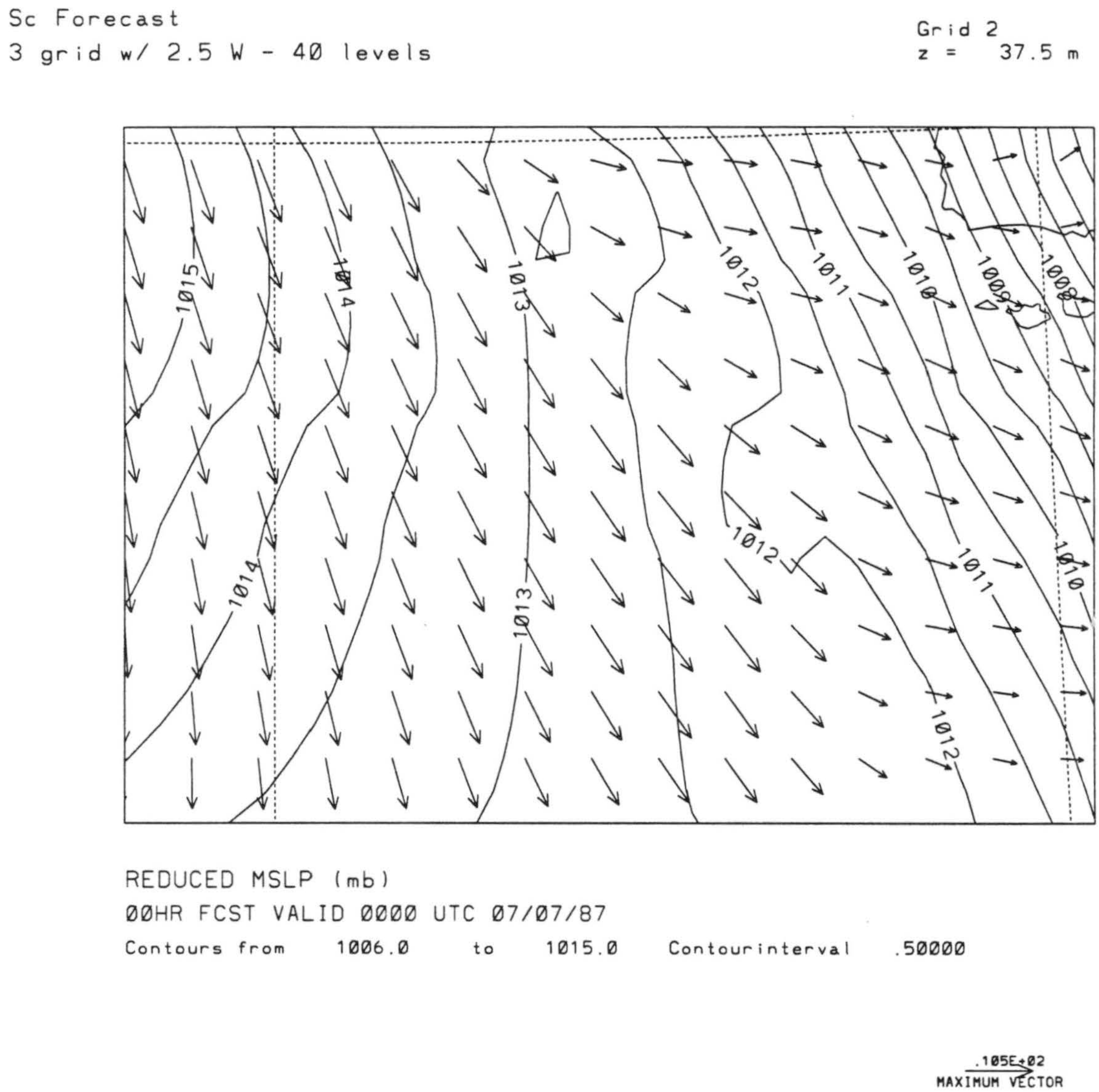

Figure 5.2: RAMS depiction of mesoscale initial mean sea level pressure and winds for Grid 2 at 00 UTC 7 July.

At 700 hPa, the circulation pattern associated with subtropical high is still evident. There is strong flow to the north of the high, bringing strong westerly winds into Washington state. Figure 5.3 shows the initial 700 hPa geopotential heights and winds.

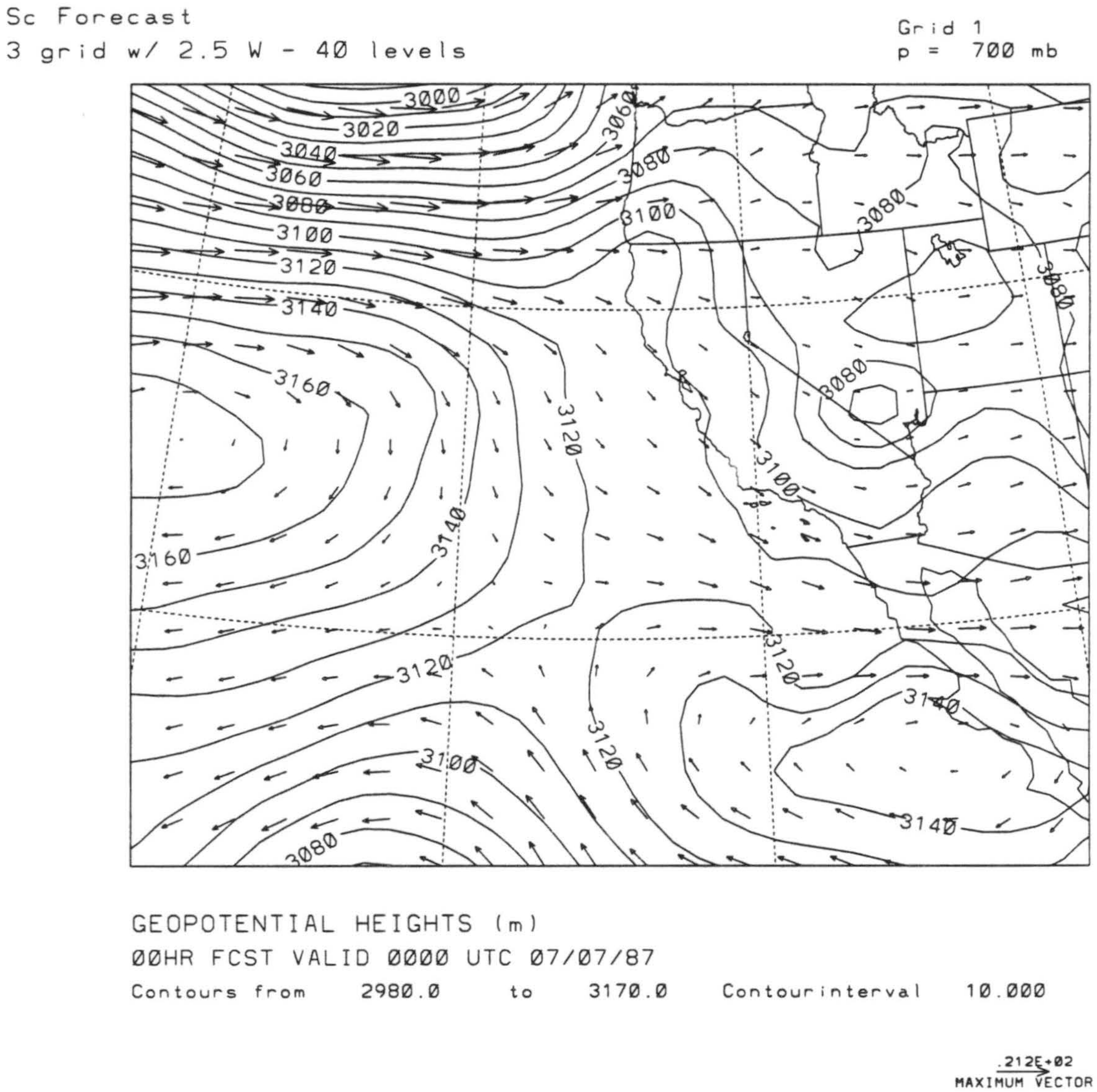

Figure 5.3: RAMS depiction of synoptic-scale initial 700 hPa geopotential heights and winds for Grid 1 at 00 UTC 7 July.

At 500 hPa, there is generally non-descript zonal flow. A weakening short wave is approaching the FIRE target area. Figure 5.4 shows the initial 500 hPa geopotential heights and winds.

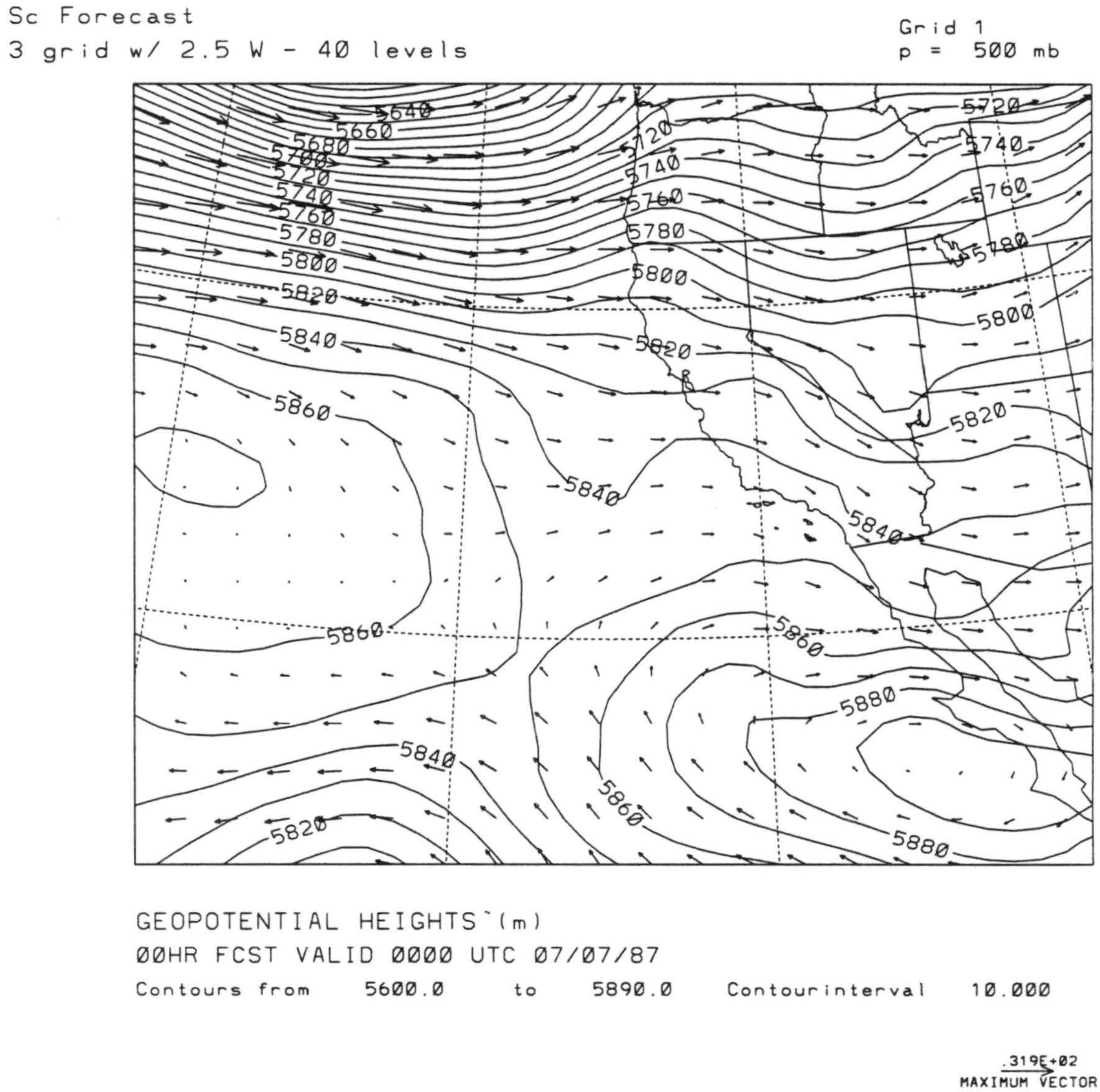

Figure 5.4: RAMS depiction of synoptic-scale initial 500 hPa geopotential heights and winds at 00 UTC 7 July.

At 250 hPa, there is again zonal flow, with the jet stretching across the top of the grid domain near 50° N. Figure 5.5 shows the initial 250 hPa geopotential heights and winds.

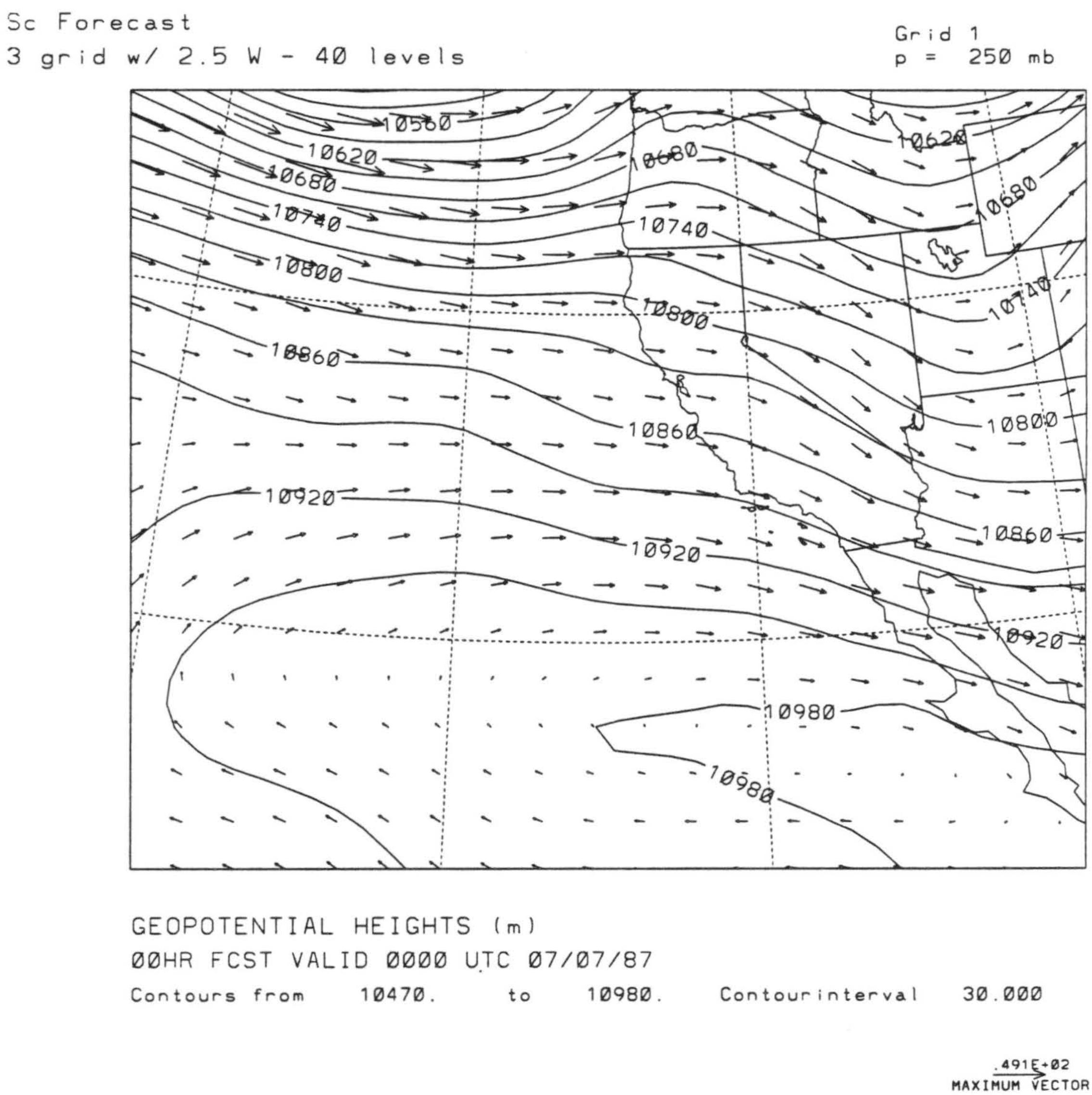

Figure 5.5: RAMS depiction of synoptic-scale initial 250 hPa geopotential heights and winds at 00 UTC 7 July.

The start of the model simulation, 0000 UTC, corresponds to 4:00 p.m. local time. During the night, strong long wave cooling caused a strengthening of the inversion and stratocumulus cloud deck. After sunrise and during the day, the cloud deck was observed to begin to dissipate on its western edge. As the day progressed, the area where the clouds had broken up moved further and further east. By 1830 UTC, a strong cloud transition was captured on satellite with the LANDSAT Thematic Mapper (2.08 - 2.35 μm band). This transition can easily be seen in Figure 5.6. West of the transition clear conditions were observed. At the transition, scattered cumuli were observed, becoming broken stratocumulus further to the east. East of the transition, nearly solid stratocumulus was found.

In the LANDSAT image, there appears to be an abrupt shift in the north-south orientation of the transition line. This shift can be seen about 1/3 of the way down from the top of the image. This "kink" may be as a result of circulations induced from the land-sea interaction. The northern part of the finest grid is closer to the California coast than the southern part.

The cloudiness transition was accompanied by changes in measured temperature, moisture, and inversion height. Data collected from the NCAR Electra around this time showed that the sea surface temperature was around 17°C in the clear region, dropping to around 15.5°C under the solid stratocumulus. The Electra also measured warmer and moister conditions in the boundary layer west of the transition. Differences across the transition of around 0.5 K in θ and 0.25 g kg^{-1} in q were found. Finally, it was found that the inversion height was lower in the clear and cumulus areas than in the stratocumulus areas (see Figures 2.3 and 2.4). For further information about the aircraft data, the reader is referred to Betts and Boers (1990).

5.2 Comparison to observed conditions

The synoptic conditions were well simulated by RAMS for this case study. The high pressure system was well represented; it did not evolve significantly during the time of the simulation. The mean sea level pressure (MSLP) field predicted by RAMS 24 hours after

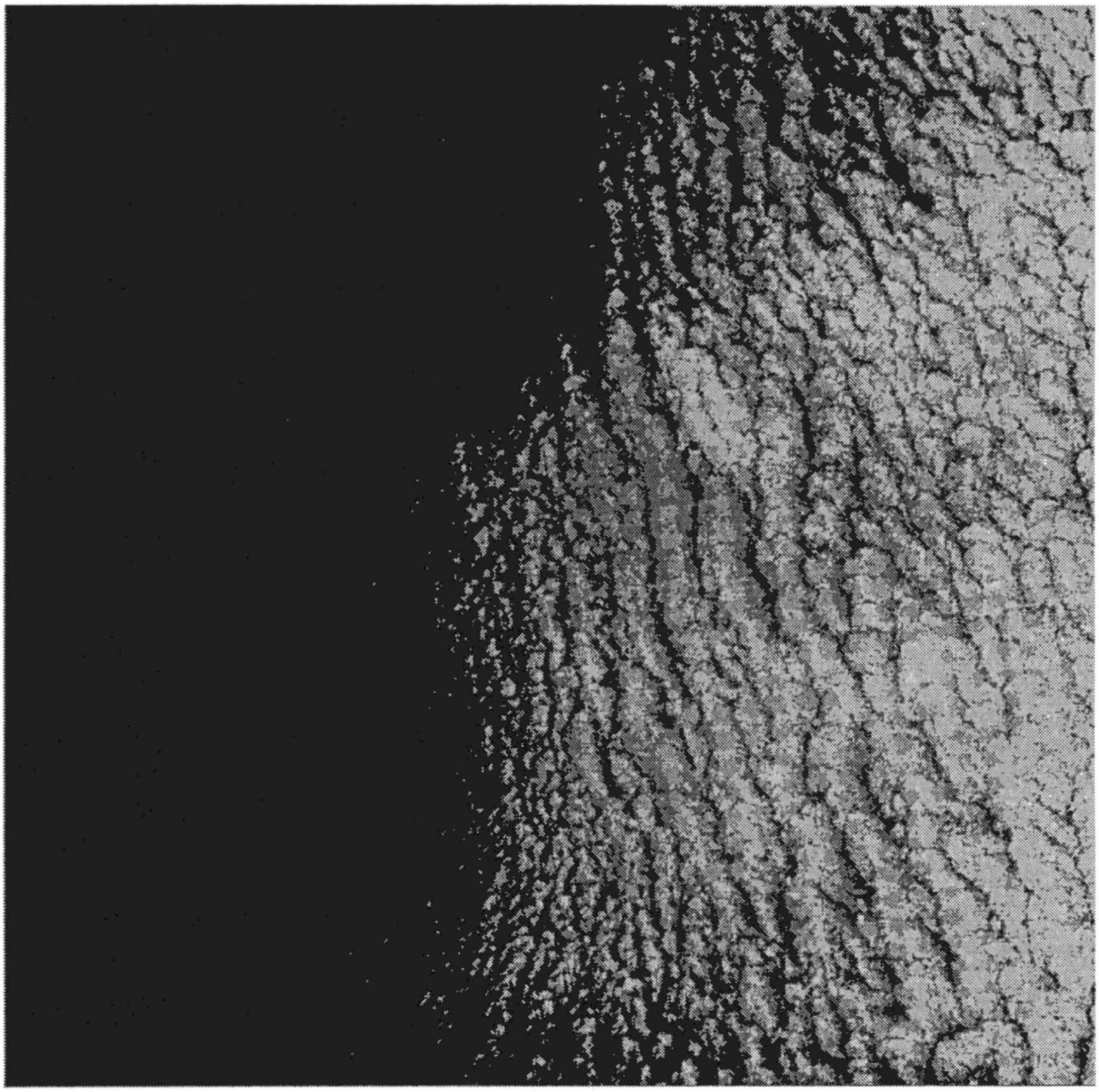

Figure 5.6: LANDSAT scene at 1830 UTC 7 July 1987 with center coordinates 33°10'N, 121°44'W. (from Betts and Boers, 1990). Distance across is about 180 km.

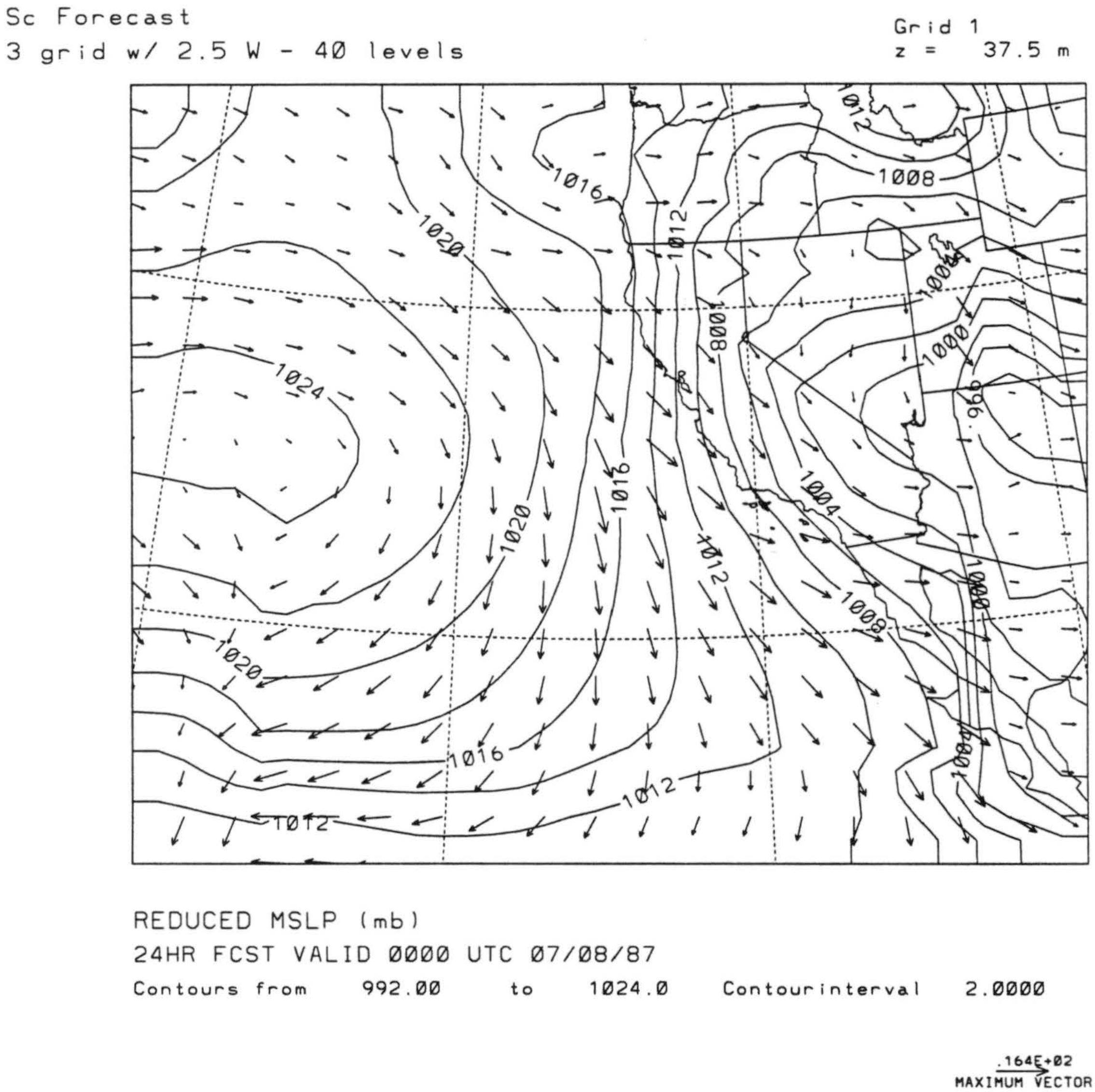

Figure 5.7: RAMS 24-hour prediction of mean sea level pressure and winds for Grid 1 valid at 00 UTC 8 July.

the start of the simulation is shown in Figure 5.7. Other comparisons with synoptic maps valid at other levels showed the simulation performance was reasonable and are not shown.

Taking a closer look at the predicted fields near the time the cloud transition was captured on satellite, shows the model performed well in developing a well-mixed boundary layer. Figures 5.8 and 5.9 show the potential temperature and total specific humidity fields in a cross-section through the center of the finest grid. The strong inversion is well-predicted as well as a very well-mixed layer. The magnitudes of the values are similar to those measured by the Electra.

One area the model did not perform well for the finest grid was the change in inversion height. The model did not show evidence of the boundary layer being much deeper on the east side of the grid; that is, where the stratocumulus was observed. The simulation of this case study predicted a boundary layer that was only slightly deeper moving east from the clear, through the scattered, to the cloudy areas.

There are four possible causes for the inability of RAMS to predict a strong sloping inversion height for this case study. The first reason is that a relatively course vertical grid spacing was used in this area. The vertical grid spacing of 75 m used within the boundary layer, while finer than most applications of RAMS, may not have been able to simulate the evolution of the inversion. At best, a 75 m spacing corresponds to a 300 m effective resolution, which is about the depth that the boundary layer changes from clear to solid cloud. The 75 m spacing was chosen to keep down the number of vertical levels to allow the cloud radiation scheme in RAMS to be used. The trade-off of this decision kept down the resolution of the model within the boundary layer.

A second reason for the flat inversion height is that the model-diagnosed fractional cloudiness did not influence the radiation calculations. This feedback was not possible for this case study using RAMS. The only way the radiation in the model is affected by water is if it is condensed out. However, an ideal fractional cloudiness scheme will produce cloud where it is observed, even if the grid-volume has not yet had condensation. It is possible that partial cloudiness in the radiation calculations would have changed the fields such that the boundary layer became significantly deeper under the cloudier areas.

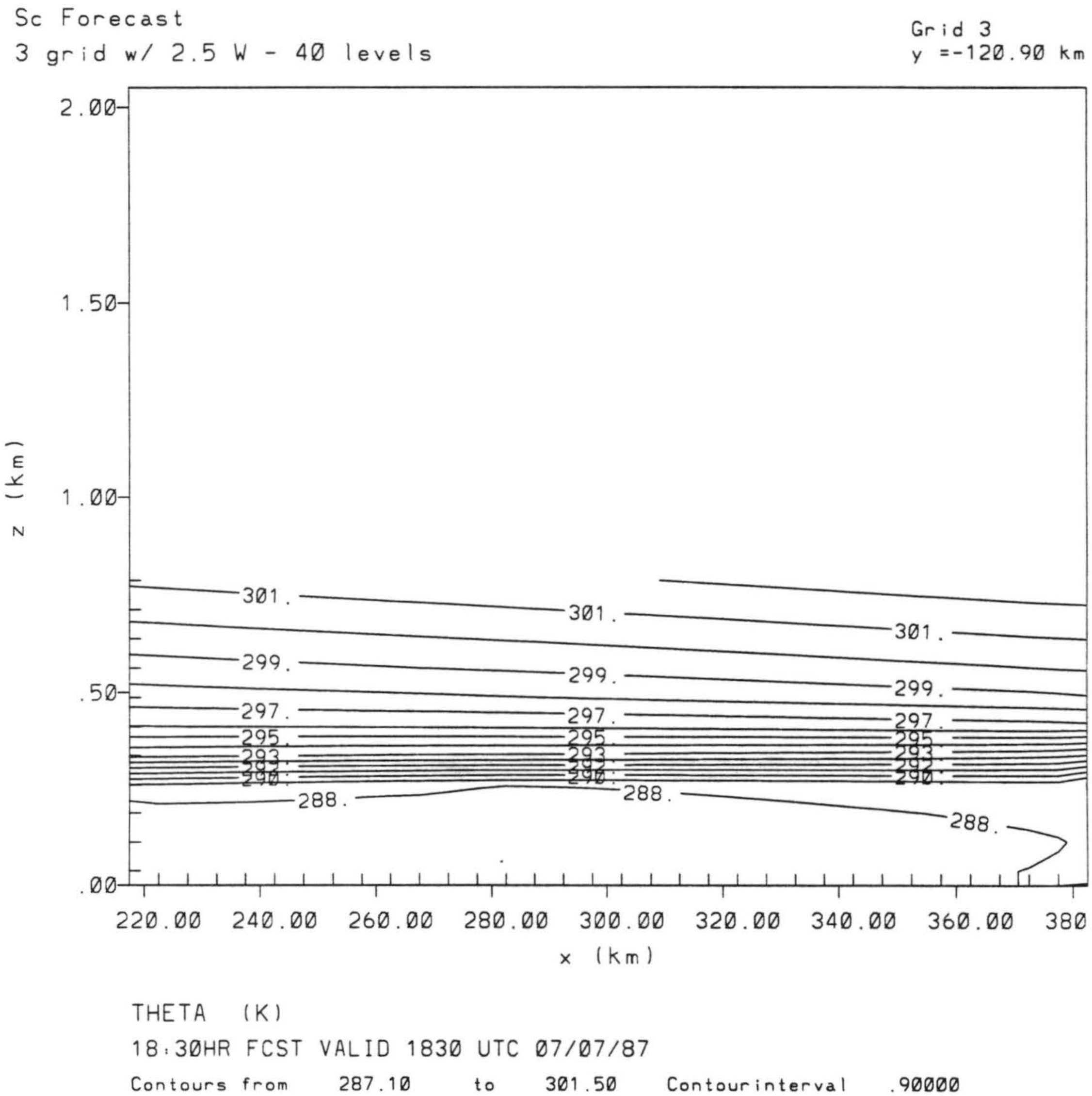

Figure 5.8: RAMS 18.5-hour prediction of potential temperature (K) for Grid 3 valid at 1830 UTC 7 July.

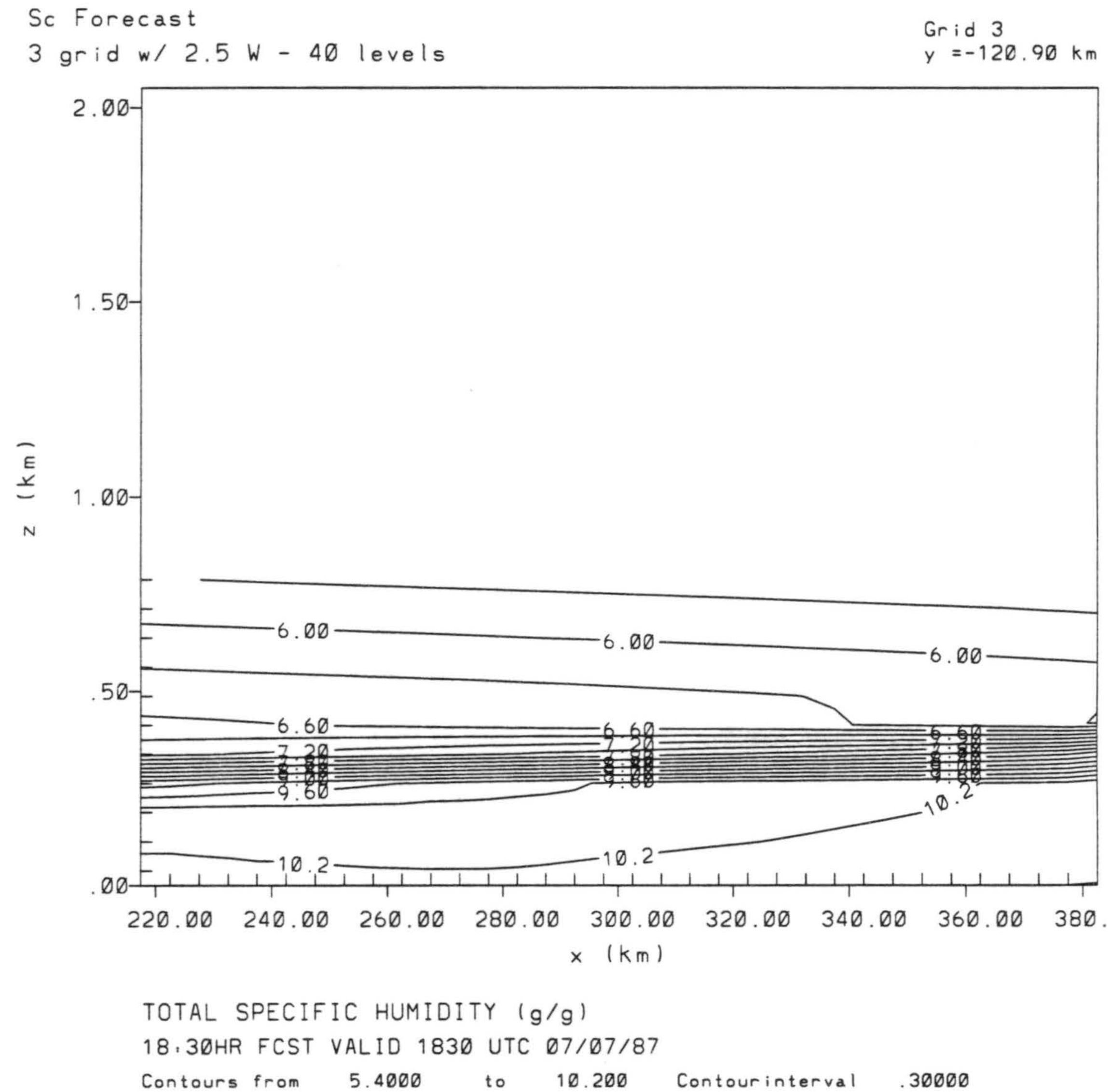

Figure 5.9: RAMS 18.5-hour prediction of total specific humidity (g/g) for Grid 3 valid at 1830 UTC 7 July.

A third reason for the flat inversion height could be uncertainties in the calculation of the subsidence over the target area. Finally, it is possible that the inversion was not as strong in the initial model fields as it was in observation.

RAMS soundings from the four cloud regimes as defined by Betts and Boers (1990) can be found in Figure 5.10. This figure shows four soundings as predicted by RAMS for the clear, cumulus, broken, and stratocumulus cloud regions. These soundings can be compared to the mean thermodynamic profiles observed by Betts and Boers which can be found in Figure 2.4.

The clear and cumulus profiles from RAMS show that the dewpoint line remains less than the temperature line, while these lines meet in the cloud deck in the broken and stratocumulus profiles. The inversion height, however, is not higher in the stratocumulus profile than in the clear profile, as was observed. Also, there is no moist layer near 900 hPa in the RAMS clear and cumulus soundings, as was observed. These differences could again be as a result of uncertainties such as model initialization and vertical resolution in the model.

5.3 Comparison to cloud transition

Attention will now be turned to the performance of the fractional cloudiness schemes that were put into the RAMS analysis package. The schemes will be evaluated against the LANDSAT satellite imagery and against fractional cloudiness measurements taken by aircraft.

5.3.1 Comparison to satellite imagery

The following plots show the fractional cloudiness (which is calculated independently in every grid-volume or grid-column) diagnosed by RAMS across an entire grid. All of the plots shown here will be for the finest grid, which allows the direct comparison of the performance of each scheme to observed conditions from the LANDSAT picture. Every one of these x-y plots is taken at the model level in RAMS just below the inversion, with the exception of the Betts and Boers FC schemes, which are valid throughout the depth of the boundary layer.

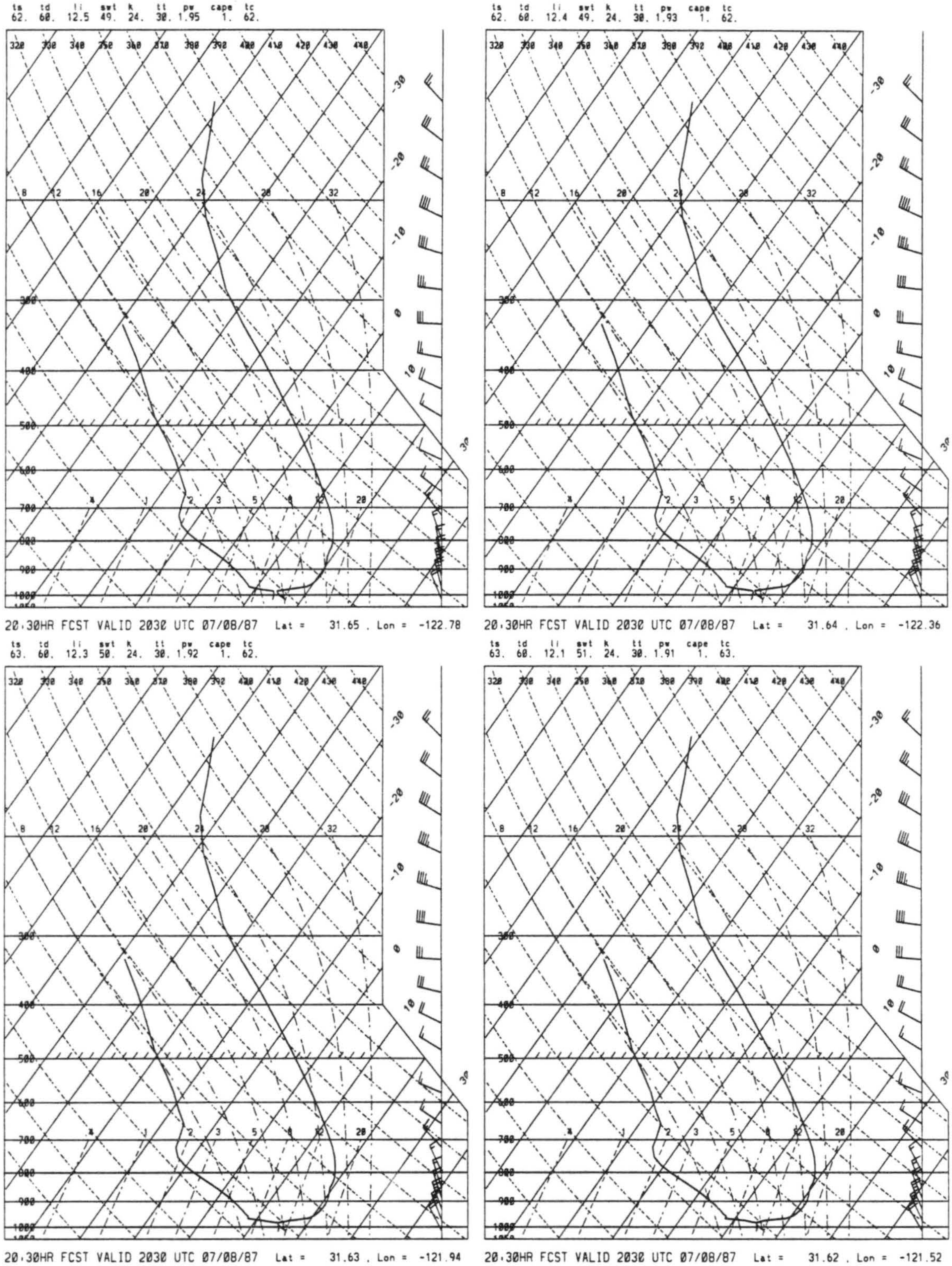

Figure 5.10: RAMS 20.5-hour prediction of soundings across transition valid at 2030 UTC 7 July. Upper left - Clear; Upper right - Cumulus; Lower left - Broken; Lower right - Stratocumulus.

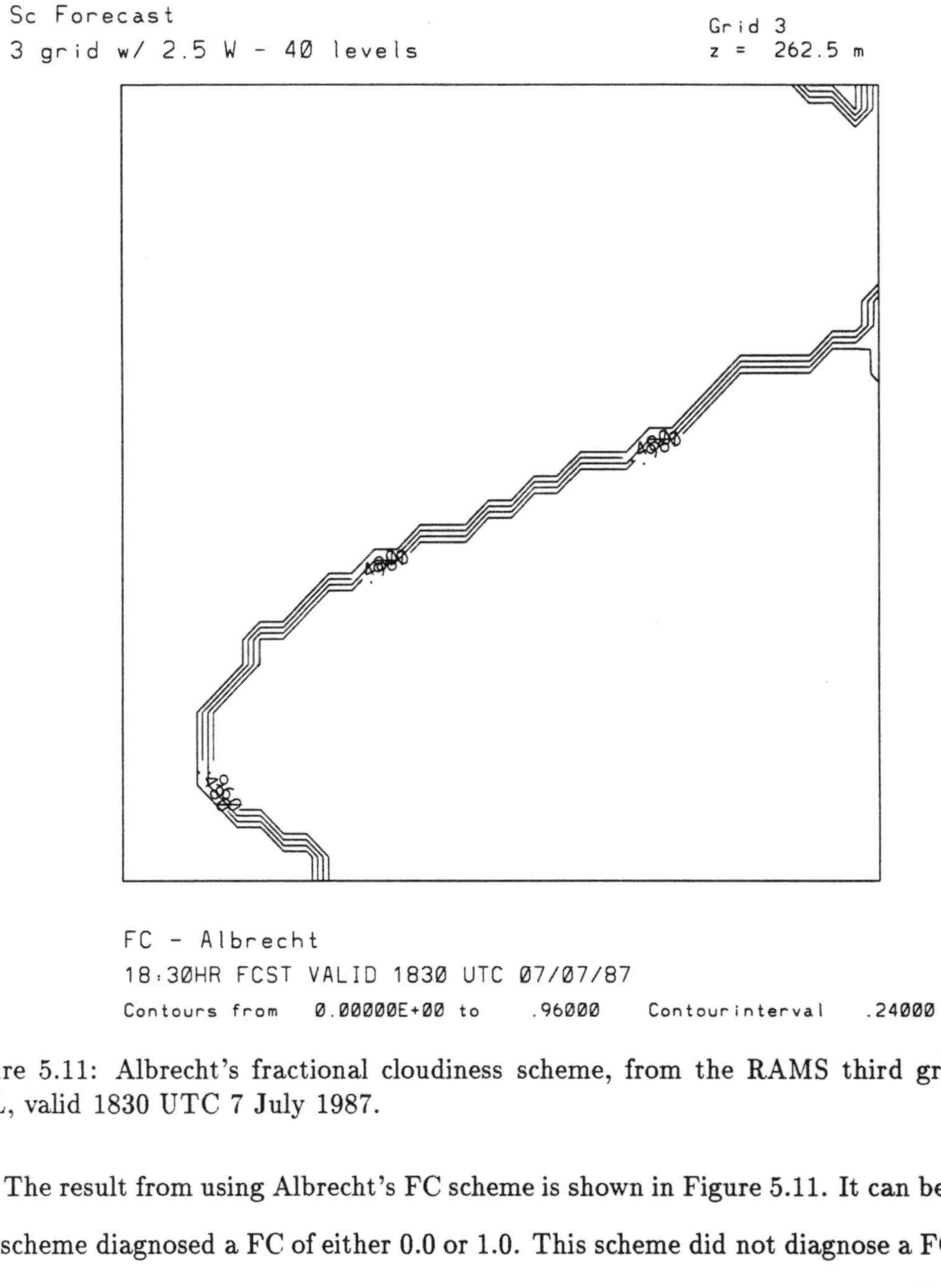

Figure 5.11: Albrecht's fractional cloudiness scheme, from the RAMS third grid, 262 m AGL, valid 1830 UTC 7 July 1987.

The result from using Albrecht's FC scheme is shown in Figure 5.11. It can be seen that this scheme diagnosed a FC of either 0.0 or 1.0. This scheme did not diagnose a FC between 0.0 and 1.0 in RAMS because the model diagnosed large areas of RH = 100%. In these areas, the FC from this scheme will always be 1.0. In other areas, where the RH did not reach 100%, the saturation ratio (SR) was too low to cause a range in the diagnosed values of fractional cloudiness. The SR was generally less than 1.0, which caused the numerator of this FC scheme to be less than zero. In these areas, no clouds were diagnosed.

The result from using Kvamstø's FC scheme is shown in Figure 5.12. This scheme performed remarkably better. A much smoother transition from clear to solid cloud was

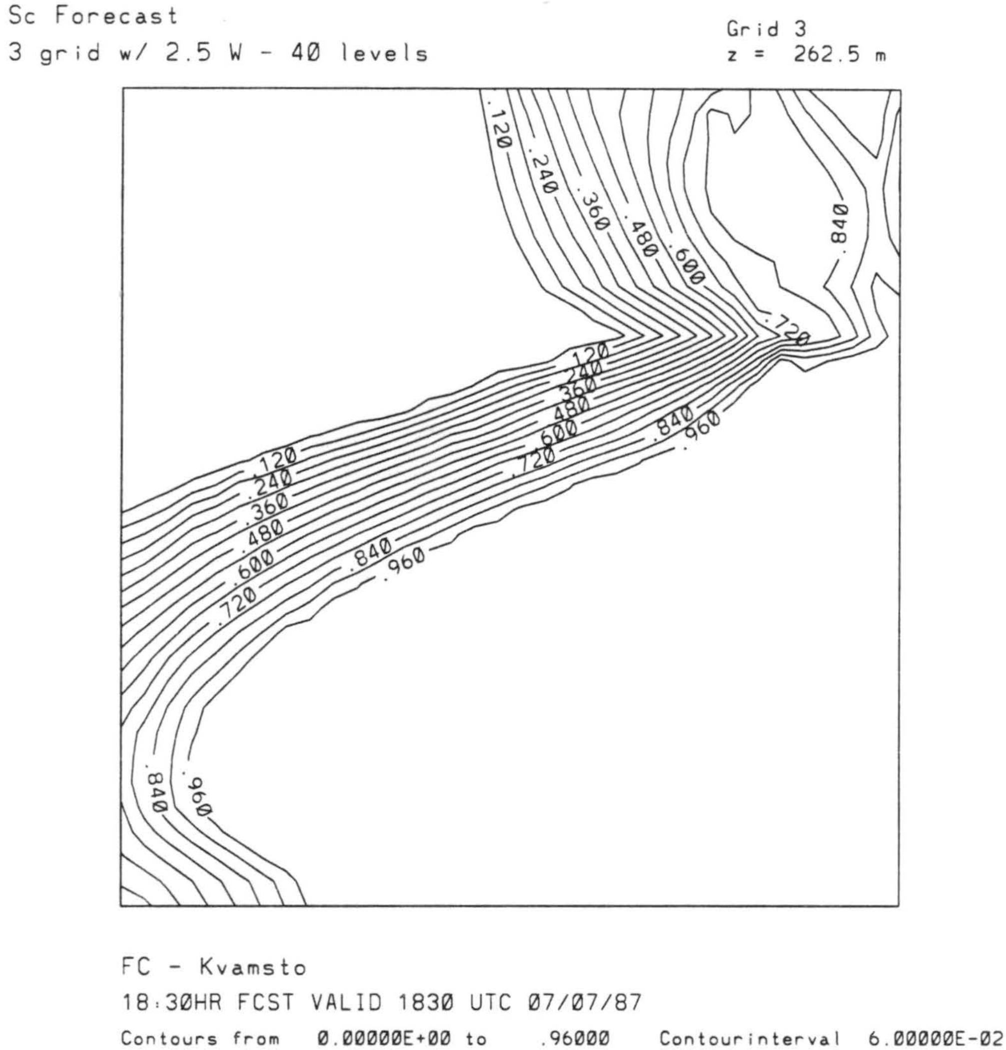

Figure 5.12: Kvamstø's fractional cloudiness scheme, from the RAMS third grid, 262 m AGL, valid 1830 UTC 7 July 1987.

diagnosed. The FC was a bit high in the southwest corner of the grid, and the transition line was not as north-south as observed. A probable cause for these deviations was the distribution of moisture within the model. The kink in the transition line about 1/3 of the way down from the top of the grid, however, was represented. The less solid cloud in the northeast corner of the grid was also well diagnosed.

The plot of the FC diagnosed by Sundqvist et al. scheme can be found in Figure 5.13. Many of the same features found in the Kvamstø plot were also found here. The kink in the transition line and the lower FC in the northeast corner of the grid appeared again. The

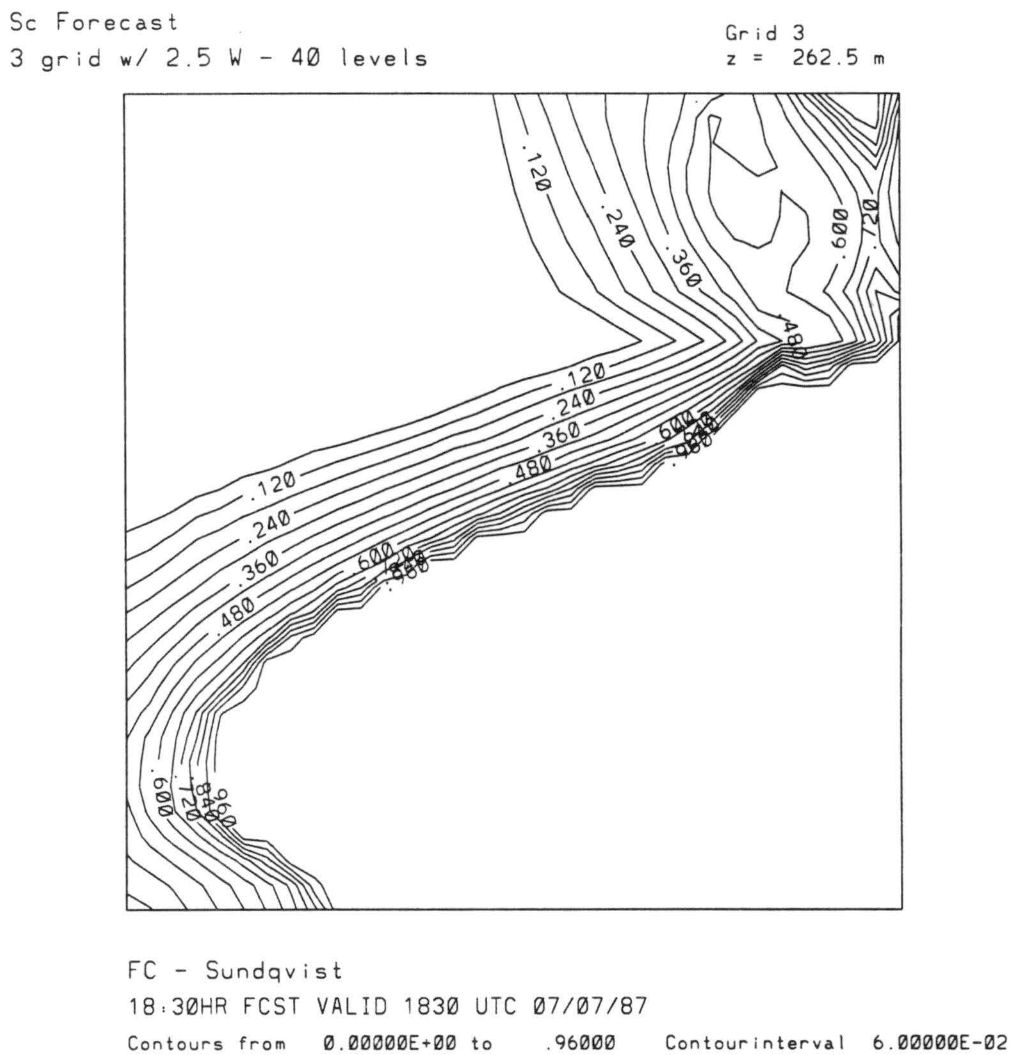

Figure 5.13: Sundqvist et al.'s fractional cloudiness scheme, from the RAMS third grid, 262 m AGL, valid 1830 UTC 7 July 1987.

transition, while again smooth, is not as linear as in the Kvamstø scheme. This difference is because the Sundqvist et al. FC scheme is not a linear function of RH.

The FC diagnosed by the Betts and Boers FC scheme, using the wet adiabat, is shown in Figure 5.14. This plot shows that nearly the entire grid diagnosed FC of 1.0. Remember that the Betts and Boers schemes diagnose a FC through the entire depth of the boundary layer, and are thus grid-column, not grid-volume, dependent. A possible cause for the failure of this scheme for this application is that the boundary layer was nearly equally well-mixed in all areas of the finest grid. With a mixed boundary layer in both clear and cloudy boundary layers predicted by the model, the mixing line slopes were found to be

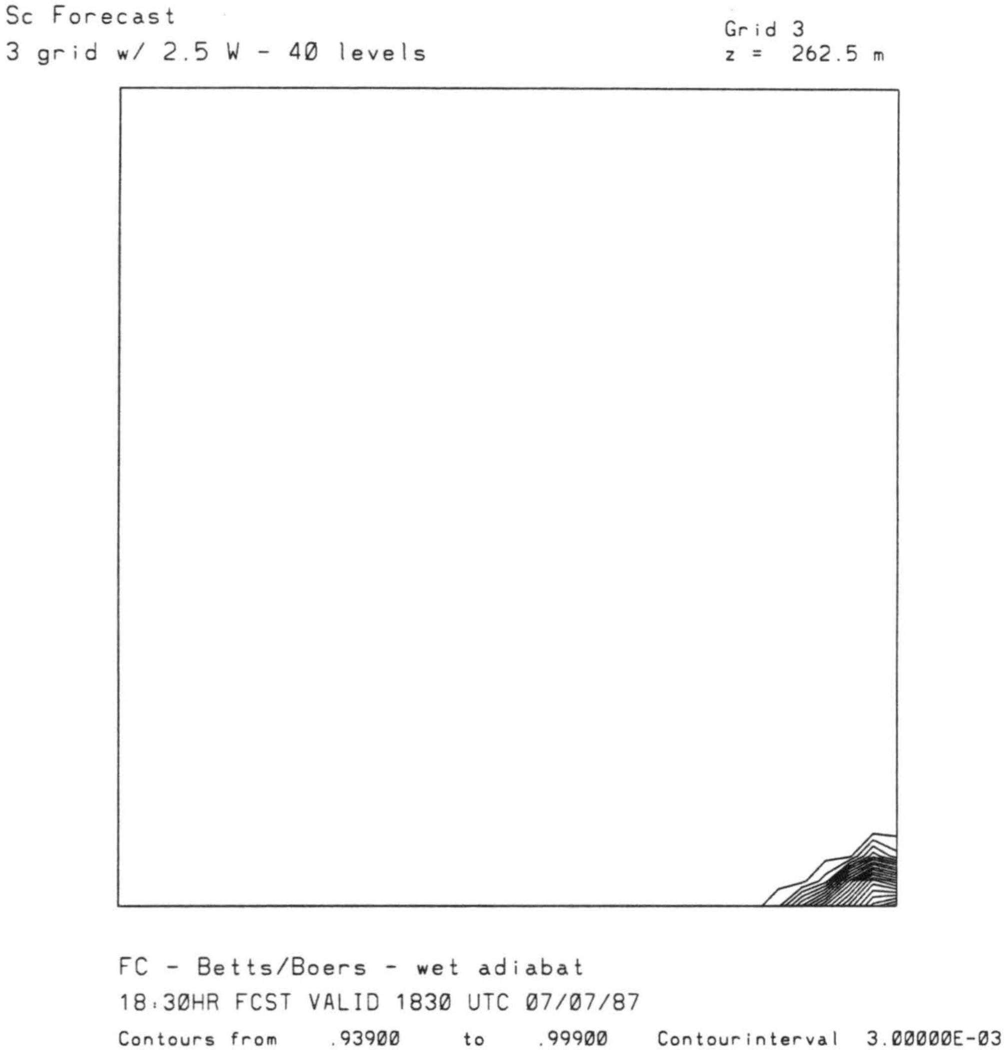

Figure 5.14: Betts and Boers' wet adiabat fractional cloudiness scheme, from the RAMS third grid, valid 1830 UTC 7 July 1987.

nearly equal. For this scheme, little to no change in the value of the slope would bring nearly identical FC everywhere in the grid. The similar slopes would likely be a problem in other models examining the transition, as uncertainties in model initialization probably contributed to the boundary layer being nearly equally well-mixed across the target area.

The result from using the FC scheme of Betts and Boers, using the wet virtual adiabat, is shown in Figure 5.15. The FC in this plot varied widely from 0.0 to 1.0, but in a haphazard manner compared to the observations. In the southeast corner of the grid, the FC was diagnosed to go to zero, but the satellite photo showed this area to be nearly solid cloud. The kink in the transition zone was diagnosed by this scheme, and the area to the north of

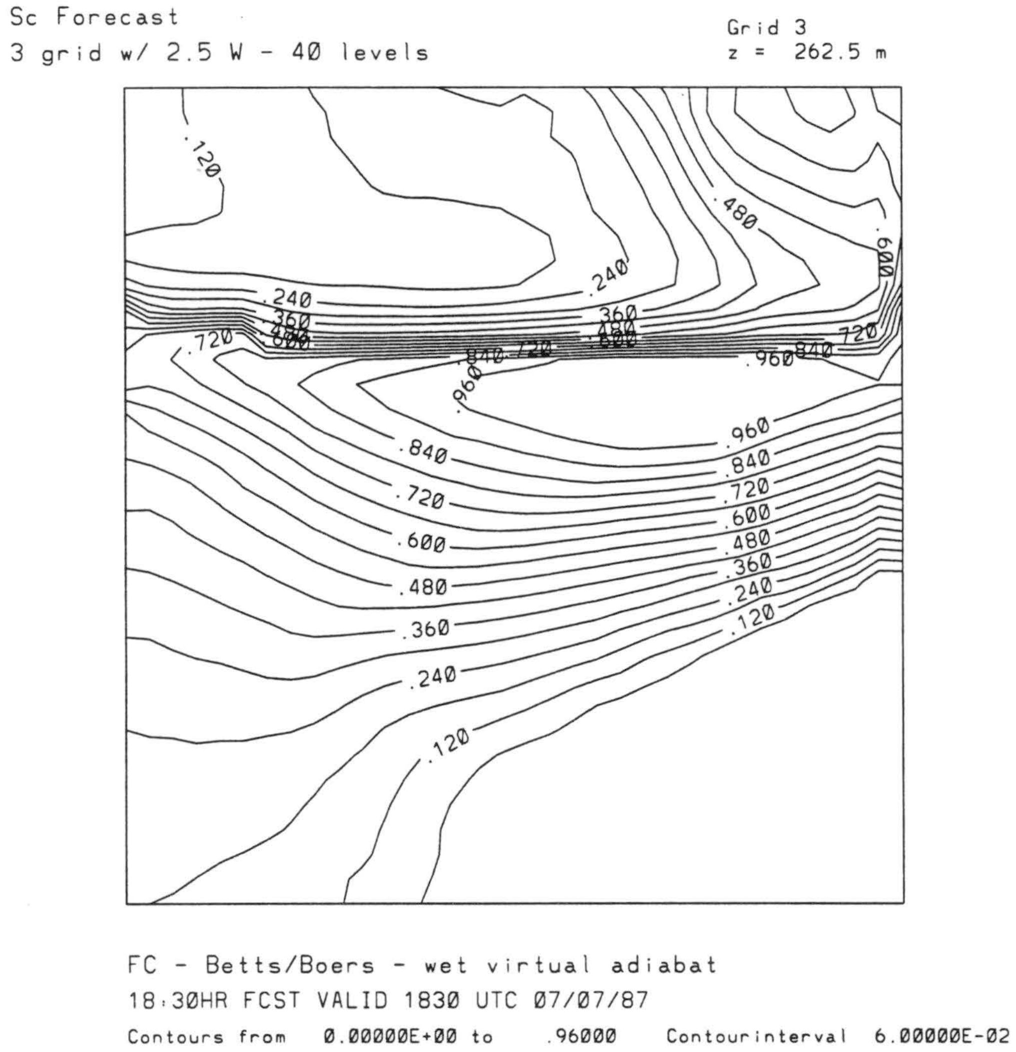

Figure 5.15: Betts and Boers' wet virtual adiabat fractional cloudiness scheme, from the RAMS third grid,valid 1830 UTC 7 July 1987.

this kink did match well with observations. A problem possibly similar to that described in the previous paragraph, however, may have caused the failure of this FC scheme for this application. Another possible problem could be uncertainties in the boundary-layer height and subsidence strength within the model.

The plot of Ek and Mahrt's FC scheme can be found in Figure 5.16. Again, the kink in the transition line was represented, and this scheme diagnosed the line well north of this kink. However, the fractional cloudiness in the southwest corner of the grid is much larger than that seen on the satellite imagery. The transition line here is much further west than

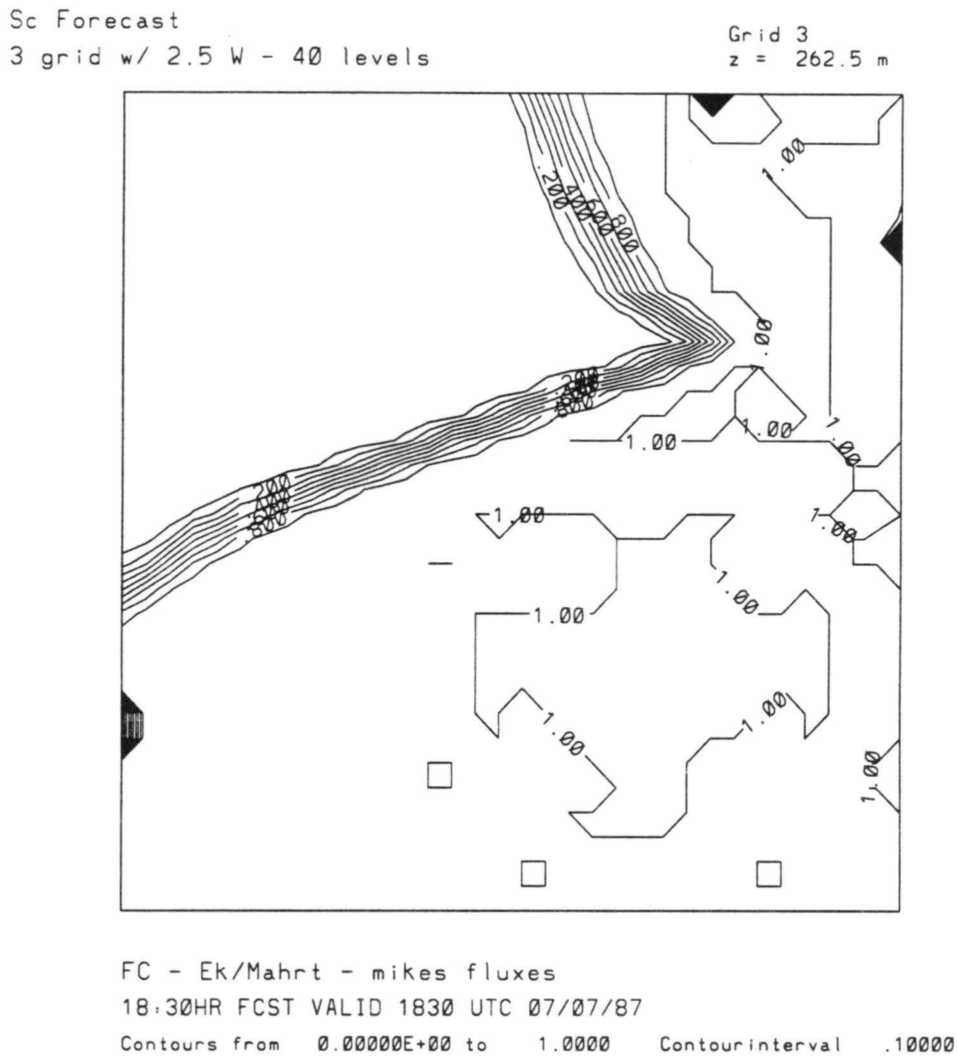

Figure 5.16: Ek and Mahrt's fractional cloudiness scheme, from the RAMS third grid, 262 m AGL, valid 1830 UTC 7 July 1987.

observed. It is probable that additional moisture was predicted by the model in this area, causing the scheme to diagnose higher values of FC.

The FC diagnosed from the Manton and Cotton scheme is shown in Figure 5.17. It diagnosed an FC of close to 1.0 throughout the grid. However, the FC did become close to zero at the transition line. This line somewhat matched the transition line from the satellite photo; thought it was not oriented north-south enough. To the west of the transition zone, the FC was shown to jump quickly back to 1.0.

This failure may be attributed to the small values of the variances and co-variances in the west area of the grid. This subgrid-scale FC scheme was built for subgrid-scale variances

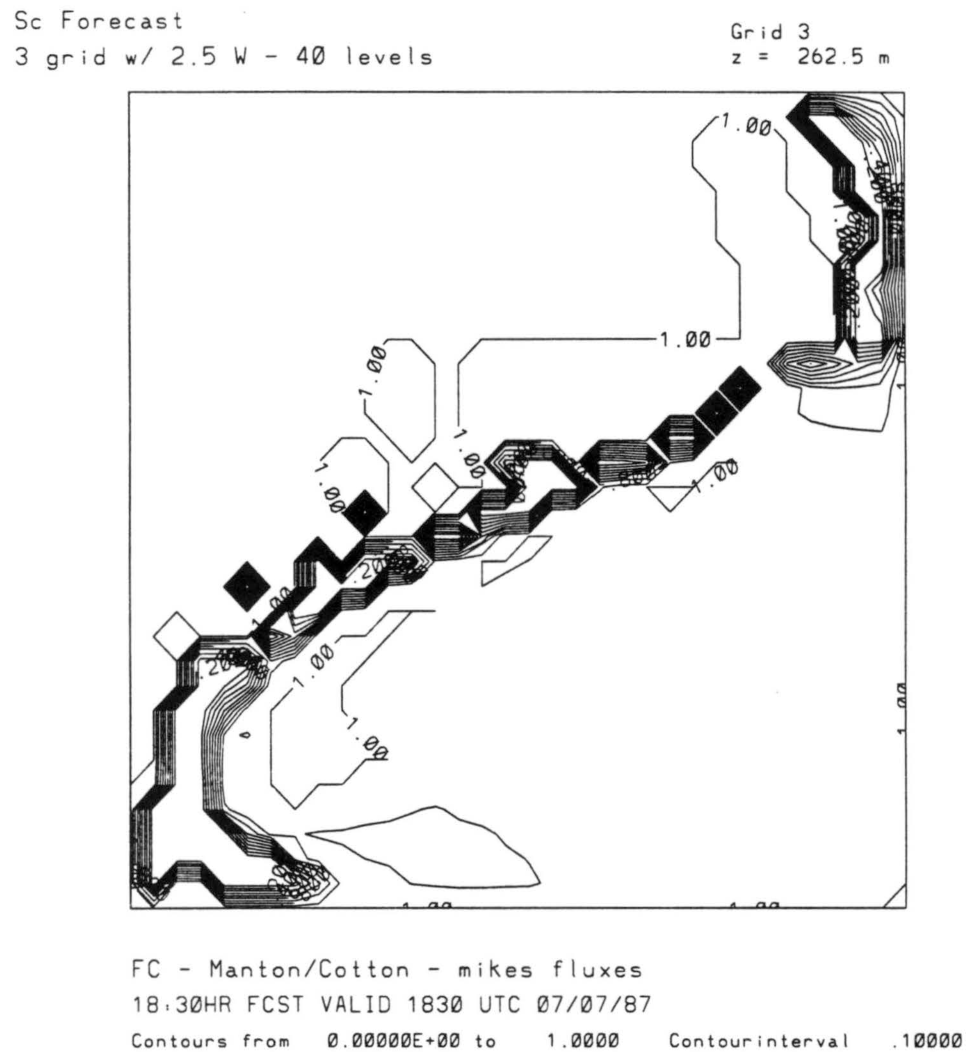

Figure 5.17: Manton and Cotton's fractional cloudiness scheme, from the RAMS third grid, 262 m AGL, valid 1830 UTC 7 July 1987.

and co-variances on the order of that typically observed in the atmosphere. The values of the perturbations could be: $\theta' \sim 0.1$ K, $r_t' \sim 10^{-4}$ kg/kg, and $w' \sim 0.1$ m/sec. The values on the west side of the transition zone were a few orders of magnitude lower than typical values. The small values for these variances and co-variances caused a small input to the error function, which could have cause the FC to go to zero for this area. The subgrid values from the Weissbluth parameterization to the east of the transition line are generally in agreement with values observed in the boundary layer.

The plot of Sommeria and Deardorff's FC is shown in Figure 5.18. At first glance, this plot looks similar to Manton and Cotton's. A few differences can be found, however. The

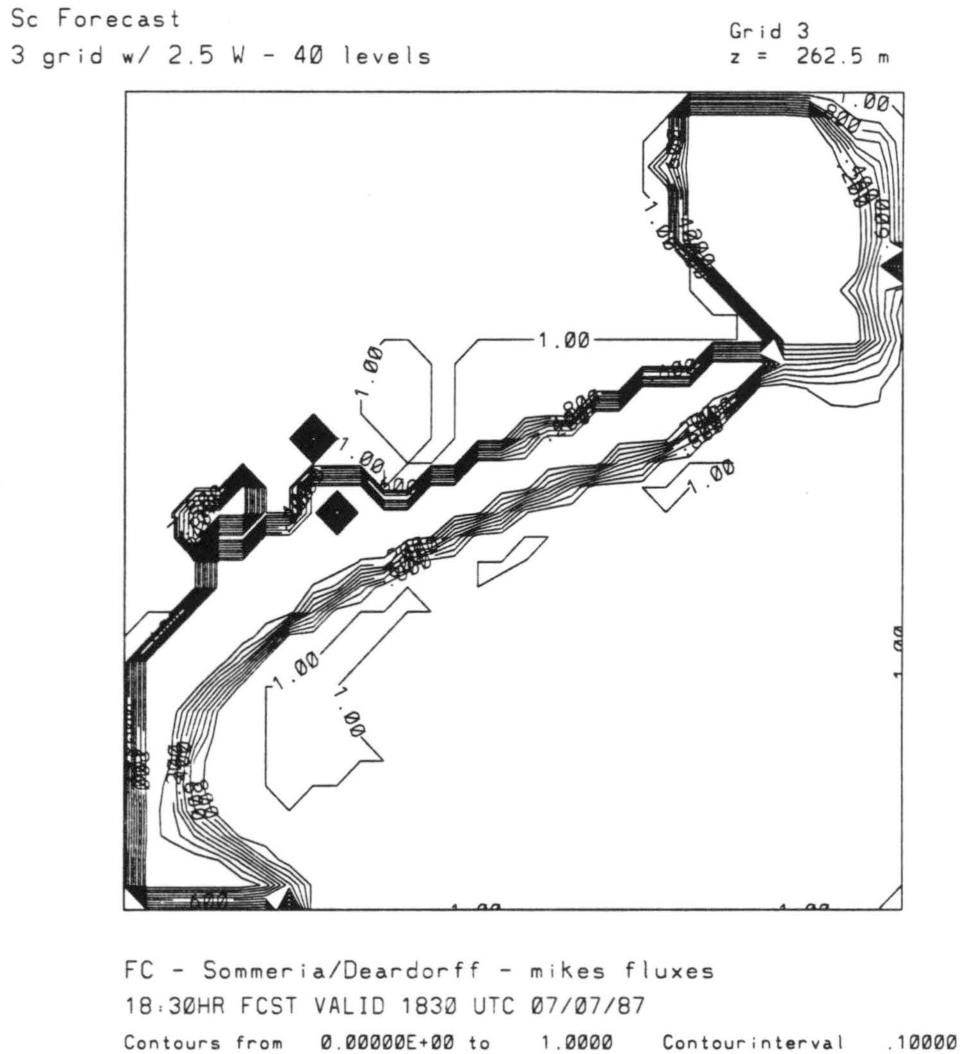

Figure 5.18: Sommeria and Deardorff's fractional cloudiness scheme, from the RAMS third grid, 262 m AGL, valid 1830 UTC 7 July 1987.

transition zone in Sommeria and Deardorff was diagnosed to be slightly wider. Also, the patchy area in the northeast corner of the grid was diagnosed to have an FC slightly lower. Again, however, the area west of the transition has an FC very close to 1.0. This problem may be the same as before in that the values of the variances were small in the west areas of the grid.

The result of using the Bechtold et al. FC scheme can be found in Figure 5.19. This plot is nearly identical to that of Sommeria and Deardorff. The problem of the scheme on the west side of the grid could again be as a result of small variances and co-variance values.

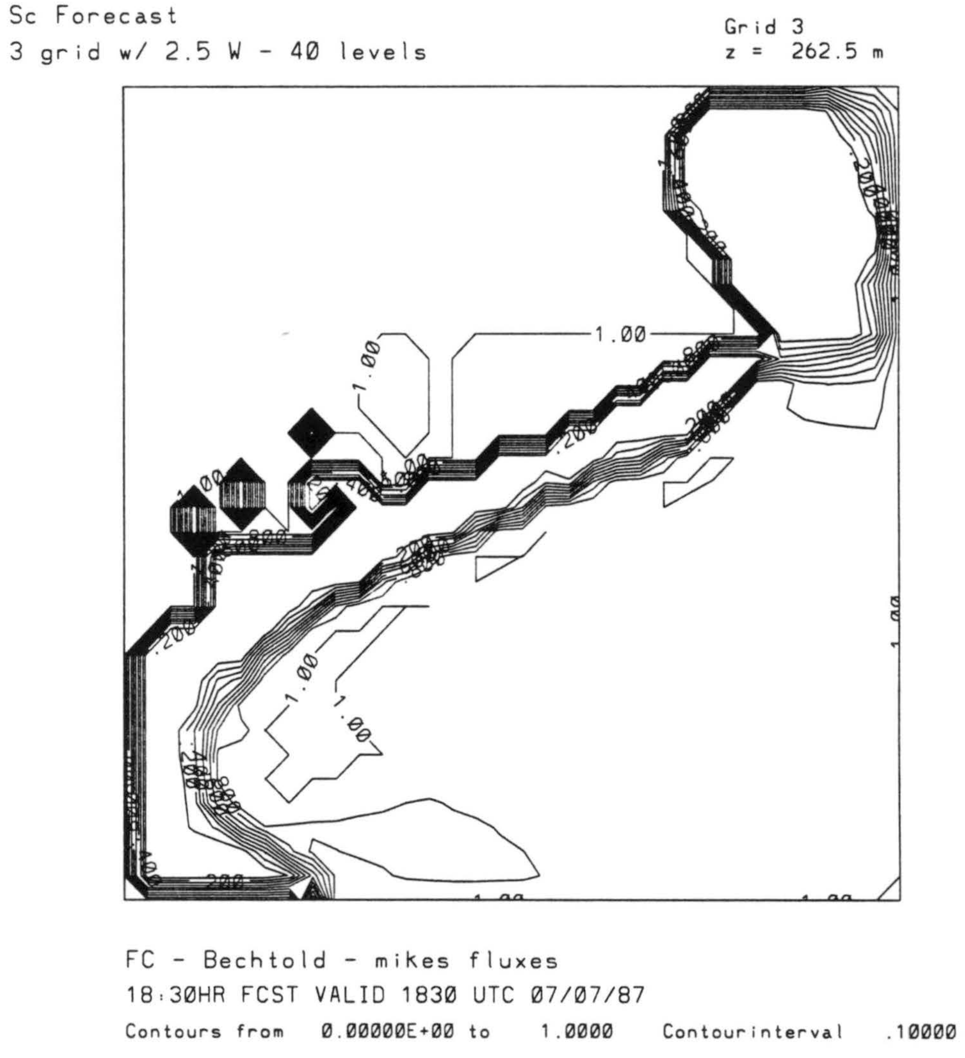

Figure 5.19: Bechtold et al.'s fractional cloudiness scheme, from the RAMS third grid, 262 m AGL, valid 1830 UTC 7 July 1987.

The width and location of the cloud transition for each of the FC schemes were compared to that from the satellite imagery. The cloud transition for this purpose was defined to be the area, from west to east, between FC = 0.0 and FC = .90. The width of this area is the width of the transition and the center of this area (from west to east) is the location of the transition. The width is given in km and the location is given in km east of the edge of the third grid.

From the LANDSAT image, the cloud transition was given as the area between where no clouds were found and where the clouds appeared to be reaching FC = .90. The width and location were defined as before. For this comparison, a representative east-west cross-section was taken across the top 1/3 of the third grid, center of the third grid, and bottom 1/3 of the third grid. The values from the FC schemes as compared to that taken from the satellite photo are given in Table 5.1.

From Table 5.1, it can be seen that the width of the transition diagnosed by the FC schemes is larger than that observed on satellite. It is probable that the transition line in the model not being along a true north-south line contributes to the diagnosed values being larger than observed. As the east-west cross-section is taken across the transition line tilted from north-south, the cross-section will go both somewhat across and along the line.

For the center of the transition, the middle and bottom regions generally show the FC schemes diagnosing the transition west of where it is found on satellite. This shift to the west has been seen in the plots from the third grid from the FC schemes. For the top region, the transition is, for the most part, diagnosed to the east of where it is found on satellite. The larger degree of scattered cumulus clouds may have caused this shift to east, as the schemes could have had difficulty diagnosing clouds in the cumulus area.

The values given by the Kvamstø and Sundqvist et al. schemes are identical in all three regions. This similarity is because these schemes share the same minimum threshold for cloudiness and because the slopes as a function of RH are very close at high RH's. The values from the Sundqvist et al. scheme are slightly lower within the transition zone - again because it is a sloping function of RH. It can be reasoned that the clouds on the satellite imagery also seem to exhibit a non-linear increase from no clouds to solid clouds.

Table 5.1: Comparison between the fractional cloudiness schemes and satellite imagery for three sections of the third grid.

Region	FC Scheme	Center of transition (km)	Width of transition (km)
Top			
	Albrecht	NG	NG
	Kvamstø	132.5	85
	Sundqvist et al.	132.5	85
	Ek & Mahrt	115	30
	Bechtold et al.	157.5	45
	Manton & Cotton	175	10
	Sommeria & Deardorff	155	50
	SATELLITE	125	49
Middle			
	Albrecht	112.5	5
	Kvamstø	67.5	95
	Sundqvist et al.	67.5	95
	Ek & Mahrt	52.5	55
	Bechtold et al.	82.5	85
	Manton & Cotton	107.5	25
	Sommeria & Deardorff	75	80
	SATELLITE	88	21
Bottom			
	Albrecht	42.5	5
	Kvamstø	30	100
	Sundqvist et al.	30	100
	Ek & Mahrt	20	80
	Bechtold et al.	30	30
	Manton & Cotton	35	20
	Sommeria & Deardorff	27.5	25
	SATELLITE	91	21

The subgrid-scale schemes seem to diagnose the transition zone generally as well as the other schemes. It should be recalled, however, that the FC = 1.0 in areas west of the transition for these schemes, as mentioned previously.

Both of the Betts and Boers FC schemes are not included in Table 5.1. The wet adiabat scheme diagnosed FC = 1.0 in all regions, and the wet virtual adiabat scheme diagnosed FC too haphazardly to find a cloud transition. In the top region, there was no transition identified by the Albrecht scheme.

5.3.2 Comparison to fractional cloudiness measurements

Betts and Boers (1990) used aircraft data to identify longitude boundaries between the cloudiness regimes. Based on these data, they determined a fractional cloudiness that is representative of the area, from clear, to cumulus, to broken, and to solid stratocumulus. The east-west line across which the transition was measured with aircraft was along 31.6° N. This latitude line is within the RAMS middle grid, south of the domain of the third grid. Betts and Boers report that the boundaries between the cloud regimes and each regime's cloud fraction are as found in Table 5.2.

Table 5.2: Boundary between cloud regimes and cloud fraction within each regime at 2032 UTC and 31.6° N (from Betts and Boers, 1990).

Region	Longitude of Boundary (°W)	Cloud Fraction
Clear		0.0
	122.64	
Cumulus		0.12
	121.91	
Broken		0.73
	121.57	
Stratocumulus		0.99

The fractional cloudiness for each parameterization programmed into RAMS was examined and compared to the observations as summarized in Betts and Boers (1990). Using the analysis package, the fractional cloudiness for each scheme was calculated for each regime across the transition line. The results of these calculations are summarized in Table 5.3.

Table 5.3: Comparison between the fractional cloudiness schemes and observations for each cloud regime.

Scheme	Clear	Cumulus	Broken	Stratocumulus
Albrecht	0.0	0.0	1.0	1.0
Kvamstø	0.07	0.77	1.0	1.0
Sundqvist et al.	0.02	0.52	1.0	1.0
Betts & Boers - wet adiabat	1.0	1.0	1.0	1.0
Betts & Boers - wet virtual adiabat	0.73	0.71	0.52	0.16
Ek & Mahrt	0.10	0.98	1.0	1.0
Bechtold et al.	1.0	0.0	0.99	0.97
Manton & Cotton	1.0	0.0	0.99	0.97
Sommeria & Deardorff	1.0	0.0	1.0	0.98
Observations	0.0	0.12	0.73	0.99

The values as reported in Table 5.3 reinforce the relative performance of each scheme as noted earlier in this Chapter. The Albrecht FC scheme identifies the transition line well, but diagnoses values of either 0.0 or 1.0. The Kvamstø scheme has the cloudy areas west of where they were observed, as does the Sundqvist et al. scheme. The slight westward bias of the transition line was noted earlier in this Chapter and persists at this time and location. The Sundqvist et al. scheme, which is a sloping function of RH, matches more closely the sloping change of cloud fraction as observed.

The Ek & Mahrt scheme diagnoses cloud fractions in a similar manner to Kvamstø and Sundqvist et al. The transition line is shown, but it is again shifted west of where it was observed.

Again, the Betts & Boers wet adiabat scheme is 1.0 at all places, as the boundary-layer in the model remains equally well-mixed in each cloud zone. The Betts & Boers wet virtual adiabat scheme again haphazardly diagnoses the fractional cloudiness across the transition zone.

The results from the subgrid-scale condensation schemes are also as before. West of the transition line, the fractional cloudiness is diagnosed to be 1.0, where it is observed to be 0.0. The cloud fraction dips to zero at the western edge of the transition zone, and then quickly rises back to near 1.0 in the broken and stratocumulus areas. A likely cause of the inability of these schemes to accurately represent the observed fractional cloudiness is the lower than expected values of the subgrid-scale variances and co-variances to the west of the transition.

Chapter 6

7 JUNE 1983

The Boundary Layer Experiment - 1983 (BLX83) took place in Oklahoma during the summer of 1983. The objective of the experiment was to study the interaction of the boundary layer and fair-weather cumulus clouds. Special attention was paid to the study of the entrainment zone and the relationship between thermals and turbulent motions.

The dates of the experiment were between 25 May and 18 June 1983. Remote sensors, surface observations, a high-density array of balloon soundings, and aircraft measurements were used to measure the boundary layer during the experiment. Lidar and sodar were also used, as well as turbulence sensors. For more information on BLX83, the reader is referred to Stull and Eloranta (1984).

Good conditions for the experiment existed during the time period. Most of the time was spent measuring during the day time, in order to study the evolution of the convective boundary layer (CBL). The case day chosen for this study, 7 June 1983, was selected because on this day boundary layer cumuli formed and dissipated during the daylight hours.

6.1 Observed conditions

On this day, a high pressure system was centered directly over Oklahoma. Relatively calm winds were observed over the state. The high pressure system moved very slowly to the south; however, no significant advection occurred over the area.

Small cumulus clouds began to form at about 11:00 a.m. local time. Cumulus humilis was reported throughout the day, slowly reaching up to 30 % coverage near 2:00 p.m. local. After this time, cloud coverage gradually decreased until 6:00 p.m. local time when nearly all clouds had dissipated. Reports from lidar and aircraft on 7 June are summarized in Table 6.1.

Table 6.1: Cloud coverage from lidar and aircraft reports during the afternoon of 7 June 1983 (from Stull et al., 1989).

Time (CDT)	Lidar Cloud Cover (%)	Aircraft Cloud Cover (%)
1000	0	NR (No Report)
1030	0	NR
1100	0.5	NR
1130	1	NR
1200	1	NR
1230	1-2	1-3
1300	10-15	10-20
1330	10-15	20-30
1400	15-20	20
1430	15	25
1500	10-15	30
1530	10-12	NR
1600	10	NR
1630	3	10-15
1700	2	2-5
1730	1-2	2-10
1800	3	0-3

6.2 Model set-up

For the Oklahoma simulations, only one grid was used. This grid had the same horizontal spacing as the finest grid from the FIRE simulations. The 5 km spacing was chosen because it is at this spacing that RAMS can handle the mesoscale circulations within the boundary layer. The grid had the same 40 vertical levels as the previous runs, with 42 grid points in each horizontal direction. The domain of the grid used for these simulations can be found in Figure 6.1.

For the most part, the options in RAMS described in Chapter 3 are the same options used for the Oklahoma simulations. The few differences will be mentioned here. The biggest change is that the model was initialized horizontally homogeneous. All grid columns in the domain were initialized to the 10:00 a.m. local sounding taken from Canton, OK. Canton is positioned at the center of the domain. The sounding used to initialize the simulations can be found in Figure 6.2.

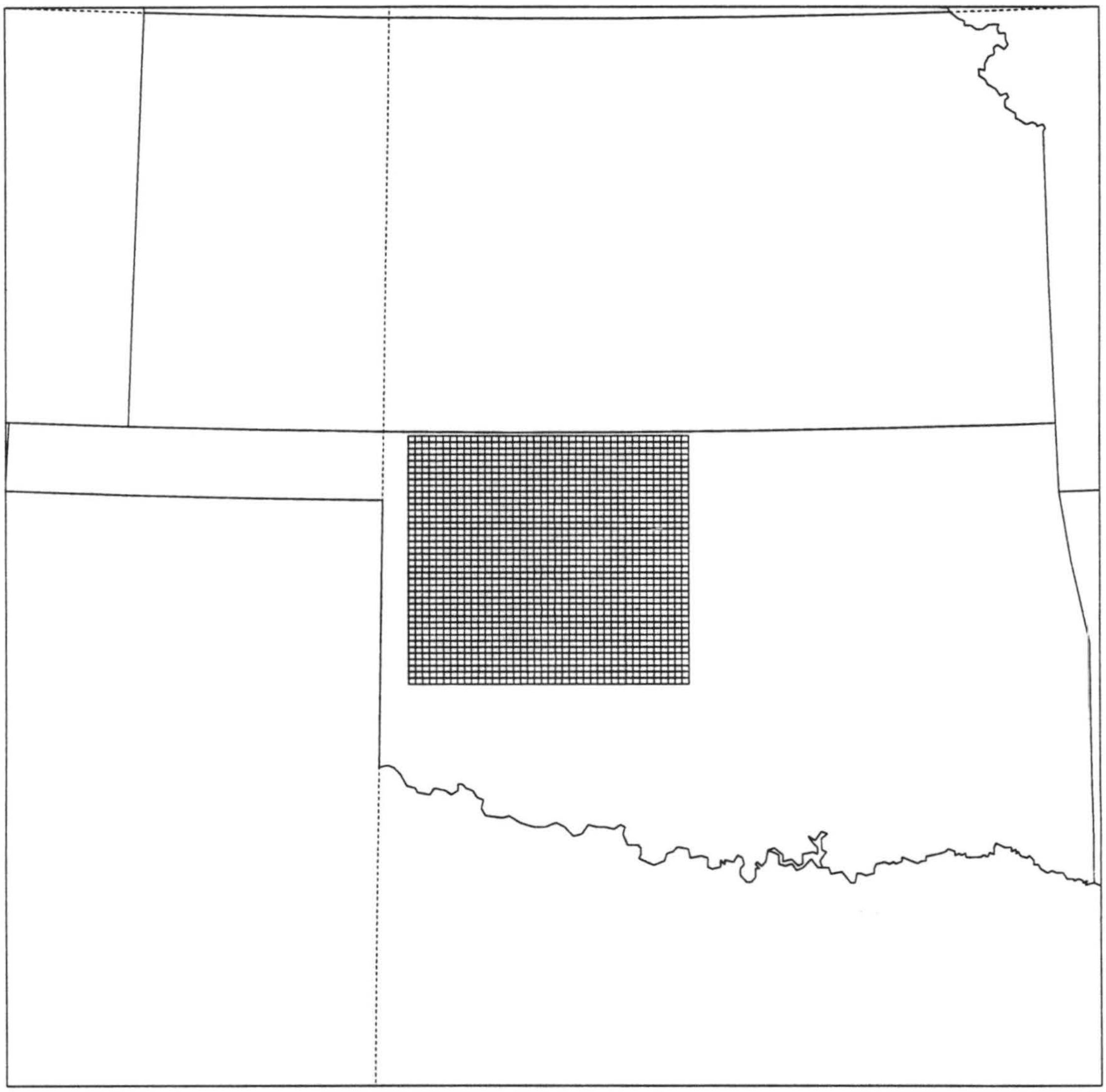

Figure 6.1: Grid showing domain of the RAMS configuration used for the Oklahoma simulations.

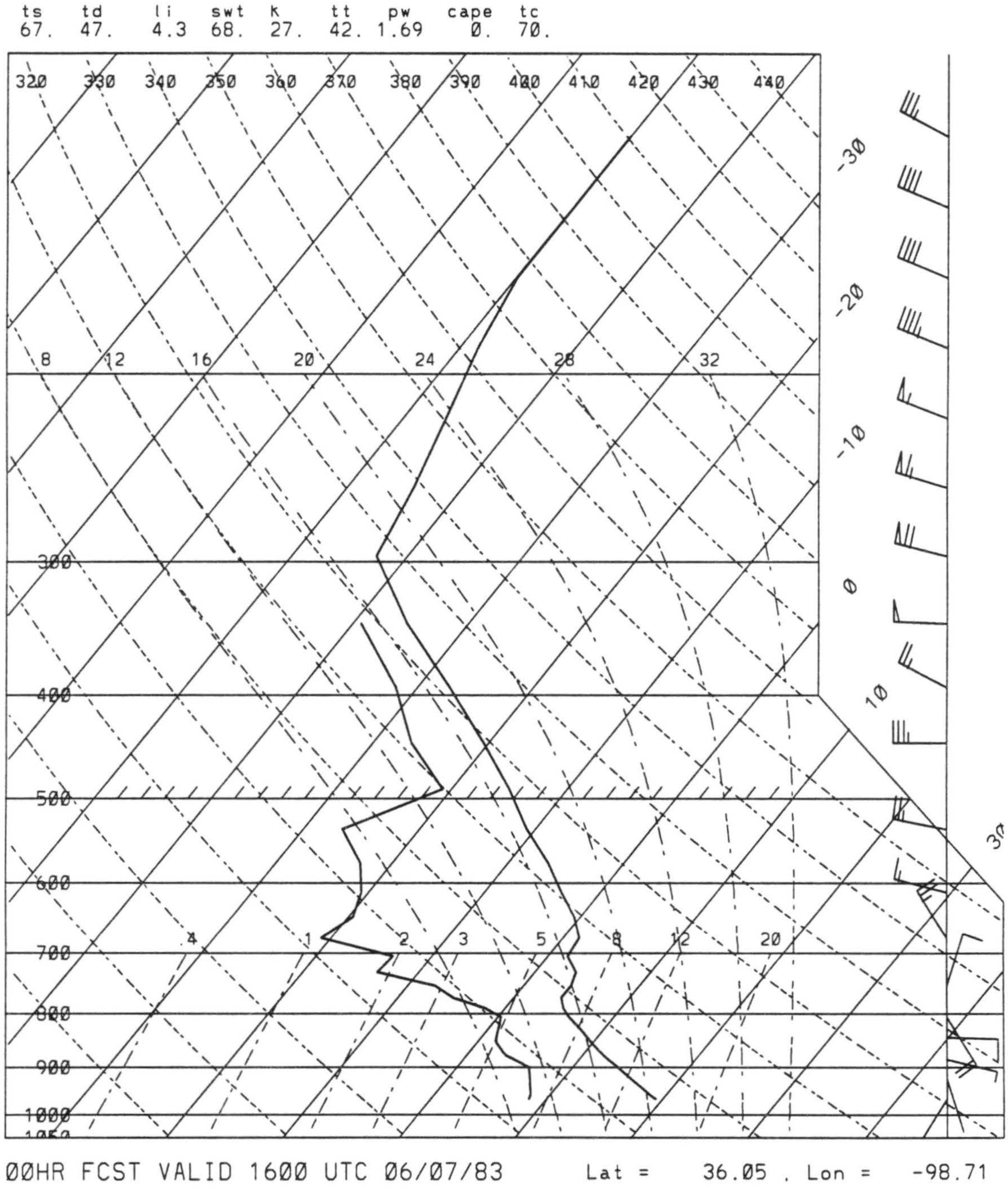

Figure 6.2: Sounding used for initialization of the Oklahoma simulations, taken at 10:00 a.m. local time, Canton, OK, 7 June 1983.

The model was run out 8 hours until 6:00 p.m. local time. The length of the simulation was chosen to allow the model to represent the development, growth, lifetime, and dissipation of the boundary layer cumuli observed during the day. The long time step of these simulations was 30 seconds, with a 3:1 long to short time step ratio.

Because the model was initialized horizontally homogeneous, the surface information at every grid point was also equal at the start of the simulation. The vegetation type chosen was mixed crop and farming, and the soil type chosen was loam. These types are generally observed in the Canton area. The temperature profile of the soil was set to be consistent with profiles observed during mid-morning. The microphysical inputs to the simulations were consistent with typical observations taken from similar air masses.

The final difference between the FIRE and BLX83 simulations turned out to be the most difficult to properly identify for the Oklahoma runs. The initial soil moisture profile (of which there were no readily available observations) had a large impact on the outcome of the simulation. Over twenty separate model runs were performed with only the initial soil moisture profile being changed between runs. Comparison of the temperature and moisture evolution at the surface in the model to that observed at Canton during the case study was the basis of the evaluation of the initial soil moisture values. Over the range of selected test values of the soil moisture (between 25 and 35 percent, depending on the soil level), a change of nearly 2 C in surface temperature and 1 g kg^{-1} in surface specific humidity were found. Also, a lowering of 2 % in the soil humidity at all soil levels produced a 6 % lowering in the relative humidity in the cumuli layer and a corresponding 32 % lowering of the fractional cloudiness by one of the schemes. The initial soil moisture profile finally chosen allowed the temperature and moisture profiles during the 8 hour period to match observations, and this profile is the initial state of the soil moisture used for the evaluation of all the fractional cloudiness schemes.

6.3 Comparison to observations

The results of the RAMS simulations for the Oklahoma case study agreed well with observations. Comparisons with surface data taken throughout the day were very similar to data taken from the model runs. The model also performed well in simulating the boundary layer height and cloud height when compared to radiosonde and observer measurements taken on the case day.

For these simulations, no noticeable north-south or east-west gradients in the predicted or diagnosed fields were found. This homogeneity was as a result of the model being initialized horizontally homogeneous. With the exception of the lateral boundary grid points, every x-y grid point value was nearly equal at a given model level. This was acceptable, as mentioned before, as no strong advection occurred on this case day.

Every plot in this section will therefore be a time-height cross-section of the center grid point. This point was chosen because it was the furthest away from the lateral grid points, because it allowed direct comparison to Canton, OK data, and because it was representative of the majority of the grid for these simulations. The time-height cross-sections have the time on the x-axis from the start of the simulation (10:00 a.m. local time) to the end of the simulation (6:00 p.m. local time). The z-axis for these plots is height through and above the boundary layer.

As can be seen in Figure 6.3, the vertical velocity variance increased slowly until just past midday. After midday, the maximum values of $\overline{w'w'}$ decreased, but the depth of large values continued to increase. The top contour, positioned near 2 km, corresponds with the observed 2000 m boundary layer height during the afternoon. The layer also became well-mixed during the afternoon, as can be seen in Figure 6.4. This figure also shows a boundary layer height near 2000 m.

6.3.1 Comparison of fractional cloudiness

Now the fractional cloudiness as determined by each scheme programmed into the analysis code will be examined. The Albrecht scheme did not produce any fractional cloudiness during the simulation. Both the saturation ratio and relative humidity remained below 0.9. With these relatively low numbers, no fractional cloudiness was produced with the Albrecht scheme. This scheme, which was built from typically observed numbers in a marine stratocumulus environment, may not be applicable for this study.

Both of the Betts and Boers schemes also did not diagnose any fractional cloudiness for the Oklahoma case study. There are two possible reasons for this. The first is that the

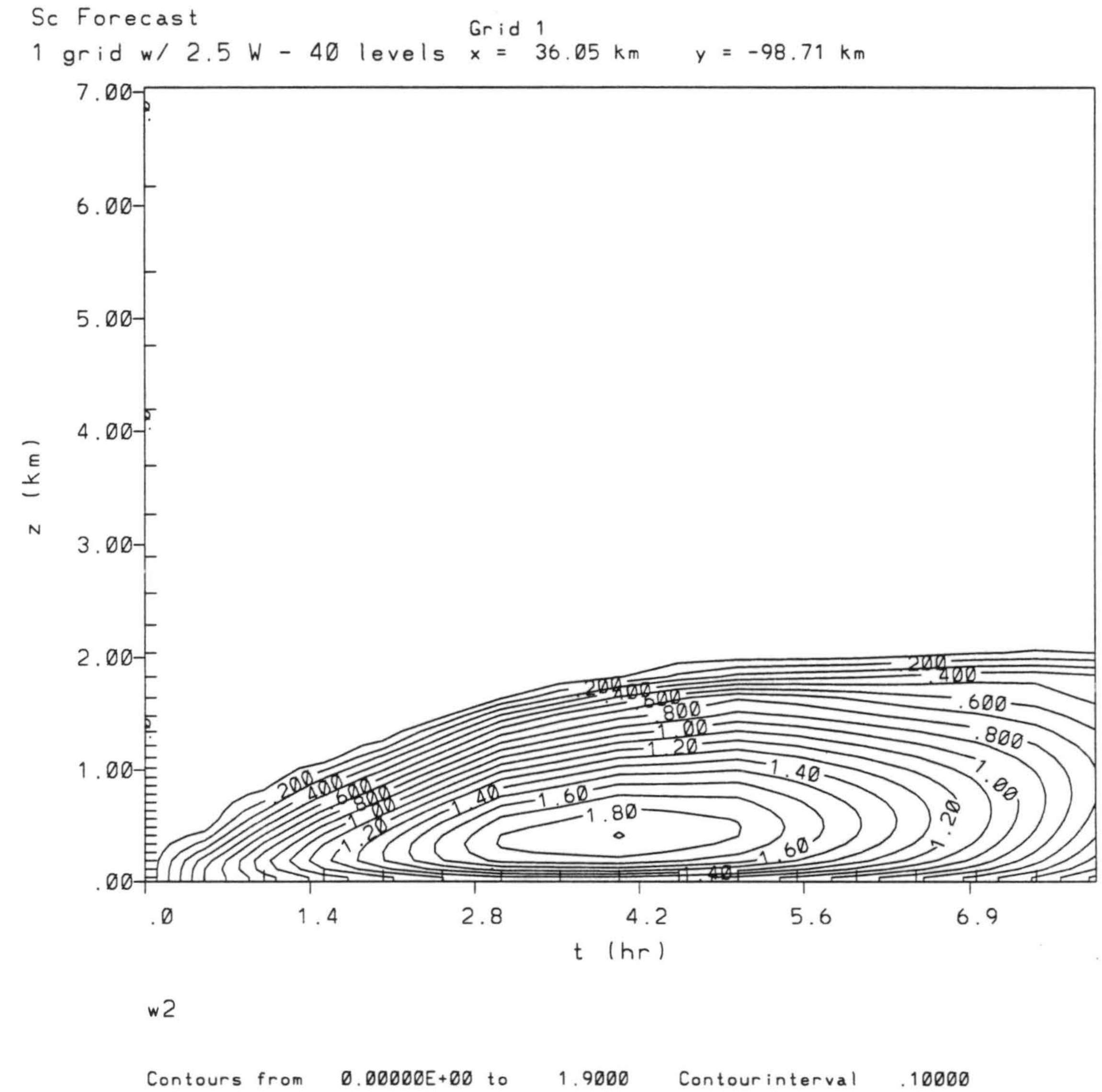

Figure 6.3: RAMS time-height prediction of vertical velocity variance for the center grid point.

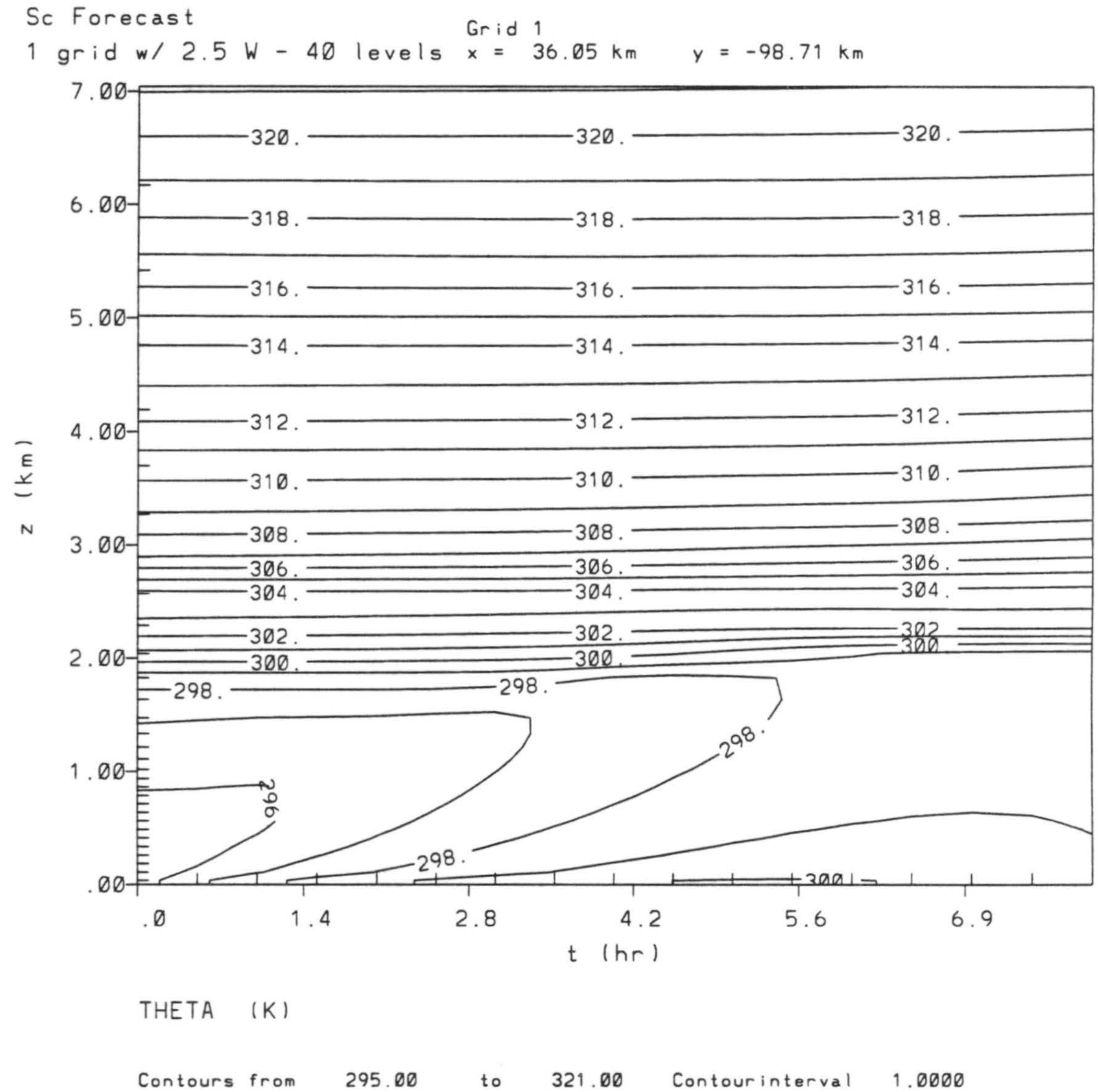

Figure 6.4: RAMS time-height prediction of potential temperature for the center grid point.

boundary layer was nearly equally well-mixed at all times during the simulation. As the mixing line slopes did not change much, neither would the fractional cloudiness as diagnosed by these schemes. The other possible reason is that these schemes were built for use on a marine stratocumulus-topped boundary layer, not a convective boundary layer. Different expected mixing line slopes may exist over land than over ocean, and it is possible that these schemes are not applicable to a convective boundary layer. There are also uncertainties in the height of the boundary-layer and the surface temperature which can adversely affect these schemes.

Both the Kvamstø and Sundqvist et al. schemes did diagnose fractional cloudiness during the simulation. Cloud base and cloud height compared well with observations. Onset of cloudiness, however, was almost 2 hours after it had been observed. After clouds had formed in the model, amounts did compare well with observations, except for the last hour of the simulation when the model diagnosed the fractional cloudiness to increase, when observations had the cloud amount decreasing to zero. The time-height cross section of fractional cloudiness from Kvamstø's scheme is shown in Figure 6.5 and that from Sundqvist et al.'s scheme is shown in Figure 6.6. There is a noticeable difference in cloud amount during the model run between the two schemes. This difference is because Kvamstø's scheme is a linear function of RH, while the Sundqvist et al. scheme is a sloping function of RH. The RH threshold for the onset of cloud in these schemes was 75 % because this simulation was over land.

The fractional cloudiness scheme of Ek and Mahrt is shown in Figure 6.7. It can be seen that this scheme diagnosed FC slightly earlier in the simulation than the previous two schemes, which was observed. Values are somewhat in line with observations. Again, there is an increase in FC towards the end of the simulation.

The fractional cloudiness determined from these three schemes as compared to observations can be found in Table 6.2. This table shows in greater detail what can be inferred from the time-height cross sections. The onset of cloudiness is generally after it was observed and the cloudiness persists longer than observed, including a re-development just before 1800 UTC. The magnitudes from the Sundqvist et al. scheme match more closely to the observations than the magnitudes from the Kvamstø scheme or the Ek and Mahrt scheme.

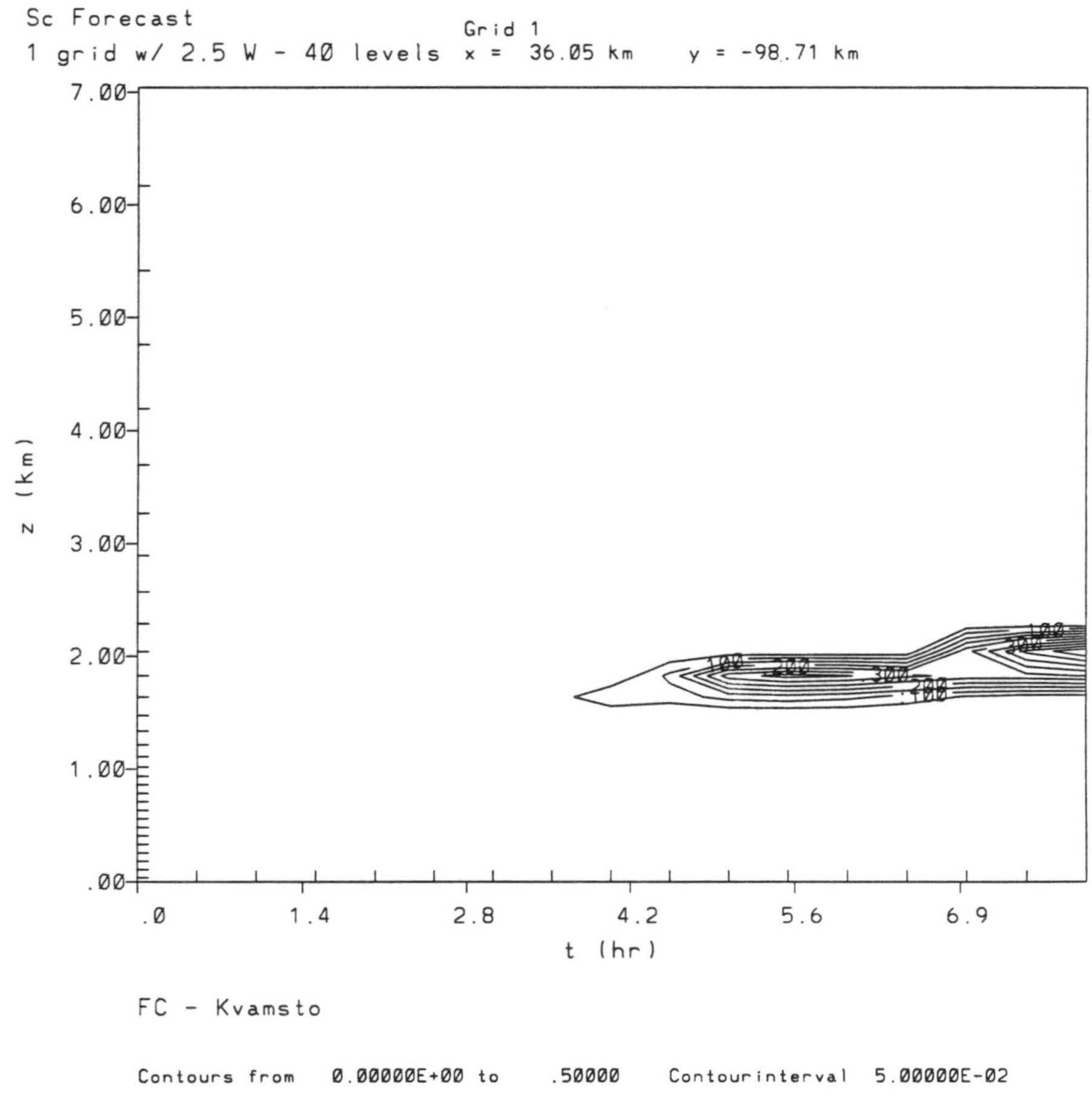

Figure 6.5: RAMS time-height determination of FC-Kvamstø for the center grid point.

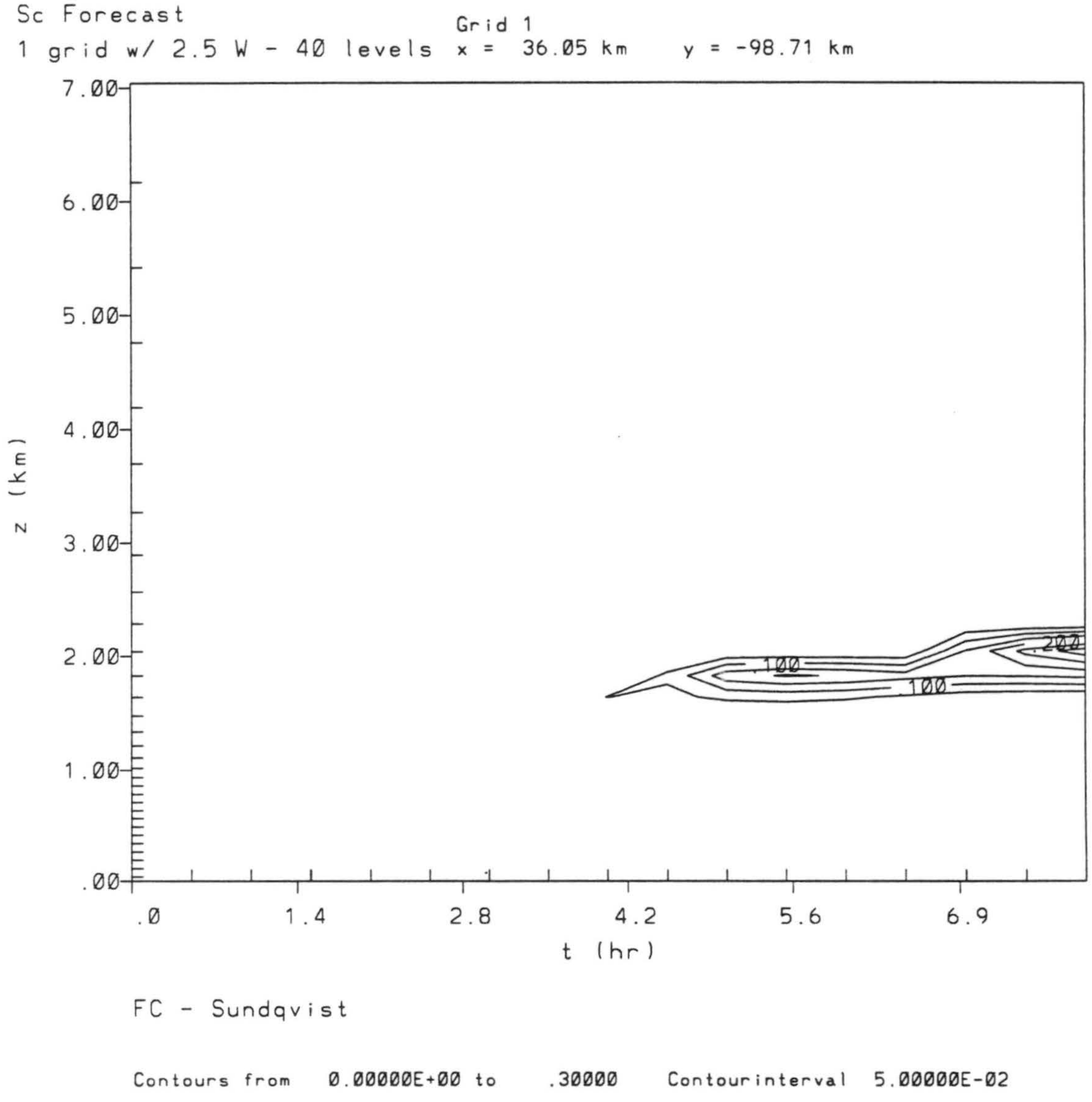

Figure 6.6: RAMS time-height determination of FC-Sundqvist et al. for the center grid point.

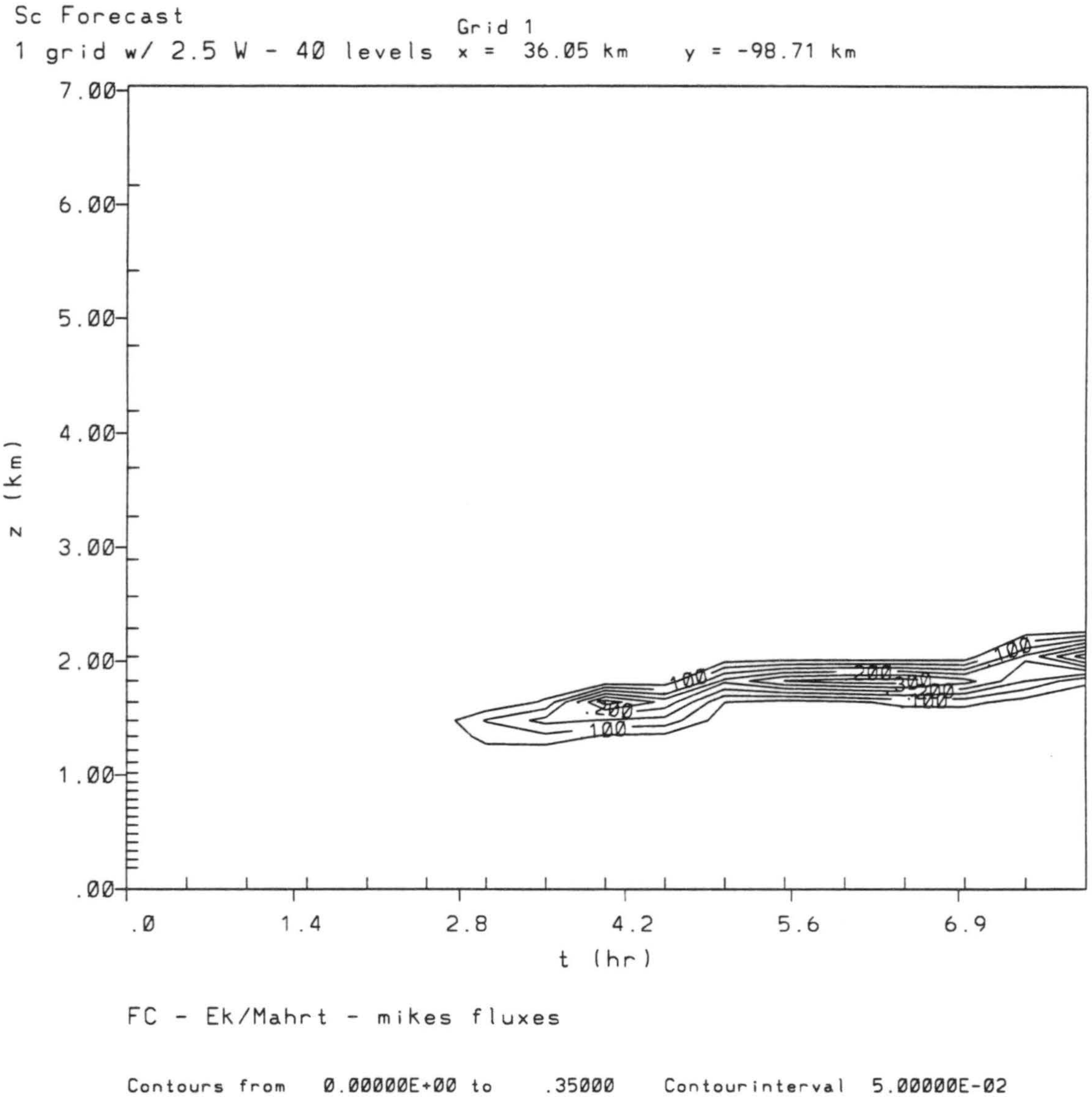

Figure 6.7: RAMS time-height determination of FC-Ek and Mahrt for the center grid point.

The magnitudes of the fractional cloudiness schemes can also be seen in a time-series plot in Figure 6.8.

Table 6.2: Cloud coverage from lidar and aircraft reports during the afternoon of 7 June 1983 (from Stull et al., 1989) compared to the fractional cloudiness through the boundary layer from the Kvamstø, Sundqvist et al., and Ek & Mahrt schemes.

Time (CDT)	Lidar	Aircraft	Kvamstø	Sundqvist et al.	Ek & Mahrt
1000	0.0	NR (No Report)	0.0	0.0	0.0
1030	0.0	NR	0.0	0.0	0.0
1100	0.005	NR	0.0	0.0	0.0
1130	0.01	NR	0.0	0.0	0.0
1200	0.01	NR	0.0	0.0	0.0
1230	0.01-0.02	0.01-0.03	0.0	0.0	0.0
1300	0.10-0.15	0.10-0.20	0.0	0.0	0.09
1330	0.10-0.15	0.20-0.30	0.0	0.0	0.16
1400	0.15-0.20	0.20	0.07	0.05	0.29
1430	0.15	0.25	0.11	0.07	0.23
1500	0.10-0.15	0.30	0.25	0.17	0.20
1530	0.10-0.12	NR	0.35	0.20	0.30
1600	0.10	NR	0.31	0.18	0.31
1630	0.03	0.10-0.15	0.28	0.16	0.30
1700	0.02	0.02-0.05	0.25	0.18	0.25
1730	0.01-0.02	0.02-0.10	0.45	0.25	0.21
1800	0.03	0.0-0.03	0.50	0.31	0.35

The subgrid-scale schemes performed almost in opposition to observations for this case. In areas where cloud was observed, these schemes diagnosed cloud amounts very close to observations. However, in all other areas of the domain, the fractional cloudiness was diagnosed to be 1.0. The failure of these subgrid schemes for this case may be a result of the low values of the turbulent fluxes as diagnosed from the Weissbluth parameterization. These values were lower than those expected for a convective boundary layer over land. The small flux values led to a large input to the error function within the fractional cloudiness schemes. The result of the Bechtold et al. scheme can be found in Figure 6.9 and the result

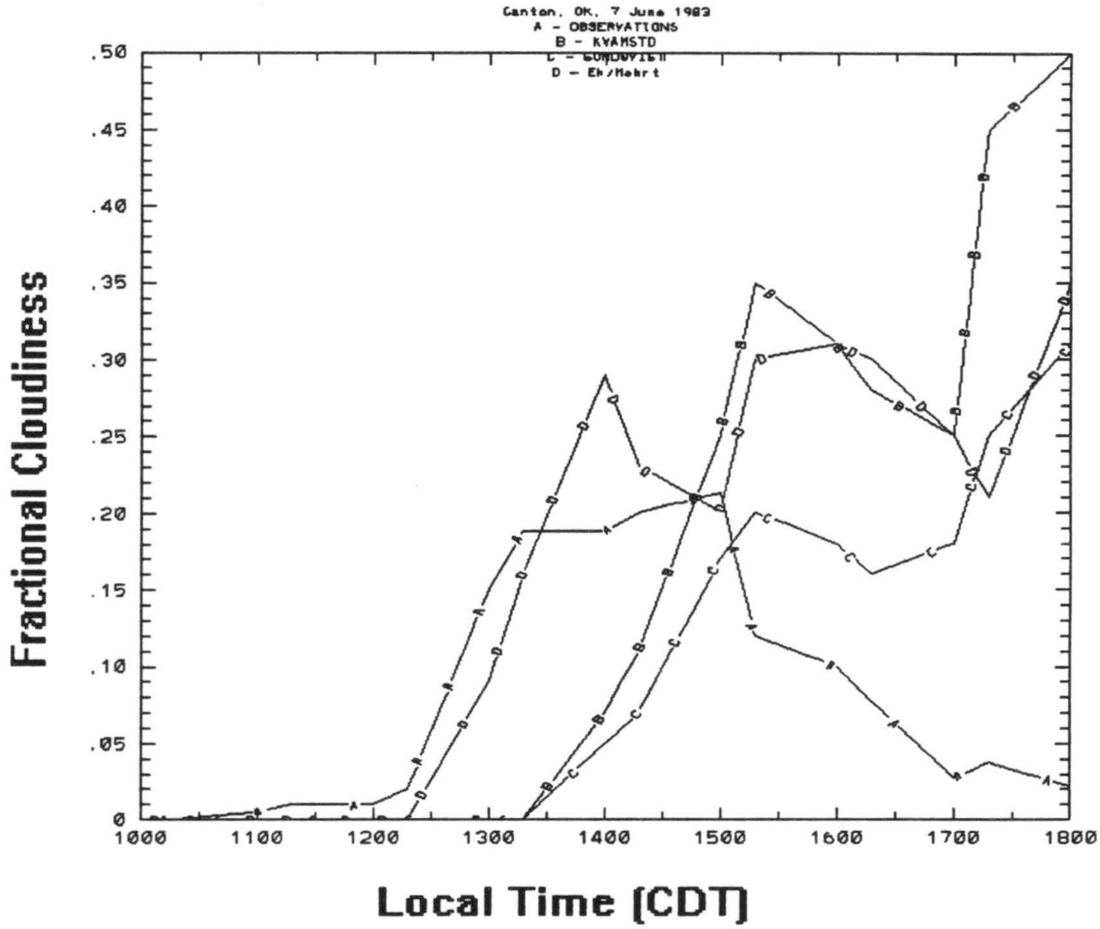

Figure 6.8: Time-series plot at the center grid point of fractional cloudiness through the boundary layer for: (A) observations; (B) Kvamstø; (C) Sundqvist et al.; and (D) Ek & Mahrt.

of the Manton and Cotton scheme can be found in Figure 6.10. The plot of Sommeria and Deardorff's FC is very similar to that of Bechtold et al., and is not shown.

Tables comparing the Albrecht and both Betts and Boers fractional schemes are not shown because the fractional cloudiness diagnosed remains 0.0 at all times during the simulation. Tables of the Bechtold et al., Manton & Cotton, and Sommeria & Deardorff schemes are not shown because of the haphazard nature with which the fractional cloudiness was diagnosed.

6.3.2 Comparison when modifying radiation

One area in which the model did not agree well with observations was in the timing of the breakup of the cloud layer. The relative humidity within the cloud layer in the

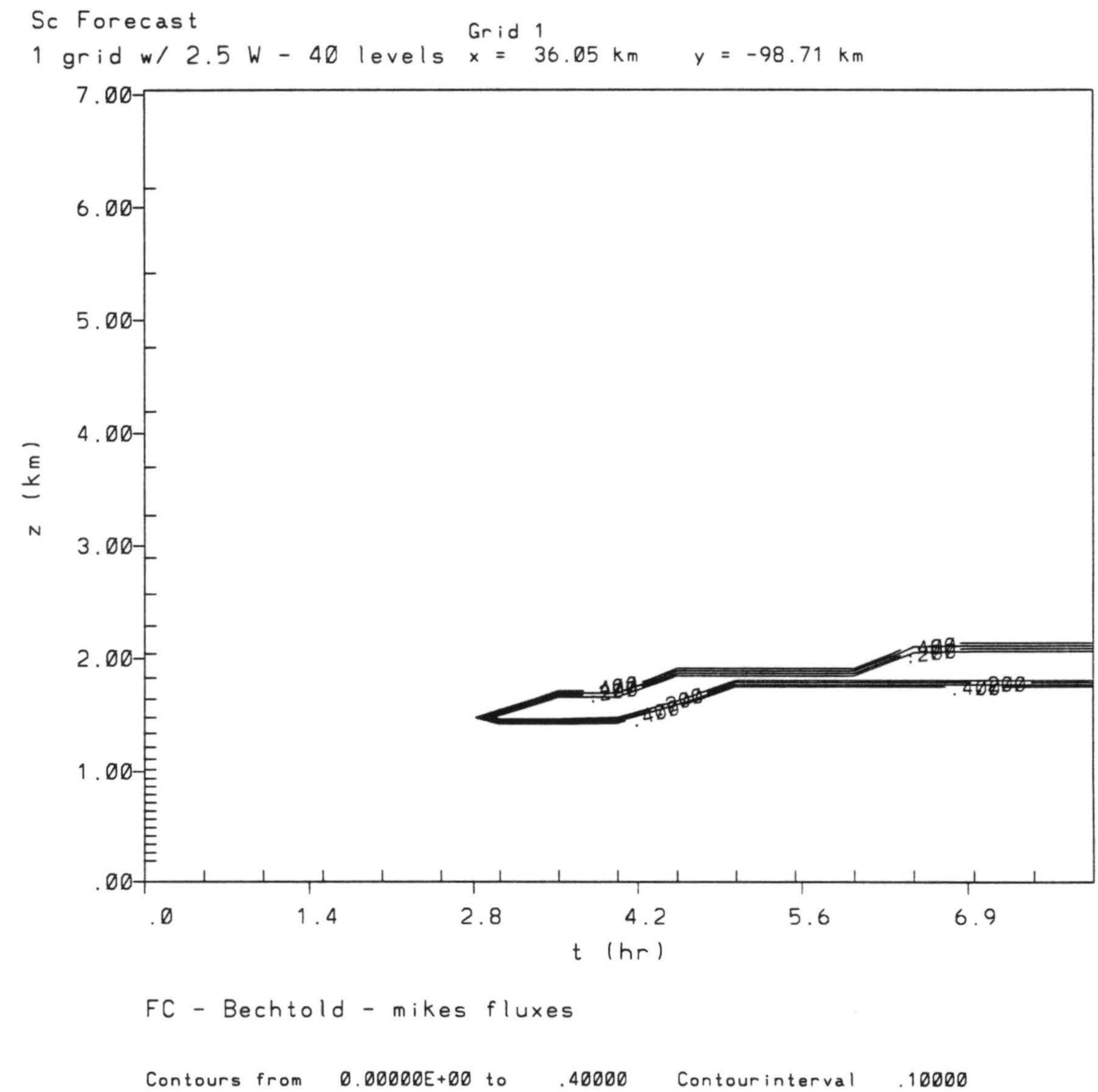

Figure 6.9: RAMS time-height determination of FC-Bechtold et al. for the center grid point.

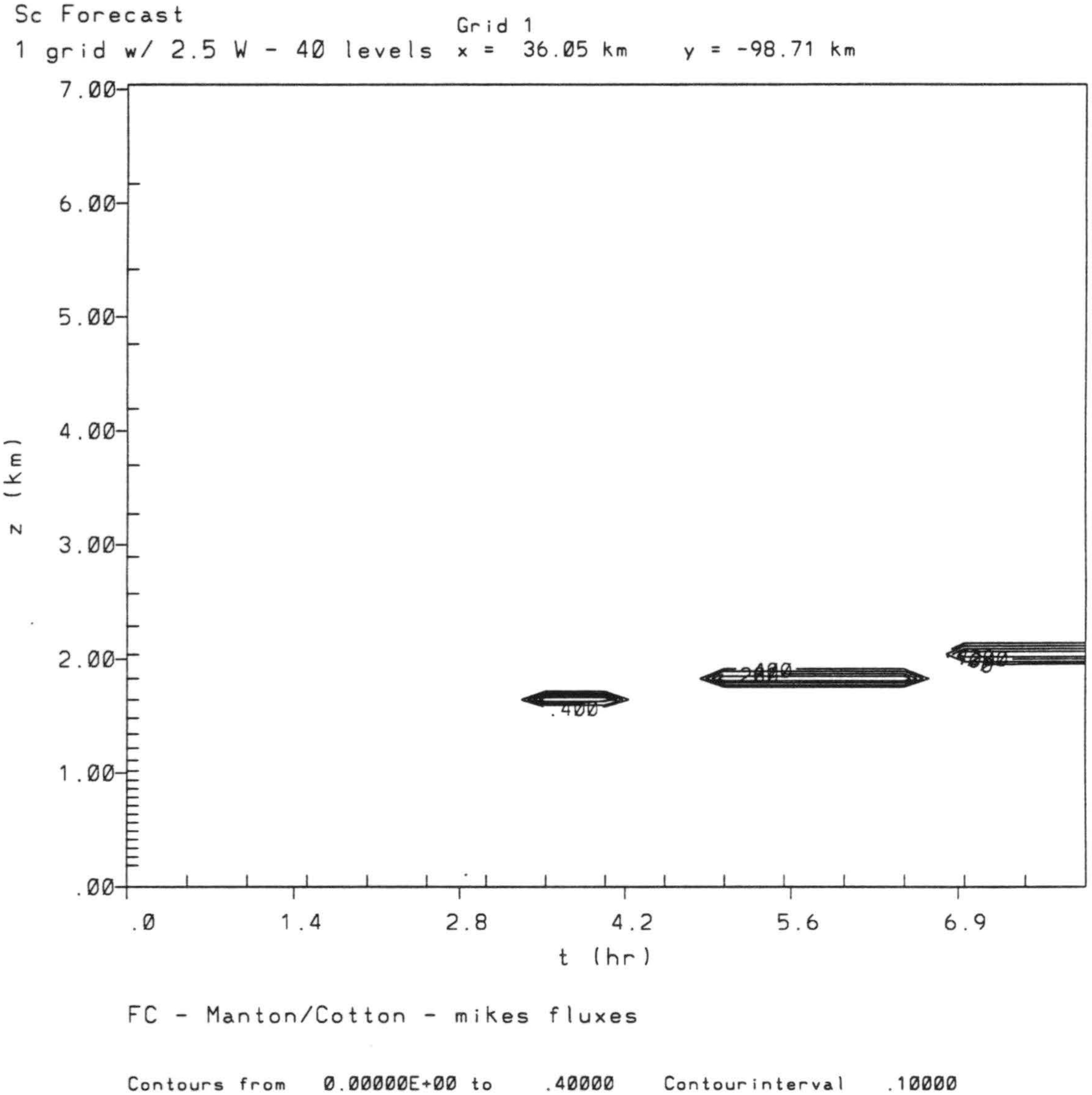

Figure 6.10: RAMS time-height determination of FC-Manton and Cotton for the center grid point.

model increased in the last hour and caused some of the fractional cloudiness schemes to also increase. Because the observations showed that clouds decreased during the 5:00 p.m. local to 6:00 p.m. local time frame, the model's performance during this last hour was in opposition to observations.

The most likely cause of the continued strengthening of the cloud layer during the last hour of the simulation is the radiative forcing. Because no cloud liquid water was diagnosed for this simulation, the radiative calculations were not affected by clouds anywhere within the model. The Chen and Cotton radiative scheme accounts for cloudiness only if cloud liquid water is produced. Therefore, buoyant forcing near the surface continued throughout the afternoon within the model and buoyant parcels continued to develop clouds at the top of the boundary layer.

In an attempt to change the non-dissipation of clouds near the boundary layer top, the radiation calculations were modified during the model run by the fractional cloudiness. This change differs from the earlier runs in that, before, the fractional cloudiness was used in a purely diagnostic manner. The FC was calculated only within the model's analysis package, while using it to affect the radiation required that it be calculated during the running of the model.

Having the fractional cloudiness modify the radiative calculations makes intuitive sense. A cloud layer with 30 % coverage should reduce the short wave radiation reaching the ground because these clouds would absorb or reflect this radiation. Similarly, scattered clouds as diagnosed by an FC scheme should increase the long wave radiation reaching the ground because the clouds would radiate at a higher temperature than the free atmosphere. These statements are true for radiation observations for boundary layer clouds.

The new radiation calculations were made in the following way. The fractional cloudiness scheme chosen to modify the radiation was that of Sundqvist et al. This scheme was chosen for two reasons: 1) it was very easy to program into the model code and 2) it seemed to perform closest to observations for this case, as shown in the previous section. The final radiation calculation was then a combination of two separate calculations. First, the radiation was calculated as if every grid-volume was completely filled with clouds. Next, the radiation was calculated as if every grid-volume was completely free of clouds. The results of these calculations were then combined using the fractional cloudiness. If the fractional cloudiness in a grid volume was 10 %, then the final radiation calculations was 10 % as a result of the complete cloud radiation calculation and 90 % as a result of the complete clear radiation calculation. The equation used for this is:

$$FINAL_{RAD} = (CLOUD_{RAD} - CLEAR_{RAD}) * FC + CLEAR_{RAD}. \tag{6.1}$$

If the fractional cloudiness at a given grid-volume was zero, the radiation was from the clear sky condition. If some FC was diagnosed, the total mixing ratio of water was temporarily changed. The total mixing ratio is what is used by the Chen and Cotton scheme to consider the effects of cloudiness. If there was cloud liquid water in the grid volume, the temporary total mixing ratio was set equal to:

$$r_{t_{TEMP}} = (r_{t_{ACTUAL}} - r_{sat})/FC + r_{sat}, \tag{6.2}$$

where r_{sat} is the saturation mixing ratio for that grid volume. If there was no cloud liquid water in the grid-volume, the temporary total mixing ratio was set equal to:

$$r_{t_{TEMP}} = r_{sat} * (1.0 + FC). \tag{6.3}$$

The temporary total mixing ratio was given to the Chen and Cotton radiation scheme for one set of calculations, and the actual total mixing ratio was given for another set of calculations. These two calculations correspond to considering complete cloud conditions and complete clear conditions. The results of the Chen and Cotton radiation scheme were combined using Equation 6.1.

There are advantages and disadvantages to having the fractional cloudiness modify the radiation calculations in this way. The largest advantage is that this method was relatively easy to program and to conceptualize. There are two large disadvantages, however. The first is that this method is only a crude approximation. The Chen and Cotton radiation scheme was built to allow the eventual addition of the fractional cloudiness parameter. Changing the radiative equations themselves, while more difficult from an engineering standpoint, will allow a more exact determination of having the FC affect the radiation.

The other drawback to the current method is that it requires the radiative equations to be solved twice. They are solved once when considering complete cloud and once when considering complete clear. Solving these equations was computationally expensive, despite being updated only every 900 model seconds. The Chen and Cotton radiation scheme calculations are very time-consuming and greatly slow down the model solution. Changing the radiative equations will allow the model to only have the Chen and Cotton radiation be calculated one time every time it is updated.

For the first model run when the fractional cloudiness modified the radiation, only the long wave and short wave radiation was affected. The vertical velocity variance from this run is shown in Figure 6.11. Comparing it to Figure 6.3, it can be seen that new simulation predicted lower amounts of $\overline{w'w'}$ in the lower boundary layer after 4.5 hours. This would indicate less surface forcing because the cloud layer is attenuating solar radiation.

The fractional cloudiness for the new simulation from the Kvamstø and Sundqvist et al. schemes are shown in Figures 6.12 and 6.13. As can be seen in the figures, nearly the same pattern of fractional cloudiness from each scheme was found when the long and short wave radiation was affected. Again, the increase of fractional cloudiness at the end of the simulation was found, in opposition to the observed decrease in cloud amount. The maximum cloud fraction at this time, however, was lowered by around 0.05 for each scheme in the last hour of the simulation.

The fractional cloudiness from the Ek and Mahrt scheme when the radiation had been modified is found in Figure 6.14. Again, nearly the same pattern was found. Towards the end of the simulation, however, the fractional cloudiness did not increase.

The fractional cloudiness from these three schemes when the radiation calculations were modified by the cloud fraction is shown in Table 6.3. Overall, the trends were similar to that shown in Table 6.2. The magnitudes were nearly the same at all times, except for the last hour of the simulation when the fractional cloudiness was reduced. A time-series plot of fractional cloudiness when the radiation calculations were modified can be found in Figure 6.15.

or the second model run when the fractional cloudiness modified the radiation, the long and short wave radiation was affected, as well as the radiative flux divergence. The

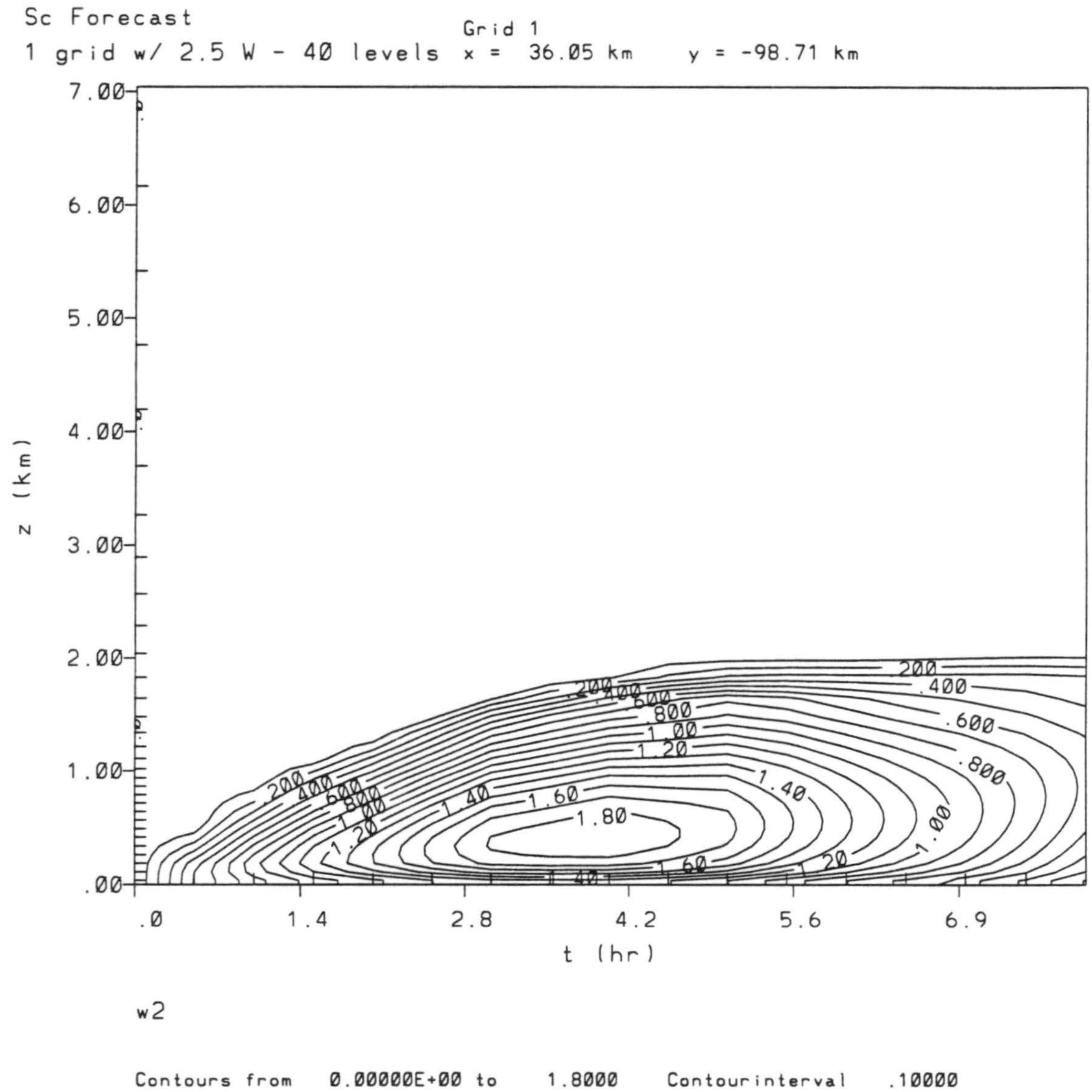

Figure 6.11: RAMS time-height prediction of vertical velocity variance for the center grid point when the long and short wave radiation have been modified.

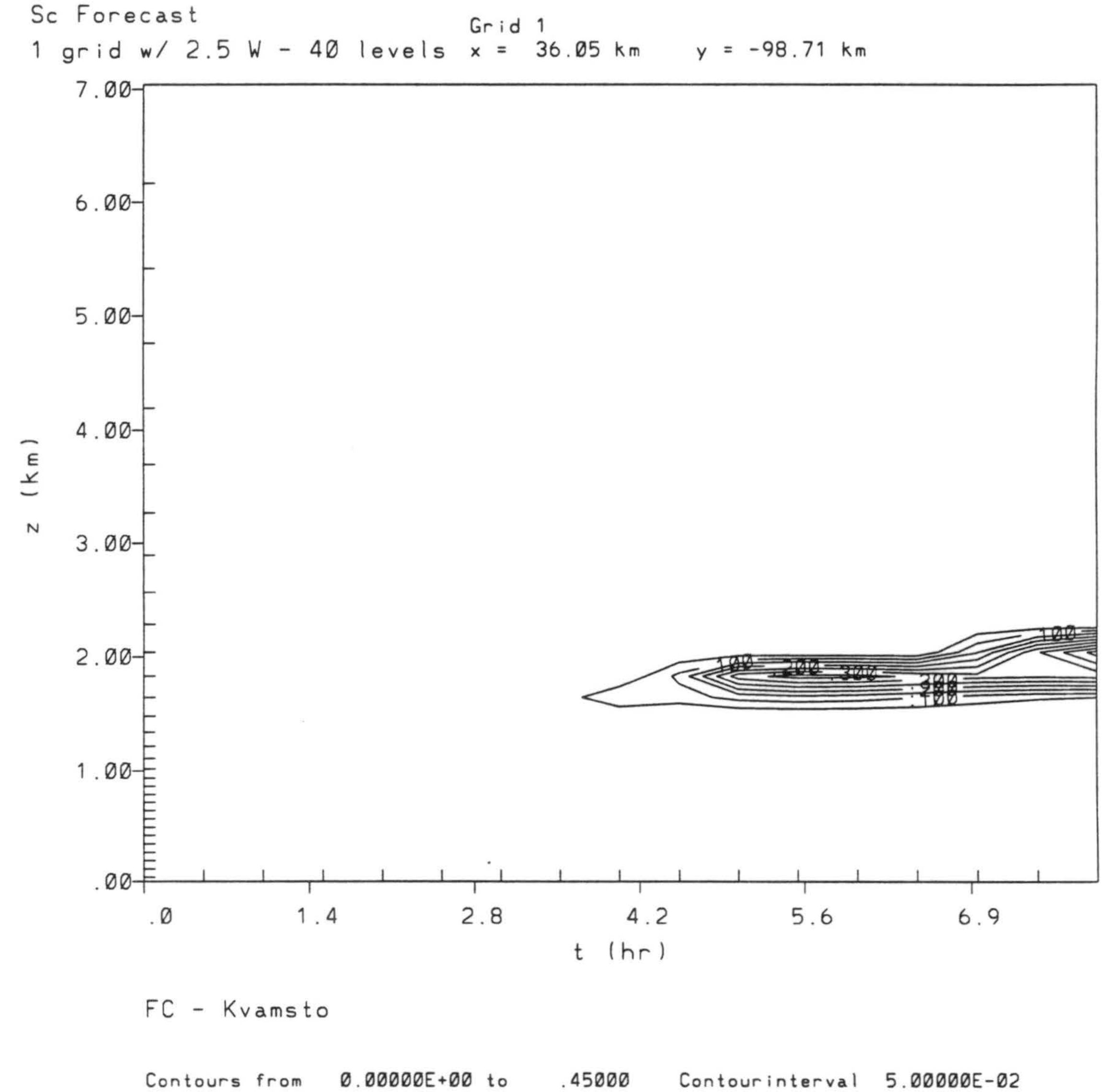

Figure 6.12: RAMS time-height determination of FC-Kvamstø for the center grid point when the long and short wave radiation have been modified.

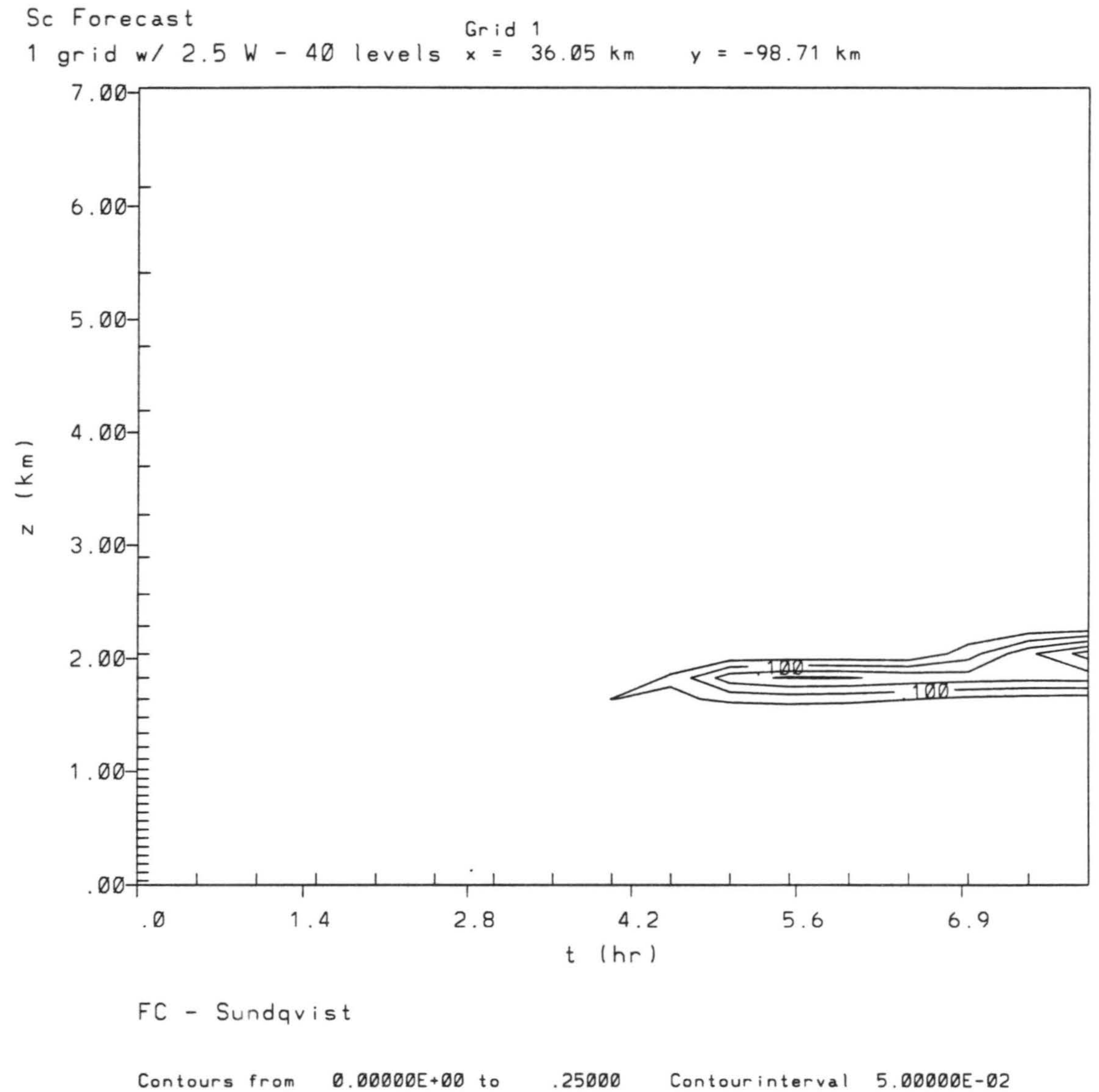

Figure 6.13: RAMS time-height determination of FC-Sundqvist et al. for the center grid point when the long and short wave radiation have been modified.

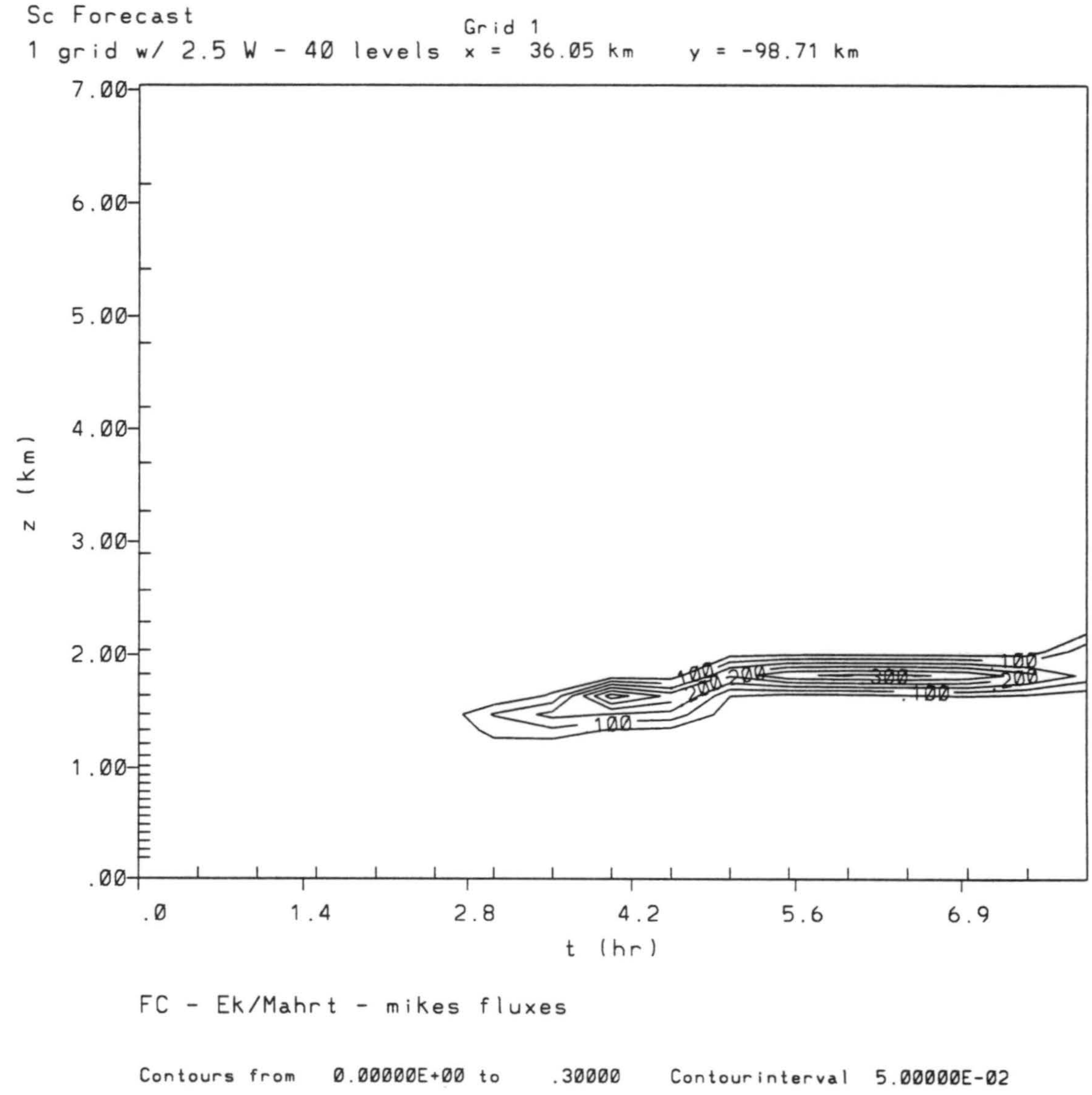

Figure 6.14: RAMS time-height determination of FC-Ek and Mahrt for the center grid point when the long and short wave radiation have been modified.

Table 6.3: As in Table 6.2, except for when the fractional cloudiness has modified the radiation.

Time (CDT)	Lidar	Aircraft	Kvamstø	Sundqvist et al.	Ek & Mahrt
1000	0.0	NR (No Report)	0.0	0.0	0.0
1030	0.0	NR	0.0	0.0	0.0
1100	0.005	NR	0.0	0.0	0.0
1130	0.01	NR	0.0	0.0	0.0
1200	0.01	NR	0.0	0.0	0.0
1230	0.01-0.02	0.01-0.03	0.0	0.0	0.0
1300	0.10-0.15	0.10-0.20	0.0	0.0	0.09
1330	0.10-0.15	0.20-0.30	0.0	0.0	0.16
1400	0.15-0.20	0.20	0.07	0.04	0.31
1430	0.15	0.25	0.11	0.07	0.22
1500	0.10-0.15	0.30	0.26	0.16	0.20
1530	0.10-0.12	NR	0.34	0.20	0.26
1600	0.10	NR	0.31	0.19	0.30
1630	0.03	0.10-0.15	0.30	0.17	0.30
1700	0.02	0.02-0.05	0.29	0.16	0.27
1730	0.01-0.02	0.02-0.10	0.34	0.19	0.21
1800	0.03	0.0-0.03	0.45	0.26	0.14

plot of vertical velocity is very similar to that of Figure 6.11 and is not shown. The fractional cloudiness schemes of Kvamstø, Sundqvist et al., and Ek & Mahrt are similar to the simulation when the radiation was not modified at all and are not shown.

Even though having the fractional cloudiness modify the radiation did lower the solar radiation reaching the earth and thus reduce the cloud forcing, the fractional cloud amount did not go to zero as observed in the final hour of the simulation. A possible cause for these boundary layer cumuli to completely dissipate within the model may therefore also be tied to the model's initial soil moisture. Although the initial soil moisture profile was chosen specifically to match the diurnal evolution of surface parameters, moisture from the soil may be finally reaching the upper mixed-layer by the end of the model runs and keeping the relative humidity in this area high. This effect may be overriding the effect of the buoyant forcing from the surface as determined from the radiation. A possible solution would be

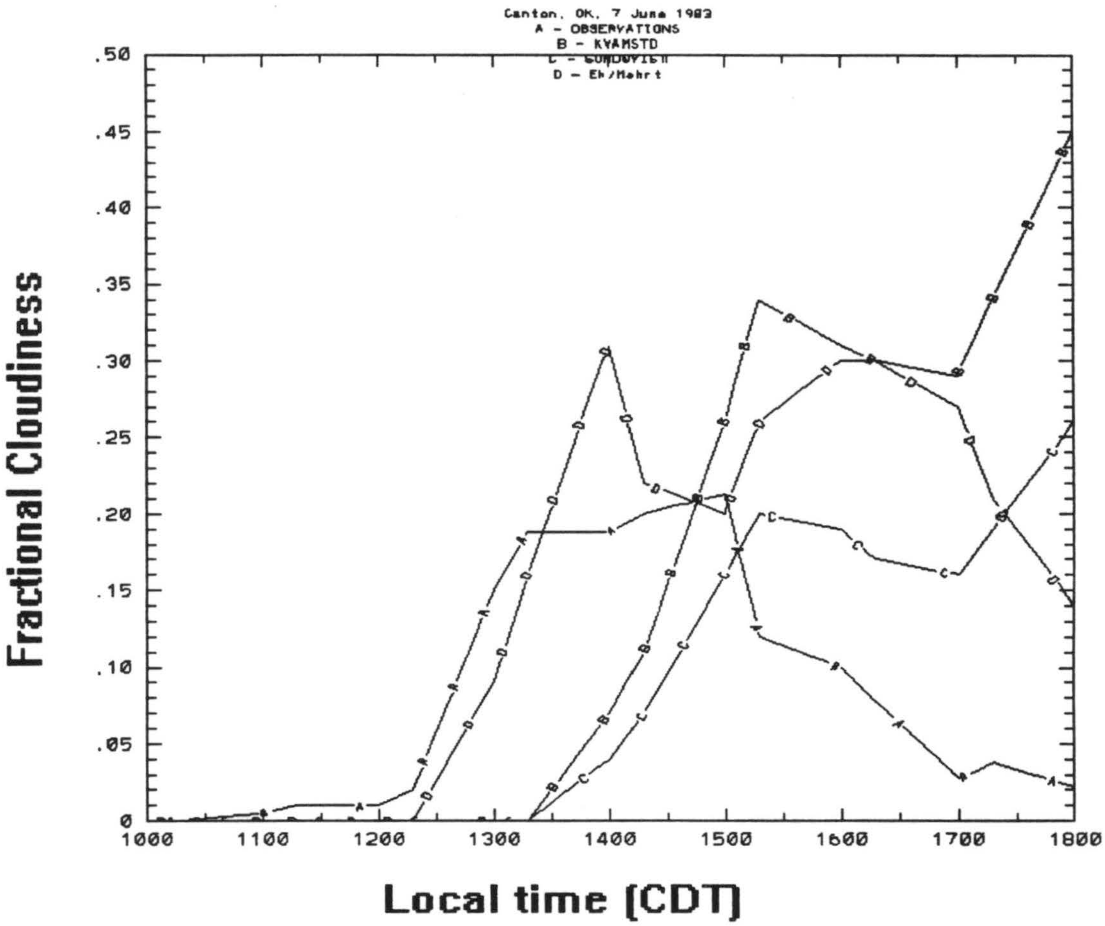

Figure 6.15: Time-series plot at the center grid point of fractional cloudiness through the boundary layer for: (A) observations; (B) Kvamstø; (C) Sundqvist et al.; and (D) Ek & Mahrt.

to tweak the initial soil moisture additionally until the relative humidity just below the inversion does not increase towards the end of the simulations.

Chapter 7

SUMMARY AND CONCLUSIONS

7.1 Summary

The primary goal of this paper was to compare and contrast the performance of various kinds of boundary layer fractional cloudiness schemes put into the RAMS model. Two separate case studies were used, one over ocean and one over land. The fractional cloudiness schemes were taken from papers from atmospheric science literature. The RAMS model used the Weissbluth turbulent parameterization for this study. This parameterization was used both because it added a predictive variable to RAMS and because it provided turbulent variances and co-variances needed for some of the fractional cloudiness schemes.

The RAMS model was set up with three interactive nested grids for the over ocean study. This study used the 7 July 1987 day from the FIRE I experiment, when a strong cloud transition from clear to overcast was observed. The performance of the simulations was shown to be nearly matched with observations. Some of the fractional cloudiness schemes were shown to capture the observed cloud transition while others were shown to have not captured the transition.

The RAMS model also was set up with one grid for the over land portion of the study. This study used the 7 June 1983 day from the BLX83 experiment, when scattered boundary layer cumuli formed and dissipated during the daytime hours. Strong sensitivity to initial soil moisture was found for these simulations. The model fields were similar to observations; however, most fractional cloudiness schemes were shown to not perform well in this part of the study.

The radiation calculations were next modified for the BLX83 model runs. The diagnosed fractional cloudiness helped to combine two separate radiation calculations, one when the grid-volume was considered to be completely filled with clouds and one when the grid volume was considered to be completely free of clouds. This acted to reduce the solar radiation reaching the ground and lower the buoyant forcing. Results were also shown for these simulations.

7.2 Conclusions

Some of the fractional cloudiness schemes put into RAMS had results which compared well to observations. Others did not perform as well. The usefulness of each of these schemes will now be critiqued on many different aspects, from ease of coding to performance under a range of implementations.

The Albrecht scheme generally identified areas of solid cloud or complete clear. However, no middle ground was observed. While this scheme was very easy to put into RAMS, it provided no additional information about cloud amount and location than that already possible with RAMS.

The Kvamstø and Sundqvist et al. schemes identified both partial and solid cloud areas very well. These schemes were very easy to code, and at the same time, offered the most reliable fractional cloudiness amounts among all of the schemes tested. A potential drawback of these schemes is that other cloud forcing information may exist in variables other than just relative humidity. These schemes may not work as well for smaller grid spacings. Sundqvist et al. may be slightly preferred because it is not a simple linear function of relative humidity and it compares a little better with observations.

The Betts and Boers wet adiabat and wet virtual adiabat schemes did not prove to be very useful. These schemes may be tied too closely to conditions observed on the day from which they were developed. The RAMS model did not produce the same conditions to the accuracy which they were observed. If the boundary layer is too evenly mixed, no gradient in fractional cloudiness from these schemes will be observed. The Betts and Boers parameterizations were also very difficult to put into the RAMS model.

Ek and Mahrt's scheme performed reasonably well for this study. Partial success when compared to observations was found. It was also relatively easy to encode this parameterization into RAMS. This scheme may improve as the cutoff in the distribution is tested for its best application within the RAMS model.

Table 7.1: Brief review of good points of using each fractional cloudiness scheme

FC Scheme	Good Points
Albrecht (1989)	Shows observed FC transition nicely Easy to apply to mesoscale model
Kvamstø (1991)	Shows observed FC transition nicely FC amounts diagnosed well compared to obs. Easy to apply to mesoscale model
Sundqvist et al. (1989)	Shows observed FC transition nicely FC amounts diagnosed well compared to obs. Easy to apply to mesoscale model Not a linear function of RH as is Kvamstø
Betts & Boers (1990)	Diagnoses on mixed-layer information
Ek & Mahrt (1991)	Shows observed FC transition nicely FC amounts diagnosed well compared to obs. Relatively easy to apply to mesoscale model
Bechtold et al. (1992), Manton & Cotton (1977), and Sommeria & Deardorff (1977)	Diagnoses on turbulent values

The subgrid-scale condensation schemes, Manton and Cotton, Sommeria and Deardorff, and Bechtold et al. all were a little bit disappointing. Results did not compare at all to observations and it proved quite difficult to code these parameterizations. The results may improve if the horizontal grid spacing is dramatically lowered, as these schemes are most applicable to small grid spacings.

A brief review of the good points of each fractional cloudiness scheme used for this study can be found in Table 7.1. Conversely, a quick look at the bad points of each scheme can be found in Table 7.2.

Overall, the Kvamstø, Sundqvist et al. and Ek & Mahrt schemes performed the best for these case studies. They matched observations, especially in the trend of fractional cloudiness in time and space. The magnitudes from the Sundqvist et al. scheme were slightly closer to observations for both case studies.

These three schemes also stand out because they will probably perform consistently well for most applications of RAMS (or other mesoscale models). Many applications of mesoscale modeling use grid spacings varying between 5 and 100 km. These have demonstrated high

Table 7.2: Brief review of bad points of using each fractional cloudiness scheme

FC Scheme	Bad Points
Albrecht (1989)	Amount of FC typically either 0.0 or 1.0
Kvamstø (1991)	Diagnoses only on relative humidity Other cloud forcing information may be lost
Sundqvist et al. (1989)	Diagnoses only on relative humidity Other cloud forcing information may be lost
Betts/Boers (1990)	FC transition does not match with observations Produces FC in column, not in volume May work only for a strict set of conditions Difficult to apply to mesoscale model
Ek/Mahrt (1991)	Need to have moisture flux information from model Problems with model having maximum RH = 100 %
Bechtold et al. (1992), Manton/Cotton (1977), and Sommeria/Deardorff (1977)	Very difficult to put into mesoscale model Model grid spacing chosen not perfect Diagnosed FC in large no-cloud areas Highly dependent on magnitudes of subgrid values

degrees of success when used on grids with spacings between 5 and 80 km as shown for the two case studies.

The level of uncertainty for the Kvamstø and Sundqvist et al. is lower than for the other schemes. The greatest uncertainty is in the distribution of moisture. Boundary-layer variances and co-variances, surface fluxes, inversion height, etc., do not (directly) affect the inputs to the Kvamstø and Sundqvist et al. cloud fractional parameterizations.

For the Ek and Mahrt FC scheme to be used, information on moisture flux must be diagnosed from a mesoscale model. This scheme has the nice feature of having the horizontal grid spacing used in the model configuration built into the calculation of FC.

These parameterizations are finally preferred because they are easily transportable between models and are not difficult to code. This transportability allows the fractional cloudiness to be used during the model run and under a wide array of model configurations.

7.3 Suggestions for future research

Suggestions for future research into diagnosing fractional cloudiness in a mesoscale model can be divided into three categories: improving and changing the model set-up, adding additional and improving existing fractional cloudiness schemes, and improving the evaluation of the fractional cloudiness schemes. Work in any three of these areas will increase understanding of the relative performance of a fractional cloudiness parameterization.

The first way the model set-up can be improved is to use vertical grid nesting for the FIRE I model runs. The 75 m vertical grid spacing proved too coarse to resolve all of the cloud features within the FIRE I target area. It was not desirable, however, to lower this spacing everywhere within the grid, as this would increase the time it would take the model to reach a solution and it would cause additional numerical problems in areas over land. These numerical problems can occur as a result of strong vertical motions over land which may move mass through a vertical grid volume within the model time step. Version 3a of RAMS, which has been newly released, allows vertical grid nesting within fine grids. A suggestion would be for 25 m vertical grid spacing, or smaller, to be used on Grid 3, with 100 m vertical grid spacing on other grids.

Another way the model set-up can be improved is to obtain a more complete initialization data set for the FIRE I runs. There is an obvious scarcity of observations in the Eastern Pacific. Better observations in this area may have allowed model prediction to match more closely with observations and allowed the improved performance of the fractional cloudiness schemes.

The model set-up can also be improved by modifying the radiative calculations and/or buoyancy fluxes to explicitly represent fractional cloudiness, as opposed to the current method. As mentioned previously, changing the way the Chen and Cotton radiation scheme includes fractional cloudiness will allow the model solution to be reached quicker and will allow a more exact radiative solution. Having each fractional cloudiness scheme put into RAMS affect the radiation in a separate simulation should also be mentioned here. Also, re-running the FIRE I simulation with the FC-modified radiation would also be insightful.

The calculated fractional cloudiness can also feedback into the flux divergence determinations. A fractional weighting can be performed between the flux divergence when the grid-volume is saturated and when the grid-volume is clear. This weighting would be important in the air but play little role at the ground.

Future research into the fractional cloudiness schemes put into the RAMS code is also suggested. For instance, changing the relative humidity threshold in the Kvamstø or Sundqvist et al. schemes can be studied. Also, a study into the most appropriate center of the Gaussian distribution from the Ek and Mahrt FC scheme can be done. Finally, it would be helpful to run the case studies with many different horizontal grid spacings to evaluate the performance of each FC scheme for a wide range of spacings.

There is also the potential for putting additional fractional cloudiness schemes into RAMS. In the atmospheric science literature, new fractional cloudiness schemes are continually being proposed. It may also be possible for a researcher to develop a new fractional cloudiness parameterization specifically for RAMS. This new scheme could be a result of an in-depth study of other model data and how these data relate to many different case studies.

Finally, the evaluation of each fractional cloudiness scheme in this study can be improved. Statistical methods in a comparison between observed and model fractional cloudiness can be used. It may be possible to digitally transfer the information in the LANDSAT imagery showing the transition into a fractional cloudiness at each grid point on the RAMS third grid. The percentage of every grid square that returns a cloud pixel could be used as verification data. The verification data could then be run through a statistical algorithm to objectively evaluate the performance of each fractional cloudiness parameterization. It is also possible to use the lidar and aircraft observations from BLX83 as observational data in a statistical evaluation.

There is also potential for future field projects to provide further case studies of fractional cloudiness. These projects could more accurately document the fractional cloudiness, and this data could be used in further comparisons to model output. It would be very helpful to have access to a fractional cloudiness data set that provides information for every grid-volume in the model configuration at one or more times during the case day. The Atlantic Stratocumulus Trade-wind EXperiment (ASTEX), which took place during the summer of 1992 in the Eastern Atlantic Ocean, may provide some cases against which RAMS and the fractional cloudiness parameterizations may be further evaluated.

REFERENCES

Albrecht, B.A., 1989: Aerosols, cloud microphysics, and fractional cloudiness. *Science,* **245,** 1227-1230.

—, 1991: Fractional cloudiness and cloud-top entrainment instability. *J. Atmos. Sci.,* **48,** 1519-1525.

—, D.A. Randall, and S. Nicholls, 1988: Observations of marine stratocumulus clouds during FIRE. *Bull. Amer. Meteor. Soc.,* **69,** 618-626.

Arakawa, A., and V.R. Lamb, 1981: A potential enstrophy and energy conserving scheme for the shallow water equations. *Mon. Wea. Rev.,* **109,** 18-36.

Ballard, S.P., B. Golding, and R.N.B. Smith, 1991: Mesoscale model experimental forecasts of the haar of northeast Scotland. *Mon. Wea. Rev.,* **119,** 2107-2123.

Banta, R., 1979: Subgrid condensation in a cumulus cloud model. *Sixth Conference on Probability and Statistics in Atmospheric Sciences, Preprint Volume,* 9-12 Oct 1979, Banff, Canada, 197-202.

Barnes, S.L., 1973: Mesoscale objective map analysis using weighted time series observations. ERL NSSL-62 NTIS COM-73-10781, NOAA, 60.

Bechtold, P., C. Fravalo, and J.P. Pinty, 1992: A model of marine boundary-layer cloudiness for mesoscale applications. *J. Atmos. Sci.,* **49,** 18, 1723-1744.

Bechtold, P., J.P. Pinty, and P. Mascart, 1993: The use of partial cloudiness in a warm-rain parameterization: A subgrid-scale precipitation scheme. *Mon. Wea. Rev.,* **121,** 3301-3311.

Betts, A.K., and R. Boers, 1990: A cloudiness transition in a marine boundary layer. *J. Atmos. Sci.,* **47,** 12, 1480-1497.

Boers, R., and A.K. Betts, 1988: Saturation point structure of marine stratocumulus clouds. *J. Atmos. Sci.,* **45,** 7, 1156-1175.

Bougeault, P., 1981: Modeling the trade-wind cumulus boundary layer. Part I: Testing the ensemble cloud relations against numerical data. *J. Atmos. Sci.,* **38,** 2414-2428.

Brost, R.A., D.H. Lenschow, and J.C. Wyngaard, 1981a: Marine stratocumulus layers. Part I: Mean conditions. *J. Atmos. Sci.,* **39,** 800-817.

Brost, R.A., D.H. Lenschow, and J.C. Wyngaard, 1981b: Marine stratocumulus layers. Part II: Turbulence budgets. *J. Atmos. Sci.,* **39,** 818-835.

Calahan, R.F., and J.B. Snider, 1989: Marine stratocumulus structure. *Remote Sens. Environ.,* **28,** 95-107.

Chen, C., 1984: The physics of the marine stratocumulus-capped mixed layer. Ph.D. dissertation. Research Institute of Colorado, Dept. of Atmos. Sci., Colorado State University, Fort Collins, CO 80523, 221 pp.

—, and W.R. Cotton, 1983: A one-dimensional simulation of the stratocumulus-capped mixed layer. *J. Appl. Meteor.,* **13,** 289-297.

—, and —, 1987: The physics of the marine stratocumulus-capped mixed layer. *J. Atmos. Sci.,* **44,** 2951-2977.

Chu, C.-T., 1986: Parameterization of shallow convection in the boundary layer. Master's Thesis. Oregon State University, Corvallis, OR.

Cram, J.M., 1990: Numerical simulation and analysis of the propagation of a prefrontal squall line. Ph.D. dissertation. Atmos. Sci. Paper No. 471, Dept. of Atmos. Sci., Colorado State University, Fort Collins, CO 80523, 330 pp.

Cotton, W.R., M.A. Stevens, T. Nehrkorn, and G.J. Tripoli, 1982: The Colorado State University three-dimensional cloud/mesoscale model - 1982. Part II: An ice phase parameterization. *J. de Rech. Atmos.,* **16,** 295-320.

—, G.J. Tripoli, R.M. Bauber, and E.A. Mulvihill, 1986: Numerical simulation of the effects of varying ice nucleation rates and aggregation processes on orographic snowfall. *J. Climate Appl. Meteor.,* **25,** 1658-1680.

Deardorff, J.W., 1980: Cloud-top entrainment instability. *J. Atmos. Sci.,* **37,** 131-147.

Ek, M., and L. Mahrt, 1991: A formulation for boundary-layer cloud cover. *Annales Geophysicae,* **9,** 716-724.

Flatau, P.J., G.J. Tripoli, J. Verlinde, and W.R. Cotton, 1989: The CSU-RAMS cloud microphysics module: General theory and code documentation. Technical Report 451, Colorado State University, Fort Collins, CO 80523.

Gal-Chen, T., and R.C.J. Somerville, 1975: On the use of a coordinate transformation for the solution of the Navier-Stokes equations. *J. Comput. Phys.,* **17,** 209-228.

Klemp, J.B., and R.B. Wilhelmson, 1978: Simulations of right- and left-moving storms produced through storm-splitting. *J. Atmos. Sci.,* **35,** 1097-1110.

Kuo, H., and W.H. Schubert, 1988: Stability of cloud-topped boundary layers. *Quart. J. Roy. Meteor. Soc.,* **114,** 887-917.

Kvamstø, N.G., 1991: An investigation of diagnostic relations between stratiform fractional cloud cover and other meteorological parameters in numerical weather predictions models. *J. Appl. Meteor.,* **30,** 200-216.

Le Truet, H., and Z.-X. Li, 1991: Sensitivity of an atmospheric general circulation model to prescribed SST changes: Feedback effects associated with the simulation of cloud optical properties. *Climate Dyn.,* **5,** 175-187.

Lilly, D.K., 1968: Models of cloud-topped mixed layers under a strong inversion. *Quart. J. Roy. Meteor. Soc.,* **94,** 292-309.

Louis, J.F., 1979: A parametric model of vertical eddy fluxes in the atmosphere. *Boundary-layer Meteor.,* **17,** 187-202.

MacVean, M.K., and P.J. Mason, 1990: Cloud-top entrainment instability through small-scale mixing and its parameterization in numerical models. *J. Atmos. Sci.,* **47,** 1012-1030.

Mahrer, Y., and R.A. Pielke, 1977: A numerical study of the airflow over irregular terrain. *Beitrage zur Physik der Atmosphare,* **50,** 93-113.

Manton, M.J., and W.R. Cotton, 1977: Formulation of approximate equations for modeling moist deep convection on the mesoscale. Colorado State University., Atmospheric Science Paper No. 266, 62 pp.

Mellor, G.L., 1977: The Gaussian cloud model relations. *J. Atmos. Sci.,* **34,** 356-358.

—, and T. Yamada, 1974: A hierarchy of turbulence closure models for planetary boundary layers. *J. Atmos. Sci.,* **31,** 1791-1806.

Minnis, P., P.W. Heck, D.F. Young, C.W. Fairall, and J.B. Snider, 1992: Stratocumulus cloud properties derived from simultaneous satellite and island-based instrumentation during FIRE. *J. Appl. Meteor.,* **31,** 317-339.

Mitchell, K., and D. Hahn, 1990: Objective development of diagnostic cloud forecast schemes in global and regional models. *Proc. Seventh Conf. on Atmos. Radiation,* Amer. Meteor. Soc., 23 - 27 July, San Francisco, J138-145.

Nicholls, S., 1989: The structure of radiatively-driven convection in stratocumulus. *Quart. J. Roy. Meteor. Soc.,* **115,** 487-511.

Nicholls, M.E., R.A. Pielke, J.L. Eastman, C.A. Finley, W.A. Lyons, C.J. Tremback, R.L. Walko, and W.R. Cotton, 1993: Applications of the numerical model to dispersion over urban areas. *The effect of urbanization on wind fields, air pollution spreading, and wind forces.,* NATO Advanced Study Institute.

Open University Course Team, 1989: Ocean Circulation. *Pergammon Press,* New York, in association with The Open University, Milton Keynes, England, 238 pp.

Paluch, I.R., and D.H. Lenschow, 1991: Stratiform cloud formation in the marine boundary layer. *J. Atmos. Sci.,* **48,** 2141-2158.

Pielke, R.A., W.R. Cotton, R.L. Walko, C.J. Tremback, W.A. Lyons, L.D. Grasso, M.E. Nicholls, M.D. Moran, D.A. Wesley, T.J. Lee, and J.H. Copeland, 1992:

A comprehensive meteorological modeling system - RAMS. *Meteorology and Atmospheric Physics,* **49,** 69-91.

Pudykiewicz, R., R. Benoit, and J. Mailhot, 1992: Inclusion and verification of a predictive cloud-water scheme in a regional numerical weather prediction model. *Mon. Wea. Rev.,* **120,** 612-626.

Randall, D.A., 1980: Conditional instability of the first kind upside down. *J. Atmos. Sci.,* **37**, 125-130.

Saito, K., and A. Baba, 1988: A statistical relation between relative humidity and CMS observed cloud amount. *J. Meteor. Soc. Japan,* **66,** 187-192.

Schumann, U., and C.-H. Moeng, 1991a: Plume fluxes in clear and cloudy convective boundary layers. *J. Atmos. Sci.,* **48,** 1746-1757.

Schumann, U., and C.-H. Moeng, 1991b: Plume budgets in clear and cloudy convective boundary layers. *J. Atmos. Sci.,* **48,** 1758-1770.

Shao, Q., 1994: The effects of cloud-top processes on convection in the cloud-topped boundary layer. Ph.D. dissertation. Dept. of Atmos. Sci., Colorado State University, Fort Collins, CO, 80523.

Siems, S., C. Bretherton, M. Baker, S. Sky, and R. Breidenthal, 1990: Buoyancy reversal and cloud top entrainment instability. *Quart. J. Roy. Meteor. Soc.,* **116,** 705-739.

Skupniewicz, C.E., J.W. Glendening, and R.F. Kamada, 1991: Boundary-layer transition across a stratocumulus cloud edge in a coastal zone. *Mon. Wea. Rev.,* **119,** 2337-2357.

Slingo, J.M., 1980: A cloud parameterization scheme derived from GATE data for use with a numerical model. *Quart. J. Roy. Meteor. Soc.,* **106,** 747-770.

—, 1987: The development and verification of a cloud prediction scheme for the ECMWF model. *Quart. J. Roy. Meteor. Soc.,* **113,** 899-927.

Smagorinsky, J., 1963: General circulation experiments with the primitive equations. Part I: The basic experiment. *Mon. Wea. Rev.,* **91,** 99-164.

Smith, L.D., and D.A. Randall, 1992: Parameterization of cloud microphysics processes in the CSU General Circulation Model. Atmospheric Science Paper No. 491, Colorado State University, Ft Collins, CO.

Smith, R.N., 1990: A scheme for prediction layer clouds and their water content in a general circulation model. *Quart. J. Roy. Meteor. Soc.,* **116,** 435-460.

Sommeria, G., and J.W. Deardorff, 1977: Subgrid-scale condensation in models of non-precipitating clouds. *J. Atmos. Sci.,* **34,** 344-355.

Stull, R.B., 1988: An Introduction to Boundary Layer Meteorology. *Kluwer Academic Publishers,* Boston, 666 pp.

—, and E.W. Eloranta, 1984: Boundary layer experiment - 1983. *Bull. Amer. Meteor. Soc.,* **65,** 450-456.

—, —, T.D. Crum, R.E. Vachalek, J. Shattuck, and E. Nelson, 1989: BLX83 data book - Boundary Layer Experiment - 1983 - Oklahoma. *Boundary Layer Research Team,* Dept. of Meteor., University of Wisconsin, Madison, WI, 53706.

Sundqvist, H., E. Berge, and J.E. Kristjansson, 1989: Condensation and cloud parameterization studies with a mesoscale NWP model. *Mon. Wea. Rev.,* **117,** 1641-1657.

Tremback, C.J., 1990: Numerical simulation of a mesoscale convective complex: model development and numerical results. Ph.D. dissertation. Atmos. Sci. Paper No. 465, Dept. of Atmos. Sci., Colorado State University, Fort Collins, CO 80523, 247 pp.

—, and R. Kessler, 1985: A surface temperature and moisture parameterization for use in mesoscale numerical models. Preprint volume of the Seventh Conference on Numerical Weather Prediction, June 1985, AMS, Montreal, Canada, 355-358.

—, G.J. Tripoli, R. Arritt, W.R. Cotton, and R.A. Pielke, 1986: The Regional Atmospheric Modeling System. Proceedings of the International Conference on Development and Application of Computer Techniques to Environmental Studies, Los Angeles, CA, 601-607.

Tripoli, G.J., 1986: A numerical investigation of an orogenic mesoscale convective system. Ph.D. dissertation. Atmos. Sci. Paper No. 401, Dept. of Atmos. Sci., Colorado State University, Fort Collins, CO 80523, 290 pp.

—, and W.R. Cotton, 1982: The Colorado State University three-dimensional cloud/ mesoscale model - 1982. Part I: General theoretical framework and sensitivity experiments. *J. de Rech. Atmos.,* **16,** 185-220.

Weissbluth, M., 1991: Convective parameterization in mesoscale models. Ph.D. dissertation. Atmos. Sci. Paper No. 486, Dept. of Atmos. Sci., Colorado State University, Fort Collins, CO 80523, 211 pp.

—, and W.R. Cotton, 1993: The representation of convection in mesoscale models. Part I: Scheme fabrication and calibration. *J. Atmos. Sci.,* **50,** 3852-3872.

Zeman, O., and J.L. Lumley, 1976: Modeling buoyancy driven mixed layers. *J. Atmos. Sci.,* bf 33, 1974-1988.

892004 E